University of Alberta

Geophysical Characterization of Peace River Landslide

by

Oluwafemi (Femi) Ogunsuyi

A thesis submitted to the Faculty of Graduate Studies and Research
in partial fulfillment of the requirements for the degree of

Master of Science
in
Geophysics

Department of Physics

Fall 2010
Edmonton, Alberta

Examining Committee

Dr. Douglas R. Schmitt, Department of Physics

Dr. Mauricio D. Sacchi, Department of Physics

Dr. Kevin Beach, Department of Physics

Dr. C. Derek Martin, Department of Civil and Environmental Engineering

Abstract

Landslides have occurred throughout the Holocene geologic epoch and they continue to occur in the Peace River Lowlands of Alberta and British Columbia. This study was conducted to provide an understanding of the processes and extents of one such landslide situated on a major slope at the Town of Peace River, Alberta by means of geophysical techniques with the aim of reducing the geohazard risk to lives and infrastructures. The geophysical characterization involved the acquisition, processing, and joint interpretation of seismic reflection, seismic refraction tomography, vertical seismic profile, and electrical resistivity tomography datasets, thereby providing important information about the subsurface geometry of the landslide, insights into the material properties of the unstable mass in contrast to that of the stable rock, and possible causes of the landslide. This contribution shows that putting considerable efforts into the acquisition and processing of geophysical datasets can yield valuable functional details.

Acknowledgements

I am very grateful to my supervisor, Dr. Doug Schmitt for his support, both technically and morally throughout the period of my study. Courtesy of Dr. Schmitt, my graduate program was spiced up with numerous travels conducting field experiments – at Peace River, Milk River, and Whitecourt. I really enjoyed myself during those periods, though I mostly wish then that it would be preferable to do the fieldworks without exposure to the Canadian cold that comes with them! He also offered me great opportunities to submit paper to a reputable journal and also make presentations at technical conferences. I can confidently say that he did play a great role in enhancing my technical presentation abilities. Thank you very much, Doug. I am thankful also to Dr. Mauricio Sacchi for teaching me a lot about geophysical inverse theory and for his technical assistance and concerns.

I acknowledge also the Peace River landslide project stakeholders: Alberta Geological Survey (AGS), Alberta Infrastructure and Transportation, Alberta Municipal Affairs, Town of Peace River, CN, ATCO Electric, ATCO Pipelines, University of Alberta, and NSERC for their financial support. I am also thankful to Tai-hoon Kim, Dr. Derek Martin, and Corey Froese for their support in matters related to this project. Special thanks to James Morgan of AGS for reading through the interpretation section of the thesis and the 'interpretation brainstormings' we had together about this research. Thanks, James.

I wish to also acknowledge GEDCO (Calgary) for providing the Vista® seismic processing package and Optim Software and Data Solutions (USA) for making available to me the SeisOpt® Pro™ seismic tomography software and the computer clusters at their processing center to run the seismic inversion algorithm. Thanks to Ali Oncel for connecting me with Optim Software and Data Solutions (USA). I am grateful also to WorleyParsons Ltd for making their equipments available for the acquisition of the ERT data.

Thanks to Len Tober and Lucas Duerksen for teaching me most of what I know about seismic and electrical resistivity tomography datasets acquisitions. I owe you guys a lot. I am also grateful to the field crew that assisted in the collection of the datasets used in this research project: Doug Schmitt, Marek Welz, Grey Riddle, Todd Bown, Lei Zhang, Gord Brasnett, Steve Taylor, Lucas Duerksen, Laurie Pankratow, Jamie Schmitt, James Morgan, and Waled Bin Merdhah. We were working ~ 18 hours a day for about three days and they did not bail out on me. I commend you all.

I am equally grateful to the Experimental Geophysics Group. Thanks also to my office mates, Todd and Grey, we throw geophysics ideas around and see how the concepts play out; and we did learn a lot. I am grateful to Miryam for her technical support and Spanish lessons. *Muchas gracias!* I wish to thank Sam Kaplan too for the PSDM exercises we engaged in.

To all my friends including the Adewales, Akandes, Obiosa-Maifes, Ogundipes, Masialas, Adetunjis, Akonkos, Ledgisters, and Idowu Ohioze, I wish to say thank you. I cherish your companies.

I also acknowledge my parents, brother and sisters for their encouragement and prayers.

I am especially grateful to my loving wife Funmi, for her love, encouragement, patience, and support. She gave me the required care I needed and more. Every time I was away working at school, she was always there to give me a call to find out how I was doing. Thank you very much, *Ajike*. My son, Moremy was also a source of encouragement to me. Well done, little man.

Finally, I am grateful to God Almighty for His guidance and blessings.

Table of Contents

List of Tables

List of Figures

List of Symbols and Abbreviations

b	CMP bin size
Δt	Sampling interval
f	Frequency
f_{Nq}	Nyquist frequency
f-k	Frequency-wavenumber
λ	wavelength
θ	Maximum expected dip of structures
ρ	Density
r-t	Apparent velocity-traveltime
τ–p	Intercept time-ray parameter
x-t	Offset-time
E	Least-square error
R	Reflection coefficient
P	Probability
S	Semblance
T	Temperature
V *or* v	Velocity
$\Delta\mathbf{q}$	Resistivity model parameter change vector
$\mathbf{F}$	Resistivity smoothness constrain matrix
$\mathbf{f}$	Resistivity model response vector
$\mathbf{g}$	Resistivity discrepancy vector
$\mathbf{J}$	Jacobian matrix
$\mathbf{y}$	Resistivity data vector
2D	Two dimensional
3D	Three dimensional
AGS	Alberta Geological Survey
API	American Petroleum Institute

a.s.l.	above sea level
BP	Before present
CMP	Common midpoint
DLS	Dominion Land Survey
DT	Sonic
EM	Electromagnetic
ERT	Electrical resistivity tomography
GPR	Ground penetrating radar
GPS	Global Positioning System
GR	Gamma ray
GRM	General Reciprocal Method
HSP	Horizontal seismic profiling
LiDAR	Light Detection and Ranging
NAD83	North American Datum of 1983
NMO	Normal moveout
NTS	National Topographic System
P-wave	Compressional wave
S-wave	Shear wave
S/N	Signal-to-noise
SEG	Society of Exploration Geophysicists
SP	Spontaneous potential
SWM	Surface Wave Method
UTM	Universal Transverse Mercator
VSP	Vertical seismic profiling

Chapter 1

Overview

The contribution presented here is a geophysical characterization of the processes and extents of a landslide situated on a major slope at the Town of Peace River, Alberta. The study is a component of a multidisciplinary project initiated in 2006 by various stakeholders for the purpose of reducing the landslide risk to lives and infrastructures at the Town of Peace River.

The thesis has seven constituting chapters, as summarized below.

The first chapter is a brief overview of the thesis. This chapter outlines what will be discussed in the subsequent chapters of the dissertation.

The expanded objective of this research and a review of relevant literatures on the application of geophysical methods to the study of landslides are described in the second chapter of this thesis. The chapter contains the objective of the research, which is to provide a geophysical characterization of the landslide at the Town of Peace River through the data acquisition, data analyses, and presentation and interpretation of results. Also contained in the second chapter are descriptions about different geophysical techniques, e.g., seismic, geoelectrical, and electromagnetic methods that have been applied previously by others in various scenarios to the study of landslides. The comprehensive literature review in the chapter offers a good background on how geophysics has been and could be successfully used to investigate landslides.

The third chapter provides a geological background and the results of the analyses performed on some wellbores at the study area. The chapter explains the geology of both the Cretaceous bedrock and the Quaternary sediments of the Peace River

area, thus providing an underlying geological framework upon which the interpretations of the ensuing geophysical responses are established. Formations within the Quaternary stratigraphy that are prone to sliding are examined within the chapter too, thereby ascertaining the correlations between the landslides in the Peace River valley and the lithology of the affected geologic formations. Also shown in the chapter are the results of the analyses performed on the geophysical logs of some wellbores in the study area, including the determination of the lithologies within which most of the shear planes and fractures were observed to occur.

The fourth chapter describes the field acquisition and processing of the various seismic techniques utilized in this research. The seismic methods employed include seismic reflection, seismic refraction tomography, and vertical seismic profiling. The technicalities related to the acquisition and processing of the reflection seismic data that is used to create a structural image of the subsurface are thoroughly explained in the chapter. Additionally, the inversion algorithm employed for the generation of a tomographic velocity field of the subsurface using the associated refraction data of the seismic dataset is fully discussed. The fourth chapter also contains details about the acquisition and unconventional processing of the vertical seismic profiling dataset involving the correction of some anomalous features on the field vibroseis pilot traces, and the separation of the desired waves travelling through the geologic formations in the vicinity of the wellbore from that propagating through the wellbore steel casing.

The electrical resistivity methodology, including associated data acquisition, inversion, and modeling that was employed in this study is explained in chapter five. Geoelectrical resistivity concepts relevant to the successful application of the geophysical technique are treated in the chapter as well. The chapter explains the data acquisition and the inversion technique used to generate a possible resistivity distribution of the subsurface that is intended to supply a means by which the Peace River landsliding could be delineated and equally provide information

about its associated processes on the basis of the contrasts in the subsurface resistivities. In order to assist in the subsequent interpretation of the inverted resistivity image, an electrical resistivity modeling procedure was performed to determine the resistivity measurements that will be made over a specified resistivity model. This modeling procedure and the associated results are also fully described in the fifth chapter of the thesis.

Chapter six of the thesis deals with the presentation of the various geophysical results and the associated combined interpretation. The results shown include the seismic reflection profile, seismic refraction tomography, zero-offset VSP data, and the inverted ERT images. The joint interpretation of the results is expected to reveal important information about the underlying Cretaceous bedrock, landslide extents, and landslide processes. The subsurface information provided by the interpretation of the geophysical results would be very useful to the geotechnical personnel and engineers for the purpose of carrying out a feasible and effective landslide mitigation procedure at the Peace River area. Hence, the sixth chapter of the thesis contains a detailed discussion about the geophysical interpretations.

The dissertation is wrapped up with conclusions and future work in the seventh chapter. Chapter seven sums up all the work carried out in the course of the geophysical characterization of the Peace River landslide. Also discussed in the last chapter are important future endeavours that are recommended for advancement in the work that has been performed on the Peace River landslide and in the field of geophysics in general.

The appendix contains a version of an invited paper on the subject of buried valleys that is in press with Society of Exploration Geophysicists (SEG) for publication in an upcoming book titled ‘Advances in Near-Surface Seismology and Ground-Penetrating Radar’. Currently, the accepted paper is being prepared for production. This paper is included as it describes in more detail some of the processing techniques that were also employed in the Peace River study.

Chapter 2

Introduction

"But as a mountain falls and crumbles away,
And as a rock is moved from its place;
As water wears away stones,
And as torrents wash away the soil of the earth..."

Job 14:18-19, Holy Bible

This chapter of the thesis will be started with a brief background about landslides in general, e.g., definitions, notable historic slides, etc. The expanded objective of this research work will be subsequently described. In addition, a review of relevant literatures on the application of various geophysical methods (e.g., seismic, electrical resistivity, vertical seismic profiling, etc.) to the study of landslides will also be discussed in this chapter. The literature review will contain some case histories where geophysics was utilized for the investigation of landslides, and to some extent, the basis of the interpretations made on the respective resulting geophysical images.

2.1 Background

Landslides are significant geohazards. They can occur anywhere around different areas of the world; almost no country is left immune to this problem. If left unmitigated, they pose active and unpredictable threats to lives and infrastructure. The types and causes of landslides are manifold; one only needs to view the website of the Landslides Hazards Program of the United States Geological Survey[1] to see a daily listing of the deaths and economic losses caused by landslides.

[1] http://landslides.usgs.gov/recent/ accessed May 6, 2010

The term landslide is appropriate to describe a broad scope of mass movement (McCann and Forster, 1990) including abrupt or gradual rupture of rocks, debris, or earth and their movement downslope due to the effect of gravity. A landslide could demonstrate varying movement type and extent of disruption in the course of a particular rupture (Figure 2.1). Furthermore, landslides could take place in areas where there are topographic inclines, e.g., mountain slopes, banks of rivers, and lakes or on landforms that have been stripped of their lateral constraining supports, e.g., river valleys. There are many factors that affect slope stability and hence the potential occurrences of landslides. These factors range from geologic causes (i.e., rock material strength, adverse orientation of structural discontinuities, fractures, etc.) to physical (e.g., high pore pressure from water saturation, earthquakes, volcanic eruptions, etc.) and even human activities (such as excavation, deforestation, mining, etc.) [Cruden and Varnes, 1996].

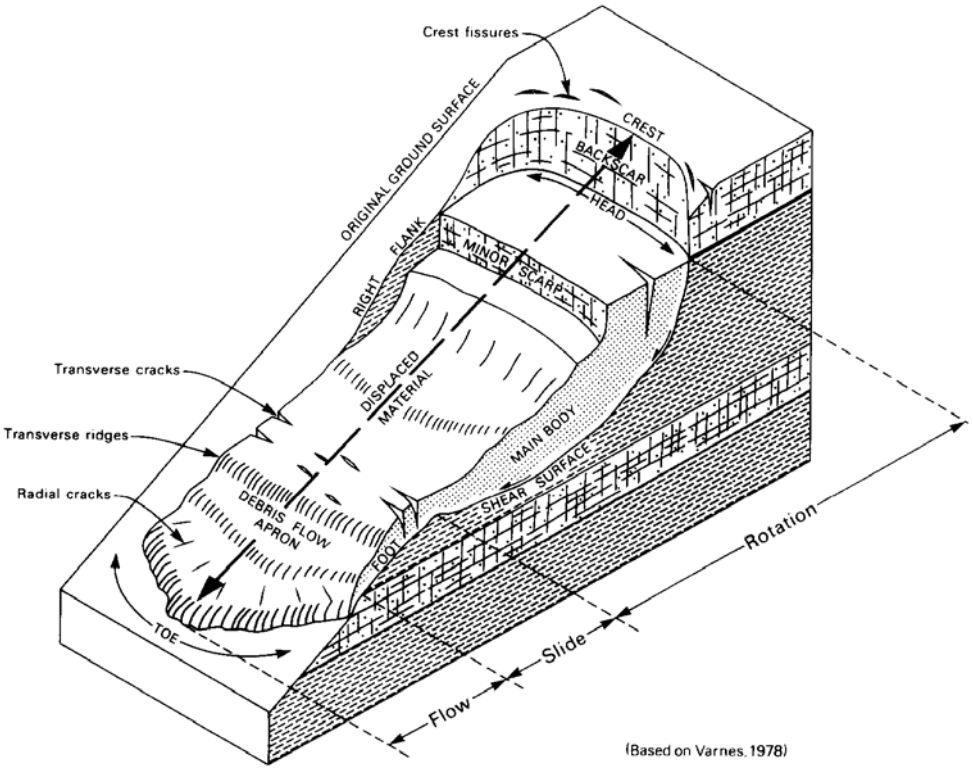

Figure 2.1: Block diagram of a complex landslide with varying movement type downslope (from McCann and Forster, 1990, based on Varnes, 1978). Reproduced with the permission of Elsevier and the Transportation Research Board.

Numerous catastrophic landslides that caused fatalities and property damage have been recorded in history. Moreover, the annual economic losses from slides can be very enormous, as established by the different landslides that have occurred in times past (Brabb and Harrod, 1989). The number of casualties and the degree of destructions depend on the size of the slide and the proximity to people and infrastructure. The possibility of an upsurge in potential risks is a consequence of rapid increase in urbanization and developments in landslide-prone areas. To avoid this loss of lives and the cost incurred from landslide incidences, it is expedient to understand the causes and characteristics of the landslide processes, determine the extent of the slope instabilities, monitor slide-prone areas, and carry out appropriate mitigation measures.

Although, as noted above, landslides are daily occurrences, it is still worth listing a few of the more notable examples.

The Val Pola landslide, which happened in Lombardy (northern Italy) on July 28, 1987 was very destructive and expensive (Crosta et al., 2003). The mass movement involved a volume between 34 and 43 million cubic meters of fractured rocks detached from a slope after a period of intense rainfall (Crosta et al., 2003). The detached rock mass, which was activated by rise in hydrostatic pressure of fractured rocks and erosion along the bed of a creek, moved approximately 800 m downslope, destroyed about 4 km of the valley below and killed 27 people from a village that was not completely evacuated (Azzoni et al., 1992). Taking into account the damage to villages, road closure, monitoring and warning procedures, and constructions and earth movement, the total cost of the slide was roughly 400 million Euros (Crosta et al., 2003). Even though some instability incidences have been recorded in the area after that major event, establishing a monitoring system that comprises geotechnical, geophysical, and topographical methods has resulted in their prior knowledge and also ensured complete safety in engineering activities (Azzoni et al., 1992). Hence, there is

likelihood that the major catastrophe could have been avoided if proper monitoring and mitigation measures were originally in place.

One of the deadliest landslide events in recent history happened in Caracas, Venezuela. A storm involving heavy rainfall spanning December 14–16, 1999 activated thousands of landslides on steep slopes. Although the landslide was in combination with flooding, the total economic losses were estimated at $1.79 billion and about 30,000 lives were lost (Wieczorek et al., 2001). According to Wieczorek et al. (2001), past records signify hydrological incidences leading to flooding and/or landslides occurring recurrently in this region, however not as disastrous as the 1999 event. These previous occurrences could be interpreted as an indication of imminent geohazards. Again, it is probable the ensuing damages to properties, disruptions of social services and fatalities could have been minimized if the initial landslides were studied, monitored and proper hazard reduction processes deployed.

Alberta is not immune from infamous and destructive landslides. The historic Frank slide occurred in the coal mining town of Frank, southern Alberta on April 29, 1903 at 4:10 am and it lasted for about 100 seconds. An enormous rock mass of limestone and shale, nearly half a mile square in area and about 400 to 500 ft thick, abruptly broke free from the face of Turtle Mountain with huge force into the valley beneath, demolishing everything in its path (McConnell and Brock, 2003). The geohazard location was characterized by steep slopes of the Turtle Mountain ridges and flat-bottomed river valley at its base. According to McConnell and Brock (2003), houses, rural buildings, and also railway tracks were destroyed by the slide; and about 70 people were estimated to be killed and some others injured. There were many factors deemed responsible for the slide: structure of Turtle Mountain, which was comprehensively dissected by fractures and jointing planes; weakening due to coal mining at the toe of mountain; above-average rainfall in months before the slide; water and ice accumulation in fractures at the top of the mountain; seismic activity before the major event; and

thermal variations (McConnell and Brock, 2003; Moreno and Froese, 2006). The risk of further slides remains real and, because of this, various geophysical monitoring techniques have been employed and studies of the extensive fracturing of the mountain undertaken (e.g., Theune et al., 2005; Theune et al., 2006) over the last half century.

As stated earlier, there are many attributes that make slopes to be susceptible to failures (e.g., geologic, physical factors, etc.). However, a landslide trigger is an external stimulus like earthquake, snowmelt, or intense rainfall that sets off the actual mass movement by reducing the slope material strength or increasing the shear stresses on the materials. Further, landslides can be classified and described by the type of material and the type of movement involved in the slides according to the categorization developed by Cruden and Varnes (1996). The classification of the material type is based on the constituting particle size (i.e., rock, debris, or earth) and the movement is based on the kinematics, e.g., fall, topple, slide, spread, or flow (Cruden and Varnes, 1996). Using this nomenclature, the name of any landslide describes the movement system fully. Some historic landslide events, which make good reading, are presented in Voight (1978); and Eisbacher and Clague (1984). The landslides described are of different types, ranging from surficial debris flow to rockfall, and triggered by different events, from earthquakes to human activities.

2.2 Motivation

Landslides have occurred throughout the Holocene geologic epoch and they continue to occur in the Peace River Lowlands[2] of Alberta and British Columbia (Davies et al., 2005). These slides are not generally directly hazardous to human safety; they nevertheless affect infrastructure in the area.

[2] Physiographic zone within the Interior Plains of Canada (Klassen, 1989).

In order to better understand these geohazards, a multidisciplinary project was initiated in 2006 by various stakeholders (Froese, 2007) to study the landslide processes and extents around the Town of Peace River, Alberta. The ultimate aim is to reduce the landslide risk to lives and infrastructures. This thesis describes the geophysical component of the study, vis-à-vis data acquisition, analyses, presentation of results, and the associated interpretation. These geophysical investigations will contribute to a better overall geological characterization of the area.

In order to carry out a feasible and effective landslide mitigation procedure, slope stability analyses involving knowledge of the subsurface structure and physical properties of the constituting materials are required. The information gained can provide substantial understanding of the mechanisms and the likely causes of slope failure. A key feature of landslides that is used to access stability, amidst other elements, is the shear (or rupture) surface (see Figure 2.1) that represents the boundary between the displaced materials and the unaffected rock. Surface examinations of landslide areas provide limited information in determining the causes of the slides. For a deep-seated landslide, it may be impossible to define its geometry, including its rupture surface, by surface inspection alone. Boreholes and geophysical methods, on the other hand, are useful in providing these much needed information for proper slope stability analysis. Apart from the relative expensive costs of drilling boreholes in comparison to using geophysical methods to study landslides, the data acquired from a borehole is also single-point based. In order to obtain adequate knowledge of the area, interpolations have to be made among numerous wellbores to fill in the spatial gaps. This makes geophysical techniques preferable, considering the lower cost, extensive lateral and depth coverage and reduced damage to formations. Geophysical techniques may provide valuable results on defining the geometry of landslides, describing their internal structures, revealing effect of groundwater on them, the physical properties of the landslide materials, and the landslide mass movement (Göktürkler et al., 2008 and references contained therein).

Geophysical techniques, however, require a contrast in the physical properties (e.g., seismic impedance, electrical resistivity, etc.) of the constituting rock materials in order to be effective. If the rupture surface of the landslide lies between two different beds of considerable difference in physical properties (for example, due to different water content), then geophysical method could be used to detect the surface. *However, in the scenario in which a landslide is occurring within a lithological unit, will there be significant contrast in the physical properties of the materials constituting the unit for the rupture surface to be detected with a combination of geophysical tools? Likewise, would enough information be obtained to provide insight to the causes of the mass movement? In the case of seismic methods, can the analyses of the character of the seismic reflections within different rock materials supply valuable information in distinguishing the displaced mass from the competent rocks?* These are some of the questions this thesis will attempt to address.

Furthermore, geophysical measurements give an image of the bulk physical properties of the rocks and *not* some specific petrophysical parameters (e.g. porosity, permeability, fluid saturation, etc.) which are mostly needed. Consequently, one needs to establish a relationship between the geophysical and material properties; and this is generally not straightforward. For instance, the electrical conductivity of a rock is based on the electrical conductivity of the separate constituents (i.e., solids and fluids), their volume fractions, geometrical distribution and interactions amidst other factors (see Knight and Endres, 2005). It is therefore obvious that a variety of factors influence an observed physical property and it may be difficult to determine precisely the values of the various desired material properties from this single measurement. Thus, there is need to employ and jointly interpret more than one type of geophysical observable in order to reasonably estimate the material properties of a given rock body.

Consequently, high resolution reflection seismic profiling, seismic refraction tomography, vertical seismic profiling (VSP), and electrical resistivity

tomography (ERT) techniques in combination with geophysical wellbore logs were utilized in exploring the subsurface dimensions of the landsliding at the Town of Peace River, and in providing insights into the material properties of the unstable mass and competent rock in addition to the possible causes of the mass movements.

The Peace River landslide has been previously determined to be a relict, retrogressive, translational earth slide (J. Morgan, personal communication, 2010). The term retrogressive signifies that the rupture surface of the landslide is extending in the opposite direction to the movement of the displaced material (Cruden and Varnes, 1996). The Peace River landslide is deemed to be similar to the earth slides at the Thompson River Valley (investigated by Eshraghian et al., 2007) that resulted in multiple sliding block units (Figure 2.2; C. D. Martin, personal communication, 2010). The translational sliding block units are not expected to result in significant lateral variation in the physical property of the materials except at places where there are changes in stratigraphy (C. D. Martin, personal communication, 2010).

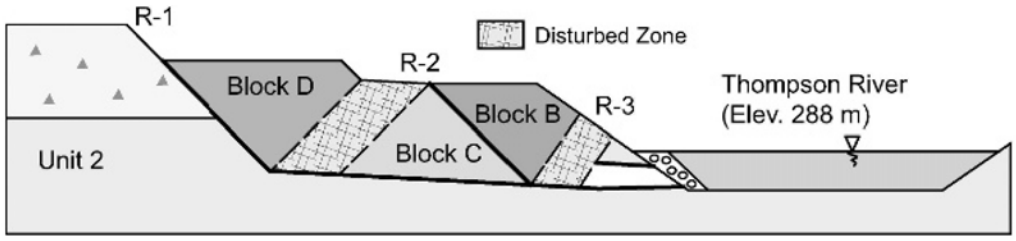

Figure 2.2: Block diagram of a retrogressive earth slide in the Thompson River Valley, British Columbia (from Eshraghian et al., 2007).

2.3 Literature Review

Given that a number of landslides areas are critical transportation passages (i.e., highways and railways), sites of service facilities (e.g., communication and power cables, hydrocarbon pipelines, etc.), and even residential quarters, the application

of any potentially effectual method to understand landslide processes cannot be disregarded. In the light of this, geophysical techniques have been utilized, successfully, in various parts of the world to study landslides in order to ensure public safety and to safeguard infrastructure.

Reflection seismic profiling is a common geophysical tool utilized in a wide range of scenarios to image the subsurface (e.g., Hunter et al., 1984; Miller and Steeples, 1994; Juhlin et al., 2002). It is surprising that until recently it has not been used extensively to study landslides, indicated by the apparent relative paucity of scientific papers on the subject. Ferrucci et al. (1999) suggested that the reason is because landslides are structurally complex and the landslide mass is not a good medium for seismic wave propagation, this being attributable to dispersion and noise. Another reason could be the uneven surface topography of landslides areas which could be characterized by steep slopes and hummocky features, making seismic reflection field data acquisition quite difficult. Nevertheless, high resolution seismic reflection method has been employed in accurately detecting the depth of a landslide in western Swiss Alps (Bruno and Marillier, 2000). This same technique has even been used to study a prehistoric slide in Utah, USA (Tingey et al., 2007). In addition, Lykousis et al. (2007) has some examples on the application of seismic reflection method to the study of submarine landslides. It is expected that if there is a significant contrast between the acoustic impedances of the landslide body and the underlying more stable bedrock, strong reflectors will likely be observed at the rupture surface. It is worth mentioning, however, that shallow landslides may be difficult to image with seismic reflection profiling by reason of the wave signal being affected by source generated noise. But with recent developments in shallow seismic reflection method (Steeples, 1998), the use of the technique in imaging shallow landslides could become increasingly successful.

Recently, Stucchi and Mazzotti (2009), presented the results of on- and offshore reflection profiles to delineate the geometry of the deepest possible rupture

surface of a landslide in Italy. Their interpretation in determining the detachment surface is based on the boundary between areas where differences in the nature of the seismic reflections are observed, i.e., chaotic reflections within the landslide body and continuous reflections in the undisturbed rock. Moreover, Bichler et al. (2004) employed P- and S-wave seismic reflection methods to obtain unit boundaries in the Quesnel Forks landslide, Canada; however the methods were not successful in delineating the rupture surface.

A more commonly used geophysical method to describe landslides is seismic refraction. Seismic refraction technique uses first break time picks to generate compressional and/or shear wave velocities for the subsurface. Compressional and shear wave speeds are generally lower within landslide bodies than in undisturbed rocks (Jongmans and Garambois, 2007), possibly due to the weathered and fractured nature of the landslide mass. The General Reciprocal Method (GRM), which assumes a layered model and is used to interpret seismic refraction dataset by calculating refractor velocities and depths via overlapping forward and reverse shots traveltimes (Palmer, 1981) was employed by Narwold and Owen (2002) to model landslides. Furthermore, seismic refraction has proved appropriate in delineating landslides depths (e.g., Bogoslovsky and Ogilvy, 1977; McCann and Forster, 1990; Havenith et al., 2000).

Seismic tomography involves the inversion of first arrival traveltimes from many sources and geophones to create a seismic wave velocity distribution of the subsurface. Seismic refraction tomography is able to produce a good representation of landslides that have complex velocity structures (Narwold and Owen, 2002). This method has been used broadly to model landslides (e.g., Heincke et al., 2006; Meric et al., 2005; Jongmans et al., 2009). It is observed that seismic tomography images lateral velocity changes competently. Israil and Pachauri (2003) and Godio et al. (2006) utilized seismic tomography in conjunction with Surface Wave Method (SWM) for the characterization of landslides areas. SWM uses Rayleigh-wave data recorded on geophones to

determine phase-velocity dispersion curve, and then shear wave velocity with respect to depth is estimated from the dispersion relation by performing a geophysical inversion procedure (e.g., Beaty and Schmitt, 2003; Pelton, 2005).

Another geophysical tool commonly used to study landslides is resistivity (or geoelectrical) methods. These measurements seek to distinguish different rock materials on the basis of their electrical resistivity properties. The relationship between a rock mass and its resistivity is quite complex because the resistivity depends largely on its numerous physical characteristics. Some of the effects of rock physical properties (e.g., porosity, pore fluid resistivity, water saturation, etc.) on the true resistivity of a rock as related to landslides investigations are outlined in Park and Kim (2005). The resistivity values of the landslide mass are expected to be different from that of the undisturbed body because of the movement of materials and deformations by the slide (Jongmans et al., 2009). Lapenna et al. (2005) encountered lower resistivity values in a landslide body, which was characterized by high content of clayey material and increase in water content, in comparison to the resistivity values of the unaffected rock. On the other hand, Meric et al. (2005) observed higher electrical resistivity values in a different landslide body, in contrast to the unaffected mass, due to a great level of fracturing related to air-filled spaces in the deformed mass. Thus, if there is substantial resistivity contrast between the different masses, the slip surface should be readily distinguishable. Electrical resistivity tomography (ERT) offers an electrical resistivity distribution (2D or 3D) of the subsurface.

Resistivity methods have been widely used to delineate landslides (e.g., Batayneh and Al-Diabat, 2002; Agnesi et al., 2005; Drahor et al., 2006; Lee et al., 2008) and in conjunction with seismic data (e.g., Socco et al., 2010; Heincke et al., 2010). Sometimes, self-potential (SP) measurements are blended with resistivity surveys because of the low costs involved (Hack, 2000). SP method is based on the measurements of natural electrical potentials induced by water flow through rock (Bogoslovsky and Ogilvy, 1977). Combinations of electrical resistivity

methods and SP measurements have also been employed to study landslides (Lapenna et al., 2003; Naudet et al., 2008).

Ground penetrating radar (GPR) has also been used to study slope stability, i.e., Toshioka et al., 1995 and Theune et al., 2006 – to map rock fractures and cracks; Roch et al., 2006 – capability for monitoring rockfall; and Bichler et al., 2004 – to determine the depth of the rupture surface. GPR uses reflected high frequency electromagnetic waves to image the subsurface based on the contrasts in the dielectric permittivity properties of the rock materials. However, applying GPR technique to study landslides has some shortcomings, e.g., signals are greatly attenuated in conductive formations and fractures create diffractions, thus reducing the depth of signal penetration (Jongmans and Garambois, 2007). Hence, they are generally used in combination with other geophysical methods (e.g., Sass et al., 2008).

Electromagnetic (EM) methods use low frequency electromagnetic waves to determine the conductivity of the subsurface by comparing a transmitted (or primary) field to a secondary field induced in the subsurface materials (Hack, 2000). EM methods are also used to characterize landslides (e.g., Cummings, 2000) and in combination with other geophysical methods (e.g., Caris and Van Asch, 1991; Schmutz et al., 2000; Godio and Bottino, 2001; Jongmans and Garambois, 2007).

Vertical seismic profiling (VSP) method is seldom used in mapping out landslides. Liu et al. (2001) used VSP to locate the distribution of formations and the sliding surfaces in the locality of some boreholes. Godio et al. (2006) conducted a seismic profiling survey in a horizontal wellbore, describing the procedure as horizontal seismic profiling (HSP). They utilized HSP method in conjunction with sonic log to characterize rock mass, based on geomechanical properties, i.e., presence of fractures. Other geophysical methods that have been used to study landslides include microseismic monitoring (Novosad et al, 1977),

seismic noise measurements, i.e., H/V method (Meric et al., 2007), magnetic field observations (McCann and Forster, 1990 and references contained) and gravimetric measurements (Del Gaudio et al., 2000).

Typically, most of these geophysical methods are not utilized in isolation, on the contrary, they are used in conjunction with other techniques (as shown in Bogoslovsky and Ogilvy, 1977; Bichler et al., 2004; and Meric et al., 2005) to better understand the landslide geometry and the physical properties of the materials. Bearing in mind that different geophysical methods are sensitive to varied physical properties, it is important to combine a variety of techniques during geohazard studies in order to obtain better insights into the landslides and their processes. Various geophysical methods and their suitability for slope stability investigations are discussed in Hack, 2000.

2.4 Summary

The objective of this study, which is to provide a geophysical characterization of a landslide at the Town of Peace River with the aim of reducing risks to lives and infrastructures, has been explained explicitly in this chapter. Employing geophysical techniques for the study of landslides is preferred over wellbores because of the relatively lower costs, extensive lateral and depth coverage, and less damage to formations. However, contrasts in the physical properties of the landslide disturbed materials and unaffected rocks are necessary for the geophysical methods to be successful. Also described in this chapter are the various geophysical methods that have been applied previously by others to the study of landslides. The reviewed geophysical techniques include seismic, geoelectrical, and electromagnetic methods. Moreover, since different geophysical methods are responsive to varied physical properties, utilizing a combination of the techniques might be essential to gain a thorough understanding of the landslide processes and extents.

Chapter 3

Geological Framework

This chapter of the thesis will deal with the pertinent underlying geological framework of the study area. Beginning with a brief background about the study area, the geology of the bedrock and the various features of the different constituting formations will be explained. In addition, the Quaternary geology and corresponding stratigraphy will be examined. Landslides in the Peace River valley and their relationships with the lithology of the geologic formations will be similarly discussed. The chapter will be wrapped up with a discussion about the results of the analyses performed on some wellbore geophysical logs at the study area.

3.1 Study Area

The research area, marked by the large star in Figure 3.1a is located, according to the National Topographic System (NTS) of Canada, in the Peace River map area (NTS 84C) of Alberta. The geophysical study area (~ Lat 56^0 14′ N and ~ Long 117^0 21′ W) is to the west of the Peace River and it lies within Township 83 and Ranges 21 to 22, west of the 5th Meridian according to the Dominion Land Survey (DLS) system (Figure 3.1b). The area falls inside the Interior Plains of Canada within the Peace River Lowland physiographic section of the Northern Alberta Lowlands region (Pettapiece, 1986). The Peace River Lowlands is flanked by the Buffalo Head Hills on the east and the Clear Hills on the west.

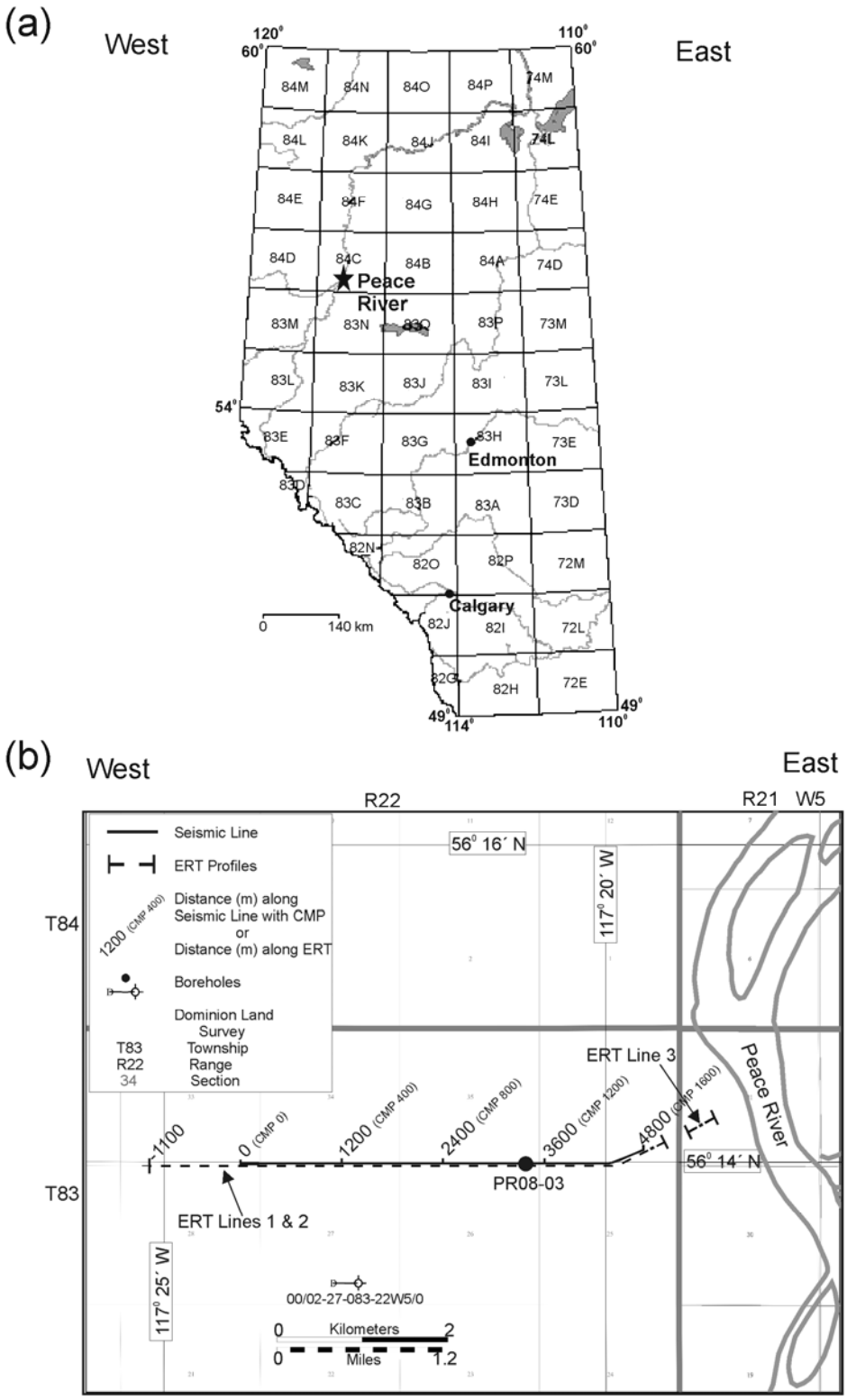

Figure 3.1. Figure caption on next page.

Figure 3.1. (a) The research area (Peace River; NTS 84C) is marked with a large star. Figure was modified from Alberta Geological Survey (AGS) website with authorization under the Non-Commercial Reproduction policy of AGS. (b) The locations of two wellbores, seismic line and the ERT profile lines are shown according to Dominion Land Survey (DLS) system. The thick black line illustrates the location of the seismic line while the thick dashed lines denote the locations of the electrical resistivity tomography (ERT) profiles.

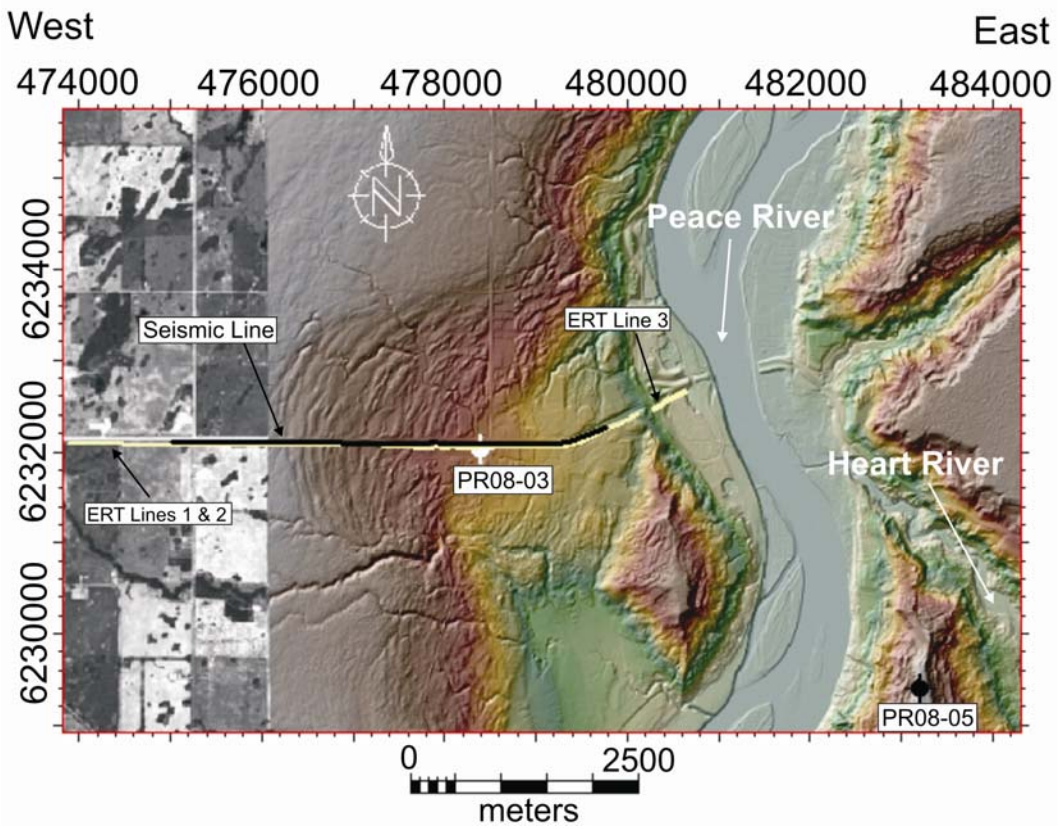

Figure 3.2. High resolution (1 m) colored Light Detection and Ranging (LiDAR) bare earth image of the Peace River region (not completely shown) overlaid on a lower resolution image (in grayscale); courtesy of the AGS. The locations of the wellbores PR08-03 and PR08-05 are shown; the seismic and the electrical resistivity tomography (ERT) profile lines are displayed in black and yellow lines respectively. The geographic locations are given in Universal Transverse Mercator (UTM) coordinates (Zone 11N) with respect to NAD83 datum.

The Peace River Lowlands of Alberta and British Columbia is historically active as related to mass movements, with landslides occurring throughout the Holocene epoch and continuing today in the region (Davies et al., 2005). In order to understand the landslides and failure potential in the Peace River valley, a high resolution (1 m) bare earth Light Detection and Ranging (LiDAR) image of the study region was conducted over 100 km^2 area centered on the Town of Peace River by Alberta Geological Survey (Morgan et al., 2008; Figure 3.2). A LiDAR system transmits and receives high frequency electromagnetic waves to obtain range and other information about far objects by analyzing the delay time between the transmitted and reflected pulses. LiDAR are advantageous over microwave radar technique for range measurements because of the high energy pulse that can be achieved in short intervals (e.g., Wehr and Lohr, 1999). The LiDAR data shows the ground surface stripped of buildings and vegetation, thus potentially affording insight into the landslide processes through the character of the landforms. Accordingly, the hummocky geomorphology observed on the west side of the Peace River (Figure 3.2) can be interpreted to be as a result of the landslide processes.

Most of the surface morphology of the area is as a result of processes associated with the last glacial event (i.e., late Wisconsin) and Holocene erosion (Davies et al., 2005). After deglaciation, the Peace River incised through the Quaternary sediments and into the underlying Cretaceous bedrock and this has developed into the dominant geomorphic feature of the region, i.e., the Peace River valley. Recent work carried out by Morgan et al. (2008) revealed that the Peace River has incised through about 180 m of Quaternary sediments and 30 m into the Cretaceous bedrock in the study area. The Cretaceous bedrock in the area is mostly covered by Quaternary sediments and the bedrock is rarely exposed to the surface except primarily at the river valley. In order to be able to fully understand and interpret the geophysical responses observed in upcoming chapters, it is crucial to know the geological context. As such, the geology of the bedrock and the Quaternary deposits are described below.

3.2 Geology of the Bedrock

The bedrock in the study area, falling within the Western Canada Sedimentary Basin is of geologic Cretaceous period (~ 100 Ma) of the Mesozoic era. The Cretaceous Fort St. John Group is the lowermost stratigraphic package relevant to the landslide processes in the Peace River area (Davies et al., 2005 and references therein). The Fort St. John Group is composed of the Peace River Formation and the stratigraphically lower Spirit River Formation. Discussion of the bedrock geology for this study will be limited to the Peace River Formation, considered to be the lowest stratigraphy unit related to the landslide mechanisms, and the stratigraphic units above it. The elevation of the bedrock, created from well logs and outcroppings by Morgan et al., 2008 for the high resolution LiDAR area, ranges from about 300 m to 400 m above sea level (a.s.l.) (Figure 3.3). It is also observed that the topography of the bedrock slopes towards the Peace River, as the ground surface elevation (Figure 3.3).

In addition to the description of the bedrock that will be treated in this subsection, the geophysical logs of a conventional petroleum wellbore that penetrated the Cretaceous formations will also be examined. The reason for analyzing the bedrock signature on geophysical logs is to determine the bedrock response that will be observed on the geophysical tools applied in this study. The geophysical logs examined are associated with a nearby deviated well (00/02-27-083-22W5/0; Figure 3.1b) operated by Penn West Petroleum Ltd. However, because digital logs were not available for wellbore 00/02-27-083-22W5/0, limited analysis will be performed on the accessible raster image.

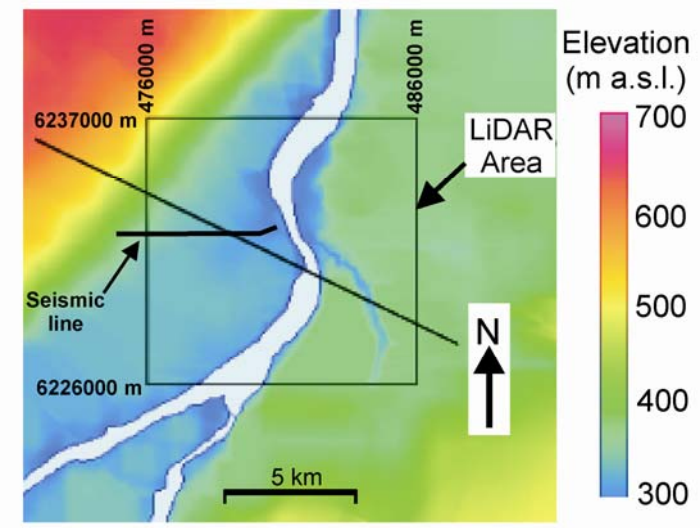

Figure 3.3. Bedrock Topography of the Peace River area (from Morgan et al., 2008). The easting and the northing of the LiDAR area are shown in UTM zone 11N coordinates. Figure was reprinted with authorization under the Non-Commercial Reproduction policy of AGS.

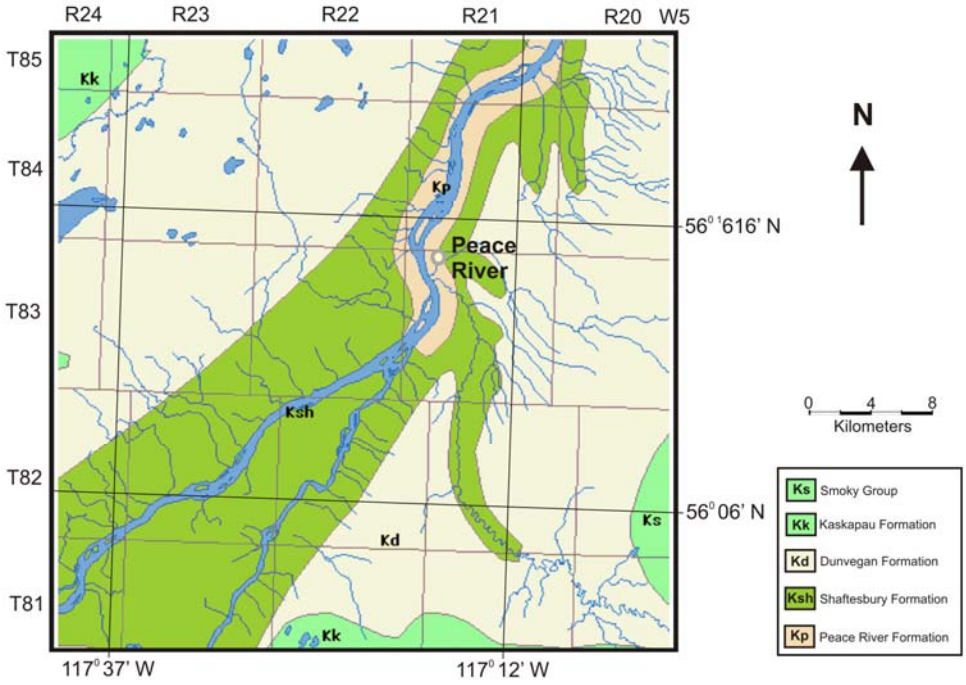

Figure 3.4. Bedrock geology of the Peace River area (modified from Hamilton et al., 1999). Figure was reprinted with authorization under the Non-Commercial Reproduction policy of AGS.

3.2.1 Peace River Formation

The Lower Cretaceous Peace River Formation outcrops along the bottom of the Peace River valley except in the reach south of the town of Peace River (Hamilton et al., 1999). The formation is the lowermost exposed unit in the area (Figure 3.4) and it is composed of the Paddy and Cadotte members (sandstones) underlain by the Harmon member (shale) (e.g., Leslie and Fenton, 2001). The Paddy member is basically made up of estuarine valley deposits, fluvial channel, and coastal plain facies (Davies et al., 2005). The Cadotte member is a clean, marine, coarse to fine grained, massively bedded sandstone; while the oldest unit, Harmon member, comprises soft, fissile, non calcareous dark grey shale (Leslie and Fenton, 2001). There is an erosional unconformity separating the Cadotte and Harmon members (Davies et al., 2005).

3.2.2 Shaftesbury Formation

Above the Peace River Formation is the Shaftesbury Formation (Figure 3.4) which outcrops mainly along the Peace River in the reach south of the town of Peace River (Hamilton et al., 1999). This formation extends over the boundary between Upper and Lower Cretaceous and it contains dark grey fish-scale bearing marine shale with bentonite partings and numerous replacement bodies and thin beds of concretionary ironstone (Hamilton et al., 1999). The upper part of the formation is silty in nature and the lower part contains thin silty and sandy intervals overlying the Peace River Formation. Lithology influences slope stability greatly and previous work as performed by Cruden et al. (1990) in analyzing landslide incidences observed on air photographs along 557 km of the Peace River showed that the shales of the Shaftesbury Formation are very prone to sliding. Davies et al. (2005) suggest that the physical properties of the shale in this formation may be the cause of the increased landslide incidences.

3.2.3 Dunvegan Formation

The upper contact of the Shaftesbury Formation is gradational into the overlying Dunvegan Formation; and though the Dunvegan unit is not observed in the geophysical study area, it is regionally extensive in the Peace River region (Figure 3.4). The formation is of Late Cretaceous age and its lower contact is conformable with the Shaftesbury Formation (Leslie and Fenton, 2001). The Dunvegan Formation is primarily grey, fine-grained, feldspathic sandstone with hard calcareous beds and laminated siltstone and grey silty shale (Hamilton et al., 1999). Notably, the formation is competent in contrast to the slide-susceptible Shaftesbury Formation (Cruden et al., 1990).

3.2.4 Smoky Group

The Smoky Group (of Late Cretaceous age) lies to the west of Peace River and it is composed of the Kaskapau and Puskwaskau formations. The Puskwaskau formation is younger than the Kaskapau formation which in turn lies stratigraphically above the Dunvegan Formation. The Kaskapau formation consists of dark grey silty marine shale with thin concretionary ironstone beds while the Puskwaskau formation is dark grey fossiliferous marine shale (Hamilton et al., 1999). Though slope failures are common in the thinly bedded shales of the Kaskapau formation (Cruden et al., 1990), the formation occurs to the west outside of the research area, away from the Peace River valley and its tributaries (Figure 3.4); and thus will not be given further consideration in this study.

3.2.5 Bedrock Signature on Geophysical Logs

The available raster image of some of the geophysical logs of wellbore 00/02-27-083-22W5/0 is presented (Figure 3.5). The borehole was drilled in 2001 from 542 m a.s.l. datum to a total depth of 800 m, thus penetrating both the Shaftesbury and Peace River Formations. The tops of the Paddy and Cadotte units were

encountered at depths 224 m (i.e., 318 m a.s.l.) and 232 m (i.e., 310 m a.s.l.) respectively in the borehole.

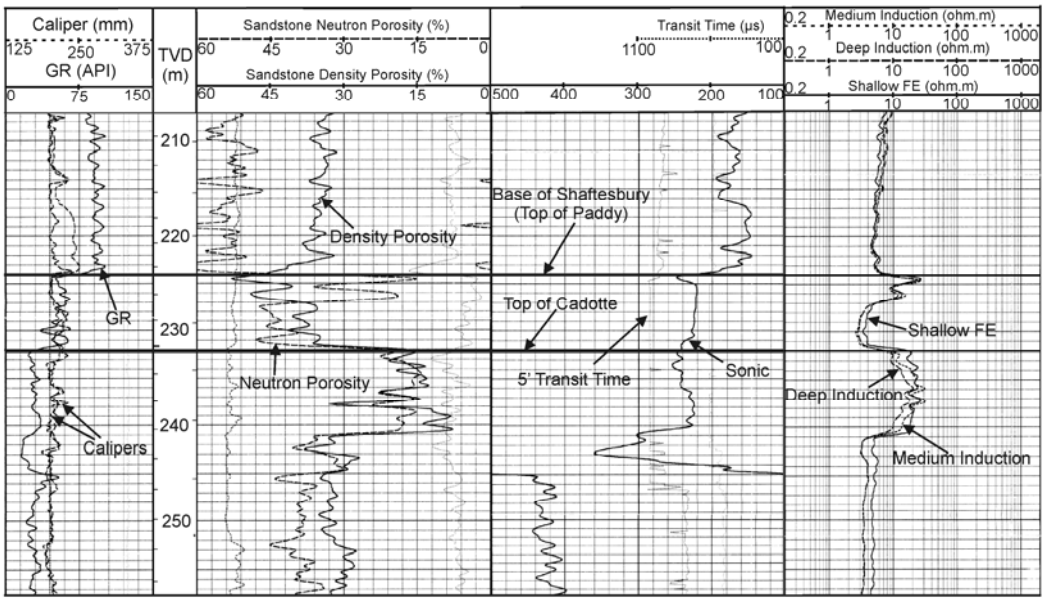

Figure 3.5. Raster image of geophysical logs for wellbore 00/02-27-083-22W5/0. The first track contains GR and caliper logs, while total vertical depth is displayed in the second track. Sandstone neutron and density porosities are displayed in the third track while the fourth track contains the compensated sonic and the transit time. The fifth track contains shallow FE, medium induction, and deep induction resistivity logs. Note that the sonic log wraps around in its track with DT values > 500 µs/m for depths < ~ 245 m and DT values < 500 µs/m for depths > ~ 245 m. The top of Paddy and Cadotte formations are shown in black heavy lines.

The boundary between the Shaftesbury and the Peace River Formation is obvious on the GR log, typified by relatively higher values within the shale (GR > 80 API) in contrast to lower values in the Paddy member unit (i.e., GR < 60 API) (Figure 3.5). A further decrease in the GR values distinguishes the Paddy member from

the Cadotte formation (i.e., GR < 30 API). As observed on the density porosity log, the porosity values increased across the Shaftesbury-Paddy interface (Figure 3.5), indicating a decrease in the density. The density increased gradually with depth within the Paddy member and then sharply at the top of the Cadotte unit. A slight increase in DT values (from ~ 570 μs/m to ~ 620 μs/m) was noticed as one transits from the Shaftesbury Formation into the Paddy member, signifying a small decrease in velocities across the boundary (~ 150 m/s). These lower velocities were also encountered in the topmost section of the Cadotte unit, before a subsequent sharp increase at ~ 245 m depth.

Due to the small decrease in velocities from Shaftesbury to the Paddy member, it is uncertain if this boundary can be resolved clearly on a low-resolution seismic tomography image of the subsurface. However, taking into account the decrease in both velocities and densities, it is expected that seismic reflection method would be able to reveal the boundary as a result of the drop in the acoustic impedance (product of velocity and density) across the Shaftesbury-Paddy interface. Nevertheless, imaging the boundary clearly with seismic reflection technique is subject to the resolution of the seismic data.

3.3 Quaternary Geology

Historically, it is believed that only one Laurentide glacial event, i.e., the late Wisconsin Lostwood Glaciation (Fenton, 1984) affected the west-central Alberta region (Liverman et al., 1989). However recent work by Leslie and Fenton (2001) suggests that a separate previous major glacial advance could also have possibly taken place in the region. Leslie and Fenton (2001) based this proposition on the observation of a fluvial sediment unit with Canadian Shield provenance stratigraphically below the Late Glacial ice advance complex of the Lostwood Glaciation. Davies et al. (2005) indicate that this major ice advance is of Burke Lake Glaciation of early Wisconsin age (Fenton, 1984). However, due to lack of

more information, it has been suggested that there could have been more than one early glacial advance in the area (Leslie and Fenton, 2001).

The Lostwood Glaciation of late Wisconsin age advancing into the region reached a maximum between 20,000 and 18,000 years Before Present (BP) and the glacial retreat occurred around 10,000 years BP (Fenton, 1984). The last glacial advance in the Peace River area flowed in southwesterly direction across the river valley at glacial maximum (Davies et al., 2005) and completely covered the region with the Clear and Whitemud Hills (i.e., east-west trending uplands) slowing down its advance but not blocking it (e.g., Leslie and Fenton, 2001). During the initial waning of the glaciation, ice in the uplands was probably separated from that in the lowlands surrounding the town of Peace River (Leslie and Fenton, 2001). The Laurentide ice sheet retreated northward and down-drainage during early deglaciation and this constituted the blocking of the drainage and ponding of the glacial meltwaters (Davies et al., 2005). One of the larger glacial lakes that formed was Glacial Lake Peace and it extended westerly into British Columbia and as far north as High Level in Alberta (Mathews, 1980). Glacial Lake Peace silt, clay and minor sand of varying thicknesses cover the study area below 610 m a.s.l. (e.g., Paulen, 2004; Morgan et al., 2008). The Lostwood Glacial deposits contain proglacial lacustrine sediments that came about as the advancing ice dammed drainage (Catto et al., 1996); advance outwash glaciofluvial sediments (Leslie and Fenton, 2001); and till and glacial Lake Peace sediments (Mathews, 1980).

Glacial melting continued to a point where the glacial lake drained through an outlet in the southeast and flooded north along the Peace River to inundate the Manning Lowland (Leslie and Fenton, 2001). Deposition of glacial sediments was ended abruptly when ice melted far enough northward to drain the glacial lake from the Manning area (Leslie and Fenton, 2001). After the drainage, the Peace River immediately began incising through the Quaternary sediments in the early Holocene (Davies et al., 2005). Slope failures, that occurred throughout the

Holocene period and still continue, and mass movement has resulted in thick accumulations of colluvium along the Peace River and its tributaries (Morgan et al., 2008). Holocene deposits include organic sediments, fluvial terraces from river incisions, loess deposits, and colluvial deposits from landslide processes (Davies et al., 2005).

3.3.1 Quaternary Stratigraphy

Morgan et al. (2008) described the results of a field based mapping effort of the overlying Quaternary sediment stratigraphy of the Peace River area. The authors' composite Quaternary geology as mapped at the confluence of the Heart and Peace Rivers (Figure 3.6) is described below.

Lying above the Shaftesbury Formation shale Cretaceous bedrock in our study area is the lowermost Quaternary stratigraphy unit, which is fluvial sediments that are dominated by heavily oxidized, sandy planar bedded pebble gravels. Lithologies of this unit are primarily Cordilleran in origin and there is complete lack of Canadian Shield clast lithologies in the sediment (Morgan et al., 2008). Laurentide deposits are recognizable by their significant content of erratics from Canadian Shield (Mathews, 1980); hence the lack of these erratics suggests that the unit is possibly of preglacial origin.

A package containing clasts from Canadian Shield overlies the oxidized gravels. The package contains a lower pebbly sand unit, a middle coarse gravel packet, and a thick stratified sandy unit over the gravel formation. Leslie and Fenton (2001) described the sediment as an Early Glacial advance deposit while Morgan et al. (2008) proposed a Middle Wisconsin age based on a similar sedimentary package encountered in the basal Peace River valley with AMS radiocarbon date of 25,120 +/- 140 ^{14}C BP.

Above this sedimentary package containing clasts of Canadian Shield provenance lies thick (almost 100 m) sorted fine sand, silt, and clay glaciolacustrine sediments of Late Wisconsin advance-phase period. The deposit, which is overconsolidated, is assumed to be from a lake formed in the Peace River valley on account of the dammed drainage outlets by the advancing Late Wisconsin Laurentide Ice Sheet. Slope failures occur in these thick deeply-buried overconsolidated glaciolacustrine sediments that are present throughout the western Peace River Lowlands of Alberta (Davies et al., 2005).

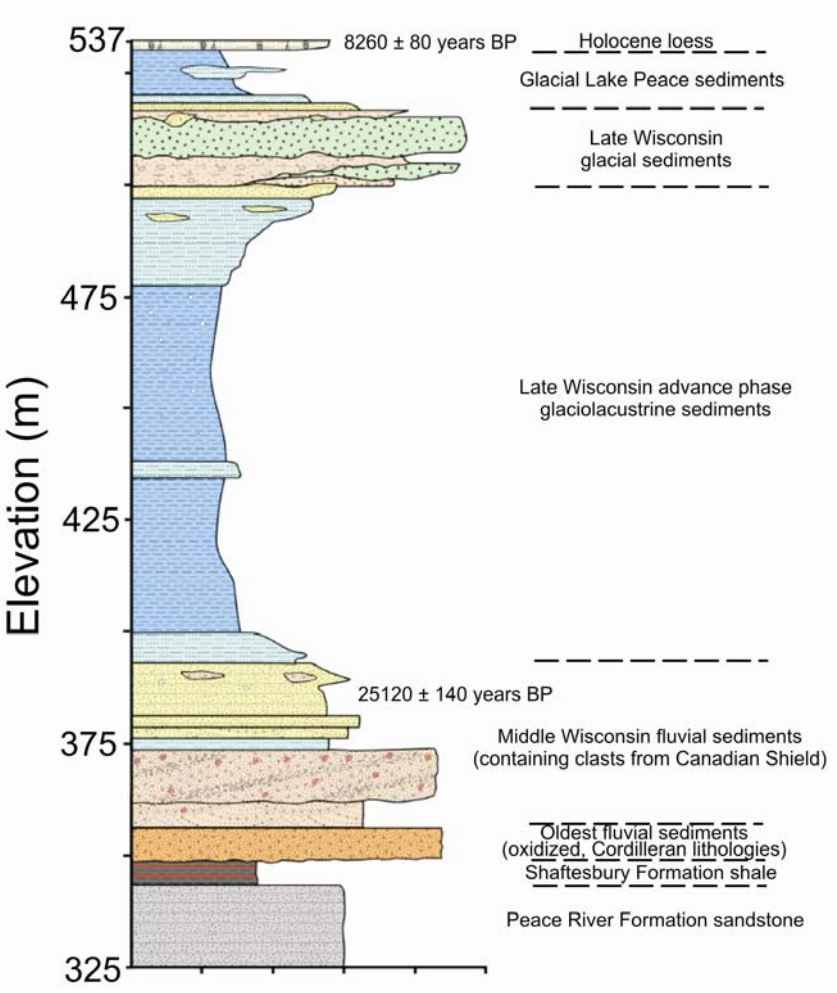

Figure 3.6. Quaternary stratigraphy section as mapped at the confluence of the Heart and Peace Rivers (adapted from Morgan et al., 2008). Figure was reprinted with authorization under the Non-Commercial Reproduction policy of AGS.

Late Wisconsin glacial sediments cap the thick glaciolacustrine package. The lower unit, whose complete stratigraphy includes chaotic stratified glaciofluvial pebble sand and granule gravel with interbeds of diamicton and silt, is interpreted as advance phase glaciofluvial subaqueous outwash that was afterwards overridden by the Laurentide Ice Sheet (Morgan et al., 2008). The upper unit, which is dense, fissile, massive dark grey diamicton of variable thickness, is indicated to be a till sheet from the late Wisconsin Lostwood Glaciation event.

Glaciolacustrine sediments composed of diamicton and massive to laminated silts and clays, of thicknesses up to more than 30 m in some places, were later deposited (Leslie and Fenton, 2001). These sediments were deposited as the Laurentide Ice Sheet retreated to the north and Glacial Lake Peace flooded the region (e.g., Morgan et al., 2008). These low-strength glaciolacustrine clays and silts of Glacial Lake Peace are also prone to sliding, thus causing slope failures in the Peace River area (Davies et al., 2005).

The recent deposits of post-glacial to recent age, consisting primarily of alluvial, colluvial and organic deposits, cap the area (Leslie and Fenton, 2001). The Holocene loess is massive to finely laminated, medium brown with sandy silt matrix and rich organic content (Morgan et al., 2008). The surficial geology and the overall distribution of the surface deposits in the Peace River area are described extensively by Leslie and Fenton (2001).

3.4 Landslides in the Peace River Valley

Mass movements occurred throughout the Holocene and remain active in the Peace River region (Davies et al., 2005). Typically, earth movements in the Peace River Valley occur within the weak layers of the Late Wisconsin Ice Sheet advance-phase overconsolidated glaciolacustrine sediments (Morgan et al., 2008). The slope failures causing these mass movements in the glaciolacustrine

sediments may not be unexpected since the overconsolidated package could possibly have rebounded after the overburden pressure (i.e., the Laurentide Ice Sheet) was removed, which in turn could have initiated water to be absorbed by the sediments leading to the weakening of the rock. Aside from the Late Wisconsin glaciolacustrine sediments that are observed all over the western Peace River Lowlands of Alberta, slope failures also occur in the low-strength Glacial Lake Peace clays and silts and the weak Shaftesbury Formation marine shales (Davies et al., 2005).

Recent mass movement events with rupture surfaces in lacustrine sediments have been documented in the Peace River Lowlands of Alberta including the 1939 Montagneuse River landslide, the 1959 Dunvegan Creek slide, the 1973 Attachie slide, the 1990 Saddle River slide, and the 1990 Eureka landslide (Miller and Cruden, 2002 and references therein). It is interesting to note that the lacustrine sediments, in which the slope failures occurred for the afore-mentioned slides have sand contents of 1% or less with clay and silt making up the rest of the composition (Miller and Cruden, 2002). This suggests that lithology is a crucial influence in landsliding occurrences in the Peace River region and adequate attention should be dedicated to the glaciolacustrine clay and silts sediments. Aside from the lithology of the sediments under consideration, slopes are susceptible to the effect of gravitational forces which may cause them to fail under certain circumstances, e.g. erosion of slope toe, increase in pore pressure due to water saturation, etc. At the study site, the Peace River valley has a considerable elevation variation with values ranging from approximately 340 m a.s.l. at the easternmost end of the ERT line 3 to about 568 m a.s.l. at the westernmost edge of the ERT line 1 (Figure 3.2) and this could, more or less, influence mass movement in the area under certain conditions.

The bare earth LiDAR image, used as an accurate digital elevation model can provide accurate (subject to terrain and signal wavelength) elevation data and a possibility to correctly map landform surficial expressions. As observed on the 1

m high-resolution LiDAR image of the Peace River region (Figure 3.2), the geomorphic representation of the landslide processes in the study area is the hummocky topography (characterized by ridges and troughs) seen on the west side of the river valley (e.g., Davies et al., 2005). This LiDAR image, in combination with borehole data, has been utilized by Morgan et al. (2008) to evaluate the morphology and extent of different slide masses. Moreover, Davis et al. (2005) has generated a digital inventory product of the classifications (consistent with Cruden and Varnes, 1996), locations, and sizes of the Holocene landslides in the Town of Peace River and its environs from existing surficial geology maps.

3.5 Wellbore Geophysical Logs

3.5.1 Introduction

Two geotechnical wells (PR08-03 and PR08-05), coordinated by Alberta Geological Survey (AGS), were spudded and logged in the vicinity of the town of Peace River (Figures 3.1b and 3.2) in December 2008. The common geophysical logs of natural gamma ray (GR), spontaneous potential (SP), electrical resistivity, and density were recorded. Unfortunately, compressional wave interval transit time (DT or sonic) logging was not carried out at that time since this is not a standard measurement in the drilling of geotechnical boreholes. Detailed explanation of the physics of these logs can be found in Ellis and Singer (2007).

GR logs measure the natural radioactivity of formations. The tool contains a detector that measures the gamma radiation emanating from the formation surrounding the borehole. The amount of radioactivity in rocks is dependent on the concentration of potassium, thorium, and uranium. These radioactive elements are abundant in clays and shales; hence GR log is a useful tool in differentiating clays and shales from sandstones, limestones, and dolomites that contain fewer amounts of these elements. The GR tools are normalized to the American

Petroleum Institute (API) standard and the logs are calibrated in API units – ranging from a few API units in salt to about 200 or more in shales. GR can be used in defining rock layer boundaries as well as aid in identifying different lithologies. In the current context, the GR log gives a semi-quantitative measurement of the abundance of potassium containing clay minerals.

The SP log records the electric potential that results from the interaction of the formation connate water, conductive drilling mud, and certain ion-selective rocks (e.g., shale). Adjacent to impermeable shale rocks, the SP curve usually exhibit an almost straight line on the log and this defines the shale baseline. On the other hand, the curve displays departures (deflections) from the shale baseline near permeable formations. The deflection may either be to the left or to the right depending on the relative salinities of the formation water and the drilling fluid. If the formation water is more saline (thus more conductive) than the mud filtrate, the deflection will be to the left; conversely, if the reverse is the case, the deflection will be to the right. Therefore, in addition to using SP log to define lithologies, it can also be used to determine the formation water resistivity. The log is measured in millivolts (mV).

Electrical resistivity tools measure the resistivity of formations. To an extent, dry rocks (excluding metallic minerals) are generally electrical insulators; and the resistivity of a rock is dependent on the resistivity of the formation water, the amount of water present and to a lesser degree on the pore structure (Ellis and Singer, 2007). However, the conductivity of clays, though less than that of metallic minerals, is significantly larger than that of other solids (Knight and Endres, 2005), and so they may have more influence on the electrical conductivity of the rock than the pore fluids. Electric conduction in the formations is partly electrolytic in nature: currents are carried by ions. The resistivities are measured either by passing current into the formation and measuring the resistance or by inducing an electric current through it and measuring its magnitude. For a formation containing saline water (i.e., dissolved salts are present), there is a

sizeable number of conducting ions, hence the resistivity is low. Hydrocarbons, on the other hand, are quite resistive and so the formation resistivity will be high. However, during interpretation, it is necessary to examine the porosity because it has an effect on the resistivity. For constant water saturation, as porosity increases, true resistivity will decrease (Ellis and Singer, 2007). The logs are measured in ohm-meters and displayed in logarithmic scale because of the wide range of values that can be encountered.

Density logs measure the density of the formation and are used basically as porosity logs. Other uses include detection of gas, determination of overburden pressure and the computation of impedances (in combination with sonic log) for the generation of synthetic seismogram. The tool emits gamma rays which are Compton-scattered by electrons in the formation. The number of scattered gamma rays detected by the tool is related to the electron density of the formation and this in turn is related to the bulk density. Bulk density is dependent on the matrix density, formation porosity and density of the fluids in the pores. Compensated density log is derived from 'corrected' density measurements, to account for mudcake and irregularities in the borehole. Density logs are normally displayed in g/cm^3 or kg/m^3. Porosity can be computed from the density log by a simple equation, if the mineralogy of the formation is known.

Acoustic properties of rocks are measured with tools like sonic (DT) which records the transit times of the compressional wave through the formation in units of μs/m or μs/ft. The P-wave material velocity of the formation influences the transit times and it is a function of the elastic properties (e.g., stiffness and rigidity) and density of the media. Moreover, the transit time is dependent on the formation matrix material, cementation, type of fluid in the pores, and pressure (Ellis and Singer, 2007). Conventional acoustic logging tool consists of an acoustic energy transmitter and a receiver operating in the frequency range of about 20 kHz. Development in the tool design led to compensated tools containing a pair of transmitters and receivers to account for borehole

irregularities. This tool would have been invaluable to the current study but unfortunately was not run in the wells.

3.5.2 Wellbore Analysis

3.5.2.1 Wellbore PR08-03

With reference to the ground level (i.e., 445.3 m a.s.l.), wellbore PR08-03 has a total depth of about 125.6 m that just barely grazed the top of the Shaftesbury formation at 322.5 m a.s.l. (Figure 3.7). The geophysical logs, lithologies, and the defects (shear planes and fractures) encountered in the wellbore are displayed together in a well section for easy interpretation (Figure 3.7). The shear planes are surfaces along which movement has taken place, while fractures are cracks or discontinuities in the formation. Roto-sonic drilling, which does not utilize drilling fluids or air, was employed for the wellbore from ground surface to 337 m a.s.l., while the remainder of the borehole was drilled with wet-rotary system.

The lithology of the sediments based on the clay contents are easily distinguished on the GR log (Figure 3.7). In PR08-03, clay-rich deposits are depicted by high GR values (> 74 API units) while sediments with lower clay contents have lower values of GR (< 60 API units). It is important to point out that the lithology term ‘diamicton’ is used here generally in the context of poorly sorted till with varying mixture of clay, silt, and sand. Hence, as observed in the composite well log display (Figure 3.7), the diamicton lithologies are characterized by a broad range of GR values. A sandy zone (< 40 API units) at 300 m a.s.l. with little or no clay, which lies directly above the Shaftesbury bedrock, is inferred to be a fluvial formation in contrast to lacustrine sediments, rich in clays that are usually deposited in calm water conditions. Lack of additional information precludes establishing the origin of the fluvial sediments which could be preglacial or of Middle Wisconsin age. The substantial amount of clay in the thick wellbore depth section of 397 m a.s.l. to 344 m a.s.l. is the basis for interpreting the zone as Late Wisconsin overconsolidated glaciolacustrine deposits (Figure 3.7). The possible

top of this overconsolidated package was interpreted to be at 397 m a.s.l. (with question marks inserted to signify uncertainties), just into the sandy formation since it is expected that there exists a gradual coarsening upward in the glaciolacustrine sediments top section (Morgan et al., 2008).

Formation water is expected to have a major effect on the electrical conductivity of a rock through ionic conduction. Although there was moisture observed within the core sections of the rocks drilled with the roto-sonic drilling system for wellbore PR08-03, however significant amount of water was not encountered in any of the depths to allow characterizing any unit as having higher water content than the others. Assuming the groundwater in the area has constant electrolytic content, the identical water saturation in each individual formation may not be the only key influence of electrical conductivity in this wellbore. Significantly, the trends of the resistivity and GR logs are observed to have an inverse relationship with each other; vis-à-vis decrease in GR corresponds to an increase in the resistivity values and vice versa. This suggests that the electrical conductivities of the formations are mostly influenced by their respective clay contents, with higher amount of clay correlating with lower resistivity. In near surface materials, the conductivity of clays is orders of magnitude greater than other solids that are non-metallic (Knight and Endres, 2005), reason being the surface conductivity associated with clay minerals.

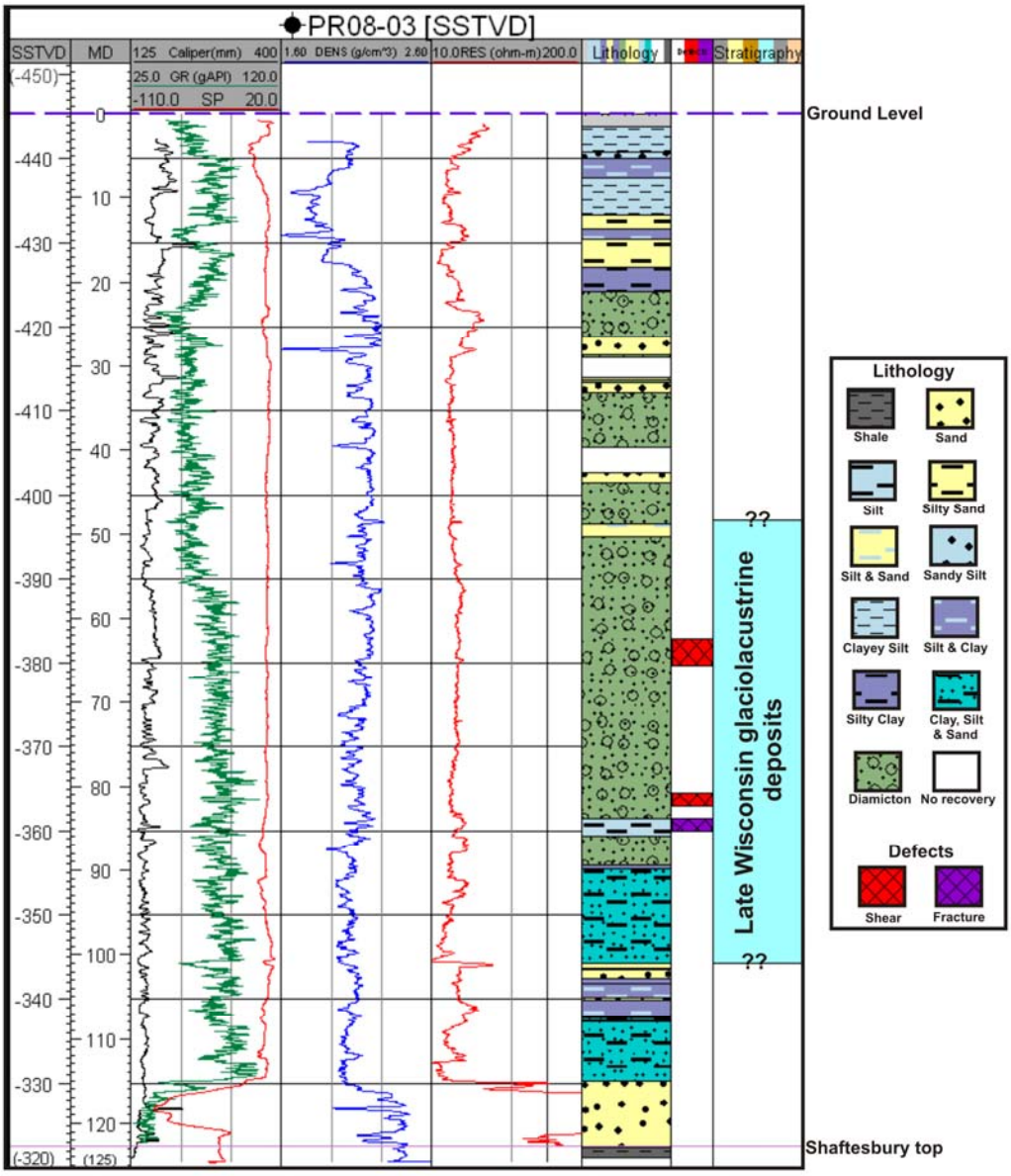

Figure 3.7. Geophysical logs in well PR08-03. The first track is the true vertical depth in relation to sea level (SSTVD) with negative values signifying depths above sea level; the second track is measured depth referenced from ground level (i.e., 445.3 m a.s.l). The third track contains GR (green), SP (red), and caliper (black) logs. The compensated density log is displayed in the fourth track, resistivity log in the fifth track and the lithology is shown in the sixth track. The seventh track contains the depths in the borehole that has defects (shears and fractures). The probable depth section of the Late Wisconsin deposits (indicated with question marks) is displayed in the last track.

There appears to be no noticeable unusual response on the available geophysical logs at depths where there exist either a shear plane or fracture in the wellbore (Figure 3.7). Nevertheless, all the recorded borehole defects occur in the apparent Late Wisconsin glaciolacustrine sediments stratigraphic section. This is consistent with the slope failures experienced in these overconsolidated deposits (Davies et al., 2005) which may possibly be naturally low strength materials or weakened by a variety of normal processes. In addition to the occurrence of the shear planes in clayey formations (relatively higher GR values in comparison to sandy beds), slickensided surfaces were also observed in the respective cores. Particularly, the top of the core at 381.29 m a.s.l. in the wellbore, abundant with shear planes, contains slickensided clay (fissured clay) which is intersected by fractures whereby water may percolate through easily. Notably, hydration of clay minerals results in loss of cohesion associated with rock softening (Cruden and Varnes, 1996) and this could reduce the shear strength of the materials, thus leading to the abundant shear planes encountered in the borehole core.

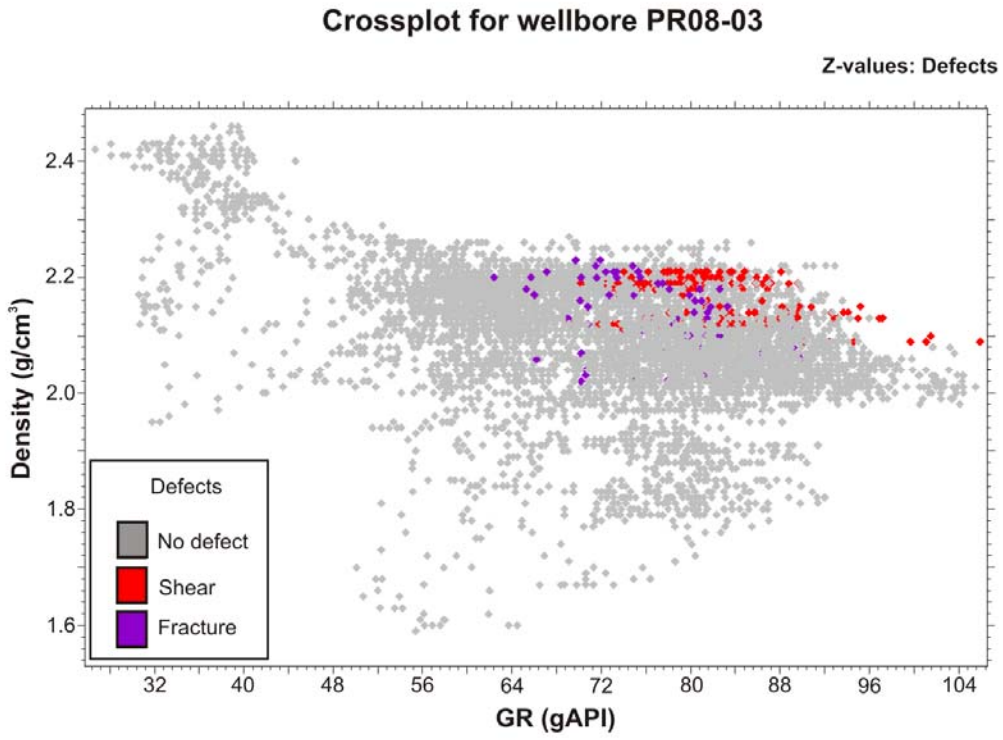

Figure 3.8. GR vs. density crossplot for wellbore PR08-03 with data points colored according to the defects (shear planes and fractured zones).

Crossplots are useful in revealing how different log combinations correlate with one another. A crossplot of the GR, density, and defects (shear planes and fractured zones) as x-, y-, and z-coordinates respectively was generated (Figure 3.8) in order to understand the relationship between the log responses and the defects. The crossplot was generated by plotting the value of the GR log at each depth against the corresponding density value and then coloring the data point with the defect observed at that depth. As earlier noted, it is apparent from the crossplot that the defects occur in clayey formation (GR values > 62 API units). However, the shear planes do not seem to correspond to any definite value of densities from which further inferences can be drawn. Likewise, the fractured zones do not appear to show any particular correlation with the density values. Due to the lack of sonic log in the wellbore, it is uncertain if a crossplot involving DT, density, and the zones with defects would have a better correlation.

3.5.2.2 Wellbore PR08-05

A composite display of the geophysical log responses, lithologies, and defects (shear planes and fractures) of wellbore PR08-05, situated on the eastern side of the Peace River (Figure 3.2) was generated (Figure 3.9). The shear planes are surfaces along which movement has taken place, while fractures are cracks or discontinuities in the formation. PR08-05 was drilled from 538.35 m a.s.l. (ground level) to a total depth of about 177 m through the Shaftesbury Formation bedrock encountered at ~ 373.6 m a.s.l. (Figure 3.9). Roto-sonic drilling was employed for the wellbore from ground surface to depths of about 114 m. This borehole is located on the other side of the Peace River beyond the geophysical research area of the seismic and ERT surveys (Figure 3.2). Despite this, the well was intentionally sited to intersect as complete an undisturbed section of the Quaternary sediments as possible; and as such it is important for purposes of comparison.

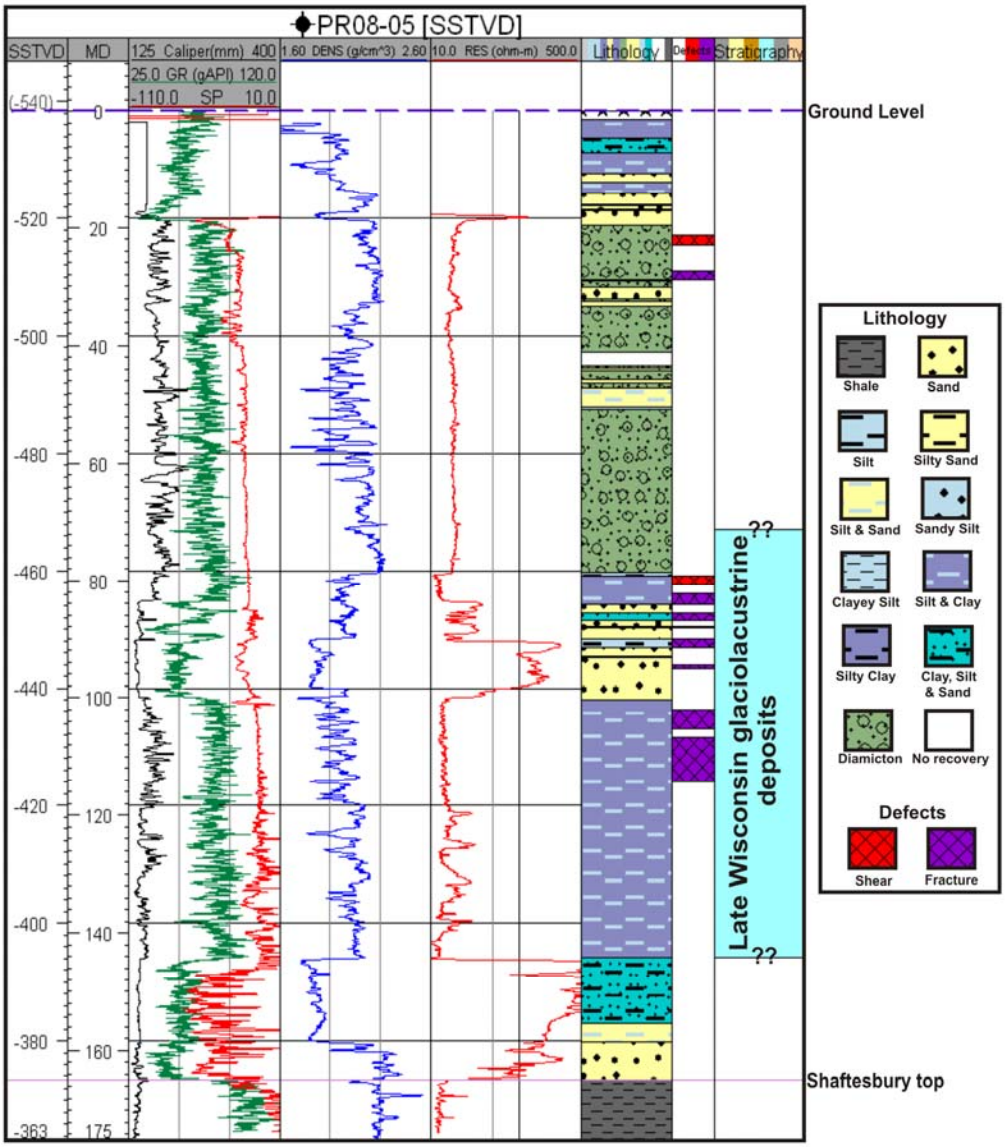

Figure 3.9. Geophysical logs in well PR08-05. The first track is the true vertical depth in relation to sea level (SSTVD) with negative values signifying depths above sea level; the second track is measured depth referenced from ground level (i.e., 538.35 m a.s.l). The third track contains GR (green), SP (red), and caliper (black) logs. The compensated density log is displayed in the fourth track, resistivity log in the fifth track and the lithology is shown in the sixth track. The seventh track contains the depths in the borehole that has defects (shears and fractures). The probable depth section of the Late Wisconsin deposits (indicated with question marks) is displayed in the last track.

Characterized by high GR values (> 90 API units) and low resistivity values (> 14 ohm-m) indicating deposition in marine (electrically conductive) environment, the Shaftesbury Formation is apparent in the PR08-05 wellbore geophysical logs signature. Similar to PR08-03 wellbore, the trends of the resistivity and GR logs of PR08-05 appear to have an inverse relationship with one another, indicating the influence that the clay content of each respective formation has on its electrical conductivity.

Late Wisconsin overconsolidated glaciolacustrine deposits was interpreted to encompass the clayey formation in the wellbore section from 467 m a.s.l. to 394 m a.s.l. (Figure 3.9). In like manner as the previously examined wellbore, most of the shear planes and fractures occur in the Late Wisconsin glaciolacustrine sediments stratigraphic section (Figure 3.9). However, the fractures were not limited to only clayey and silty formations but occur also in a sandy unit at about 443 m a.s.l. Given that porosity and associated fluid content is the key reason for density differences in the near surface region (Knight and Endres, 2005), this particular sand unit, with top at 446.9 m a.s.l., can be interpreted to have a relatively high porosity as inferred from the low value of the bulk density (~ 1.87 g/cm^3). The sandy formation, that is also described by relatively high resistivity, is however relatively dry and overconsolidated. It is unknown if the fractures observed in this sandy unit occurred in naturally dry conditions or wet circumstances with a subsequent water-drainage attributable to overconsolidation processes.

Shear planes and fractures were also noticed to occur in shallow depths at 517 m a.s.l. and 510.9 m a.s.l. respectively outside the interpreted Late Wisconsin glaciolacustrine stratigraphic wellbore section (Figure 3.9). Based on the comparatively high values of GR (> 70 API units) and bulk density (> 2.1 g/cm^3), this wellbore section is presumed to correspond to the Glacial Lake Peace glaciolacustrine sediments. This is in agreement with some of the slope failure

events in Peace River area which were caused by the low-strength glaciolacustrine clays and silts of Glacial Lake Peace (Davies et al. 2005).

A crossplot of GR, density, and zones with defects (i.e., shear planes and fractures) for wellbore PR08-05 (Figure 3.10) was generated to reveal the correlations between the geophysical logs and the defects. The crossplot was generated by plotting the value of the GR log at each depth against the corresponding density value and then coloring the data point with the defect observed at that depth. The relationship between the resulting data points is not apparent and no clear correlation could be drawn from their distribution. One can only conclude that most of the shear planes and fractures occur in silty and clayey formations.

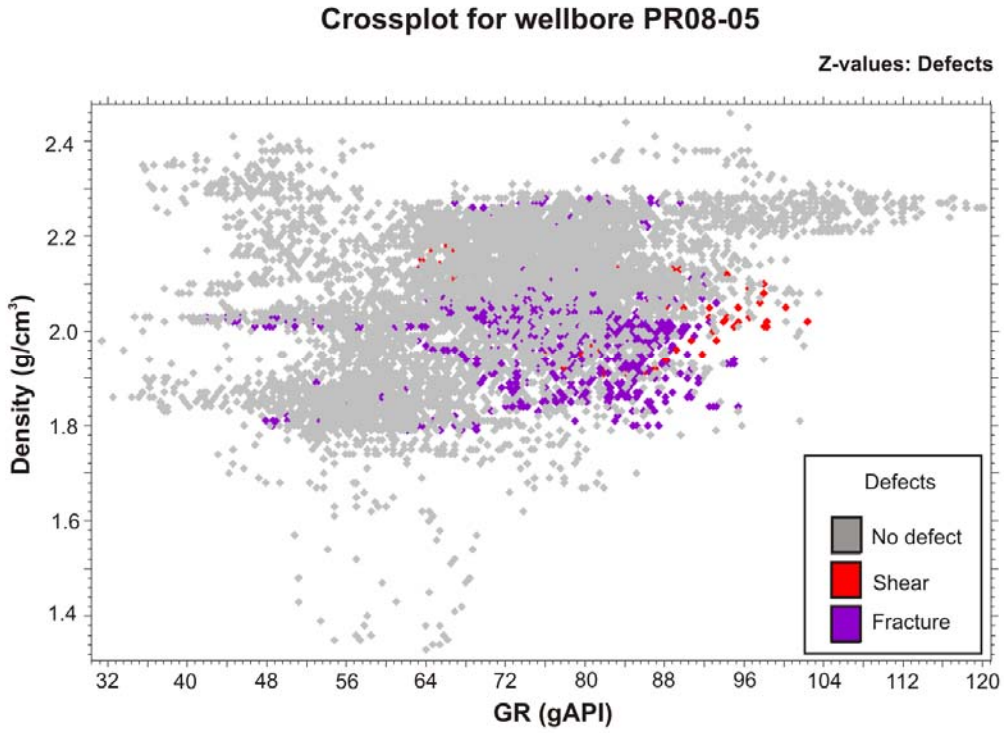

Figure 3.10. GR vs. density crossplot for wellbore PR08-05 with data points colored according to the defects (shear planes and fractured zones).

3.6 Summary

The geology of both the Cretaceous bedrock and the Quaternary sediments of the Peace River area have been described in this chapter. The lowermost exposed bedrock in the study area is the Peace River Formation that lies stratigraphically underneath the Shaftesbury Formation shales. Above the Shaftesbury Formation is the Dunvegan Formation that underlies the Smoky Group. The Quaternary sediments were observed to be deposited mostly on top of the Shaftesbury Formation in the study area. Notable packages within the Quaternary stratigraphy are the thick deeply-buried overconsolidated glaciolacustrine sediments that are present throughout the western Peace River Lowlands of Alberta and the low-strength glaciolacustrine clays and silts of Glacial Lake Peace. These aforementioned Quaternary units are prone to sliding, causing slope failures in the Peace River area. Similarly, previous studies showed that slope failures are common in the shales of the Shaftesbury Formation. Thus, it can be inferred that lithology plays a major role in slope stability at the study area. This deduction was also supported by the results of the analyses performed on the geophysical logs of some wellbores in the study area for the reason that most shear planes and fractures observed in the wellbores occur predominantly in silty and clayey formations.

Chapter 4

Seismic Methodology

In this chapter, the seismic methodology employed in the study of the landslide will be described in detail. The chapter will begin with an overview about seismic methods utilized in this research, i.e., seismic reflection, seismic refraction tomography, and vertical seismic profiling. Seismic reflection dataset acquisition, with its corresponding processing optimized to suppress source-generated noise will later be discussed. The procedure related to the generation of a velocity distribution of the subsurface via the use of the associated refraction waves from the collected seismic data will also be explained in this chapter. Subsequently, the acquisition and processing of the vertical seismic profiling datasets will be described.

4.1 Seismic Overview

The seismic method, one of the commonly used geophysical techniques to explore the subsurface, involves the generation of elastic waves and the subsequent detection of the seismic energy by some type of receiver after propagating across a portion of the earth. Seismic waves propagating through the earth are called body waves, while those travelling along the earth's surface are described as surface waves.

Body waves with particle motions parallel to the direction of wave propagation are labeled P (or compressional) waves, whereas body waves that have particle motions perpendicular to the wave propagation direction are called S (or shear) waves. The velocity of P-wave is influenced by the bulk modulus (a measure of

resistance to compression), shear modulus (a measure of rigidity), and density of the media through which the wave is propagating and it is normally faster than the S-wave velocity that is only dependent on the shear modulus and density of the material.

Surface waves are slower than body waves and are classified as Rayleigh or Love waves. Rayleigh waves, with elliptical particle motion retrograde to the wave propagation direction, are created by the interaction of P- and S-waves. In contrast, Love waves, that are SH (S-wave with particle motions constrained in a horizontal plane) equivalents, require a velocity gradient with depth in order to be generated and their particle motions are entirely horizontal and perpendicular to direction of the wave propagation. Though surface waves, by means of spectral analysis method, can be used for estimating the S-wave velocity of near surface materials (Pelton, 2005), such technique was not exploited in this research.

Although body waves are used in the investigation of the subsurface without any particular threshold to the depths of investigation, the focus of this thesis is limited to its application for near-surface exploration, sometimes called high resolution seismology. Near-surface seismic exploratory techniques, as utilized in this research, can be broadly categorized into (1) seismic reflection, (2) seismic refraction, and (3) vertical seismic profiling. P-waves are mostly used in high resolution seismic exploration, but S-waves are increasingly being used as well due to advances in technology.

The seismic reflection method generates a structural image of the subsurface from the reflections emanating from various geologic units in the earth's interior (see illustration in Figure 4.1a). Seismic wave reflections occur where there are acoustic impedance contrasts in the earth's geologic layers. The acoustic impedance of a material is the product of its density and the velocity of the seismic wave (i.e., P or S) propagating through it. The amplitude of the reflected

wave relative to the incident wave is represented by the reflection coefficient *R*, expressed for normal incidence by

$$R = \frac{\rho_2 V_2 - \rho_1 V_1}{\rho_2 V_2 + \rho_1 V_1}, \qquad (4.1)$$

where ρ_1, V_1, ρ_2 and V_2 are the density of first medium, velocity of first medium, density of second medium, and velocity of second medium respectively (Figure 4.1a). Typical 2D acquisition geometry of seismic reflection exploration consists of a seismic energy source activated along the length of a string of receivers with a range of receiver offsets (with offset referring to the distance between the source and a particular receiver). There is a wide range of seismic sources that could be used on land seismic exploration, including vibrator mounted on a truck, weight drop, sledge hammer, dynamite, etc. Receivers on land are mostly geophones that are sensitive to ground movements and convert these motions to electric signals to be recorded on seismographs. Data collected during seismic reflection surveys are not limited to reflected waves only, but other waves like refracted and surface waves that could be described as noise in this context are also inevitably recorded. To enhance the reflected events over the noise, some processing steps are required and they will be discussed fully in a later section of this chapter. For further information about seismic reflection methods, the reader is referred to Steeples and Miller (1990; 1998).

The seismic refraction method provides information about the seismic velocities and thicknesses of subsurface geological units. The geometrical basis of the seismic wave refraction technique is the critical refraction of rays at velocity contrast boundaries with the condition that velocity increases with depth (Figure 4.1a). As a result of this condition, seismic refraction analysis will possibly produce incorrect results in areas where velocity inversion exist (i.e., a velocity decrease across a boundary). There are numerous methods used to interpret refraction data. Methods include intercept-time (e.g., Zirbel, 1954); reciprocal or delay-time methods like Gardner method (Gardner, 1939), plus-minus method (Hagedoorn, 1959), and generalized reciprocal method (Palmer, 1981); and

generalized linear inversion scheme involving ray tracing (e.g., Hampson and Russell, 1984).

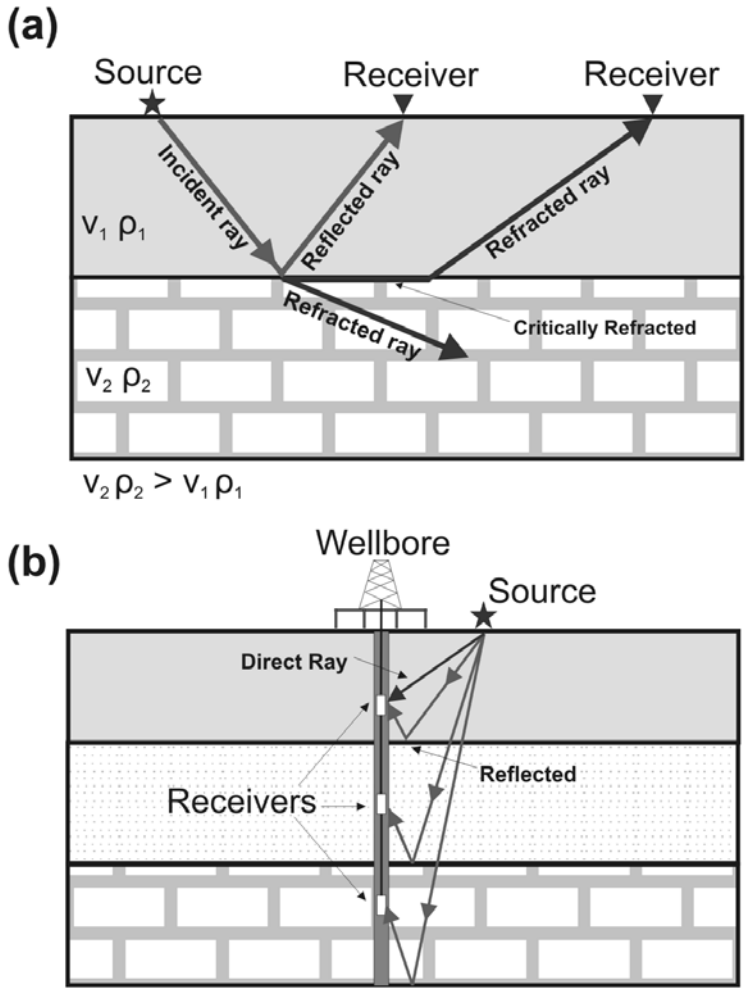

Figure 4.1. (a) Cartoon showing seismic reflection and refraction concepts. *V* and *ρ* are velocity and density respectively. (b) Demonstration of a zero-offset vertical seismic profiling.

However, simple refraction analysis may not be adequate in accurately modeling complex subsurface structures. Moreover, seismic rays can be continuously refracted as a result of subsurface vertical positive velocity gradient in a scenario described as turning-ray model, prior to being received at the surface. An

application of such seismic turning-ray model is observed in refraction tomography that involves the inversion of first arrival (i.e., direct and refracted waves) traveltimes from multiple sources and receivers to generate a seismic wave velocity image of the subsurface. Tomographic inversion can also be applied effectively in areas where there are lateral velocity variations to provide useful velocity information. Furthermore, seismic refraction tomography may be able to provide some knowledge about low velocity layers sandwiched between higher velocity zones, if not from the resulting subsurface velocity distribution image, at least from the analysis of the corresponding raypath coverage. Examples of turning-ray tomographic inversion algorithm include Zhu et al. (1992) and Stefani (1995). Additional information about seismic refraction method may be found in Green (1974) and Lankston (1989).

Zero-offset vertical seismic profiling (VSP) involves the use of 3-component geophones placed at various depths in a wellbore with the seismic source located on the surface near the wellhead (Figure 4.1b). The data acquired from a zero-offset VSP can be used to determine the one-way traveltime to various subsurface depths (i.e., checkshot survey) and the acoustic reflectivities near the borehole for the purpose of conducting a 'tie' with the seismic reflection data. Since the depths of the 3-component geophones are accurately known in VSP surveys, performing a data 'tie' with the reflection data allows identification of particular geologic units and the corresponding depth estimates. However, a raw VSP data contains a strong-amplitude downgoing wavefield that normally masks the desired upgoing reflections; therefore wavefield separation techniques are applied during VSP data processing to create an appropriate image of the reflections.

In a walkaway VSP configuration, a 3-component geophone is held at a fixed depth while the seismic source is moved along the surface at varied offsets to the wellhead; such VSP type produces a structural image of the subsurface in the vicinity of the borehole. Principles and applications of VSP can be found in

Hardage (2000); Kennett et al. (1980); Dillon and Thomson (1984); and Oristaglio (1985).

4.2 Seismic Reflection

A high-resolution 2D seismic campaign was carried out at the Town of Peace River in June 2009. The seismic survey was intended to image the Cretaceous bedrocks (i.e., Shaftesbury and Peace River Formations) and the Quaternary sediments above them for the purpose of understanding the subsurface structure and processes of the Peace River landslide. Adequate consideration was given to the design of the seismic survey to optimize the vertical and lateral resolutions of the seismic reflection profile. Predictably, near surface high resolution seismic reflection data are typically affected by different phases of source-generated noise because of the closeness of the targets to the surface; therefore the reflection data was processed in such a way as to suppress these coherent noises. In summary, this section of the thesis deals with the seismic reflection data acquisition and the processing sequence employed.

4.2.1 Data Acquisition

4.2.1.1 Seismic Data Acquisition

The high-resolution 2D seismic line was acquired in west-east direction over a survey length of ~ 4.8 km (Figures 3.1 and 3.2). The total 2D line was acquired in six cable-spread length segments over a 3-day period. The 2D survey was conducted parallel to Highway 2, inside the northern ditch of the highway, within the Alberta Transportation right-of-way on the west side of the Town of Peace River. We realized that traffic noise along this corridor would be problematic, but both local culture and topography tightly restricted where the survey could be run. The 2D seismic line overlaps the surface over disturbed and undisturbed ground as established from the high-resolution LiDAR image (Figure 3.2).

A summary of the acquisition parameters is outlined in Table 4.1. The P-wave energy source of the survey was the University of Alberta's 6000-lb IVI Minivib™ unit (built by Industrial Vehicles International of Tulsa, OK), operated with linear sweeps of 7 s period from 15 Hz to 250 Hz at a force of about 17790 Newtons (4000 pounds). The IVI Minivib™ unit could not be operated steadily at its vibrator plate maximum force of 26690 Newtons (6000 pounds) due to some mechanical problems encountered at the commencement of the seismic program.

Table 4.1. Acquisition parameters for the 2D seismic survey.

Parameter	Value
2D line direction	West-East
Length of profile	~ 4.8 km
Source	6000-lb IVI Minivib™ unit
Source frequency	15-250 Hz
Source type	Linear
Source length	7 s
Source spacing (average)	24 m
Number of sweeps per shotpoint location	5-9
Number of unique shotpoints	185
Number of unique stations	1062
Receivers	40-Hz single geophones
Receiver spacing	4 m
Recording instrument	Geometrics Geode™ system
Number of channels	168-192
Sampling interval	0.5 ms
Record length after cross-correlation	1.19 s
Average nominal fold	~ 22

The seismic traces were acquired with 40-Hz geophone singles at a 4 m spacing using 240-channel semi-distributed seismograph that includes eight 24-channel Geode™ (manufactured by Geometrics Ltd., San Jose, CA) field boxes, primarily designed for near-surface seismic surveys, connected via field intranet cables (for digital data transfer) to the recording computer. The sampling rate of the data was 0.5 ms and the total recorded field record time was 8.19 s to account for the vibroseis sweep duration time of 7 s and the desired geologic record length of 1.19 s. Cross-correlation of the seismic traces with the sweep pilot signal is required to collapse the vibroseis sweep into a spike; this was carried out in the field and the final records were saved in SEG-2 format. It is important to point out that the autocorrelation of the sweep pilot trace is a zero-phase Klauder wavelet defined by the sweep duration and its low and high frequency values (Geyer, 1970).

Good coupling of the seismic source and receivers to the ground are usually necessary for maintaining a high signal-to-noise (S/N) ratio in the recorded traces. The disturbed mass in landslides are generally uncompacted and so there is a high possibility of non-perfect coupling of the geophones and the Minivib™ unit's vibrator plate with the ground in these areas. This is apparent in the shallow portion (< 200 ms) of both positive and negative offsets of a raw correlated shot record (Figure 4.2a). The traces associated with the negative offsets of the shot gather, that were possibly recorded over undisturbed ground, have better events continuities and higher amplitudes than those related to the positive offsets, likely conducted over a broken up area (Figure 4.2a). The gradual decline in the amplitudes of high seismic frequencies as observed in the amplitude spectrum of the average of all the correlated traces (Figure 4.2b) could also be an indication of a non-perfect coupling and attenuation. Although efforts were made during the seismic acquisition to ensure good source and receiver coupling with the ground as much as possible, near perfect coupling could not be achieved, possibly because of the inherent complex nature of the heterogeneous surficial and

landslide materials. However, trace gaining, carried out during seismic data processing, may facilitate boosting of the amplitudes of the affected traces.

Landslides mass can be very heterogeneous and complex in nature causing it to be a bad medium for seismic wave propagation as a result of wave scattering and dispersion. This is possibly one of the reasons seismic reflection has not been used extensively to investigate landslides. A shot gather recorded in one of the areas believed to be affected by the landslide processes (Figure 4.2c) reveals the difficulties in distinguishing first arrivals and strong shallow continuous reflection; this could be an indication of the broken up nature of the materials in this area.

The surface topography along the 2D line location was uneven, characterized by hummocky features, and covered with sticky mud in many places that caused the Minivib™ unit to get stuck a number of times, sufficient to warrant the use of a towing truck to pull free; for this reason a constant source spacing of 24 m could not be maintained all through the length of the survey. Accordingly, closer seismic source spacing was utilized in some places to balance the inability to sweep the vibroseis in some mud-covered areas in an attempt to maintain a good nominal fold. Implementing this workaround resulted in irregular fold coverage with some areas having folds as low as 5, some other areas as high as 40, and an ensuing average nominal fold of about 22. To further increase the subsurface fold, one can attempt incorporating gathers from far offsets shots. However, interference between reflected waves and refracted waves crops up at large offsets, with the separation of these arrivals quite difficult because of their similar frequency contents and apparent velocities (Pelton, 2005); hence the incorporation of these far offset shot gathers with the data may be detrimental in high resolution shallow reflection surveys. Large offsets, generally affected by small normal moveout (NMO) associated with deep high-velocity reflectors and frequency distortion for shallow events following NMO corrections (Yilmaz, 2001) are other problems encountered with integrating far offset records into common midpoint

(CMP) bins in reflection seismic method. Nevertheless, gathers associated with far offset shots were recorded during the data acquisition for the purpose of seismic refraction tomography generation.

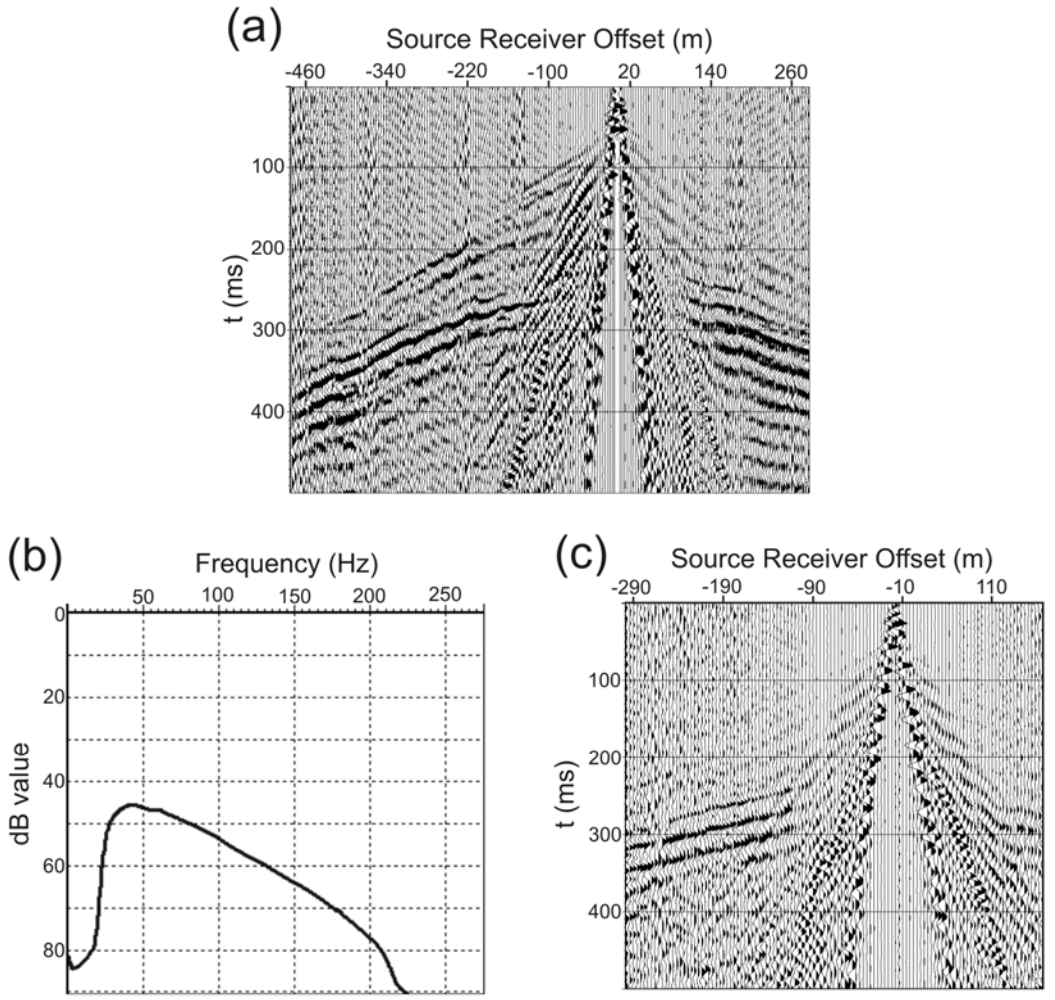

Figure 4.2. (a) Raw shot record (shotpoint 1120) acquired over possible undisturbed ground at negative source receiver offsets and disturbed ground at positive offsets highlighting differences in coupling. (b) Amplitude spectrum of the average of all correlated traces showing gradual decline in energy as frequencies increase. (c) Shot record (number 1150) acquired over a possible unstable area with obscured first arrivals indicating poor seismic wave medium.

Traffic noise was a potential problem in the collected data because of the proximity of the seismic line to a major highway. Likewise, ground roll noise that often overshadows weak reflections in near-surface land seismic acquisition could be present significantly in the recorded data. To minimize the effect of the highway traffic noise and the ground roll that often has much of its energy concentrated in the low frequencies, high frequency 40-Hz geophones (manufactured by OYO Geospace Company) as against low-frequency 14-Hz phones were utilized. The downside of this choice is the reduction in the overall bandwidth of the data; but this is likely balanced out by the enhancement of the near-surface reflections due to the anticipated suppression of the ground roll. As expected, it was observed that traffic noise increased significantly during the daytime over what was experienced at night; therefore the number of source sweeps at individual shotpoint location was optimized to vary from about 5 at nighttime to 9 at daytime in order to achieve a high level of S/N ratio after stacking. During high traffic times, control of each shot was shifted to the vibrator operator who was more easily able to monitor traffic approaching or on the line.

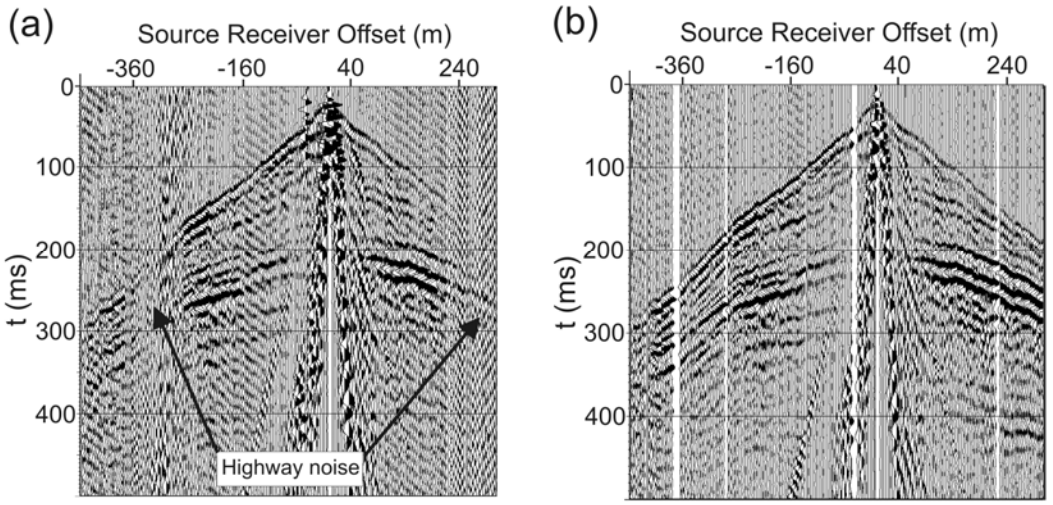

Figure 4.3. (a) Raw shot gather (shotpoint 1498) contaminated by highway noise. (b) Resulting shot record after surgically muting the affected traces in (a) and other shot gathers acquired at the same location and vertically stacking them.

In order to reduce the effect of random noise on shot gathers, field records at the same location from repeated source activations are basically added in a practice called vertical stacking. Vertical stacking was not carried out in the field because of the masking of the reflection data by highway noise in some parts of the shot gathers (Figure 4.3a). After the field activities, the traces that were affected by the traffic noise on every shot gather were surgically muted before performing the vertical stacking of gathers from the same location. This process increased the S/N ratio considerably (Figure 4.3b).

Vertical resolution, which can be described as the ability to separate two vertically close events, was one of the factors taken into account during the seismic survey design. A geologic layer is well resolved vertically if unique reflections from the top and base of the layer are adequately separated in time to be distinguishable. Noise causes the broadening of wavelet and this forces the limit of resolution to $\lambda/4$ (Widess, 1973), where λ is the predominant wavelength of the incident wavelet. As a consequence, any layer thinner than one-fourth of the wavelength of the incident wave may not be vertically resolved in the presence of noise; thus in order to improve the resolution, the wavelength needs to be shortened. Consider the relationship between the wavelength λ, velocity v, and the predominant frequency f, given by

$$\lambda = \frac{v}{f}. \qquad (4.2)$$

It follows that for any given layer velocity, higher frequencies are required to facilitate the enhancement of the seismic vertical resolution. Consequently, sweeps of frequencies up to 250 Hz were generated by the seismic source for satisfactory vertical resolution. In addition, the recorded data was sampled at a rate of 0.5 ms in an attempt to accommodate the high frequencies.

Lateral resolution deals with the ability to distinguish two close reflecting points positioned horizontally. The width of the first Fresnel zone, which is the segment of the surface over which reflected waves will interfere constructively, is a

measure of lateral seismic resolution. In general, two reflecting events that fall within a Fresnel zone may be deemed indistinguishable; therefore, the narrow the width of the Fresnel zone the higher the spatial resolution. The Fresnel zone width does not only depend on the incident wave frequency, with relatively high frequency narrowing the Fresnel zone, but also on the velocity and the depth of the reflecting surface (Yilmaz, 2001). Considering that the Fresnel zone typically increases with depth resulting in the deterioration of lateral resolution with depth (Yilmaz, 2001), and our inability to control the velocity and depth of reflectors, we endeavored to preserve high frequencies in the recorded data.

If a seismic wavefield is not sampled adequately enough in time and space, distortion or aliasing of the recorded data may arise. Temporal aliasing can be avoided if the sampling interval Δt of the seismic signal is small enough that the Nyquist frequency is larger than the maximum frequency of the data; with the Nyquist frequency f_{Nq} expressed as

$$f_{Nq} = \frac{1}{2\Delta t}. \qquad (4.3)$$

The Nyquist frequency of the acquired seismic dataset is 1 kHz, as evaluated by Equation 4.3 with 0.5 ms being the sampling rate. With a maximum bandwidth frequency of 250 Hz, the recorded seismic data is not at risk of being affected by temporal aliasing.

Spatial aliasing that relates to how the seismic signal is sampled in space can cause artifacts to appear in shot gathers and even processed seismic profile. The steeper the dip of a seismic event, the lower is the frequency at which spatial aliasing occurs (Yilmaz, 2001). Spatially aliased ground roll coherency can be destroyed by decreasing the geophone interval considerably (Steeples and Miller, 1998); but there are limitations to accomplishing this during data acquisition because substantial reduction of the receiver spacing is subject to cost and logistical constraints. Due to these reasons, the geophone spacing of 4 m could not be further decreased during the data acquisition. Thus, with a geophone

spacing of 4 m, surface waves travelling at 300 m/s are at risk of being spatially aliased at frequencies greater than 38 Hz. Spatial aliasing of surface waves was not pronounced in our dataset. In addition, there is a chance that events with large dips contained in the seismic data could be spatially aliased at high frequencies. However, during data processing, the choice of an optimal CMP bin size could minimize spatial aliasing for dipping reflections. This will be discussed in detail in a later section.

4.2.1.2 Geodetic Data Acquisition

Geodetic information is required for every seismic trace for the intention of establishing proper geometry before any further processing step is carried out. Geodetic data was collected with the University of Alberta's Trimble Differential Global Positioning System (GPS). The differential GPS, an improvement to GPS, makes use of a stationary and roving receiver to determine position and elevation with centimeter precision. Each point surveyed during the acquisition program was specified in Universal Transverse Mercator (UTM) Zone 11 North coordinate system referenced to North American Datum of 1983 (NAD83) to provide easting, northing, and elevation values.

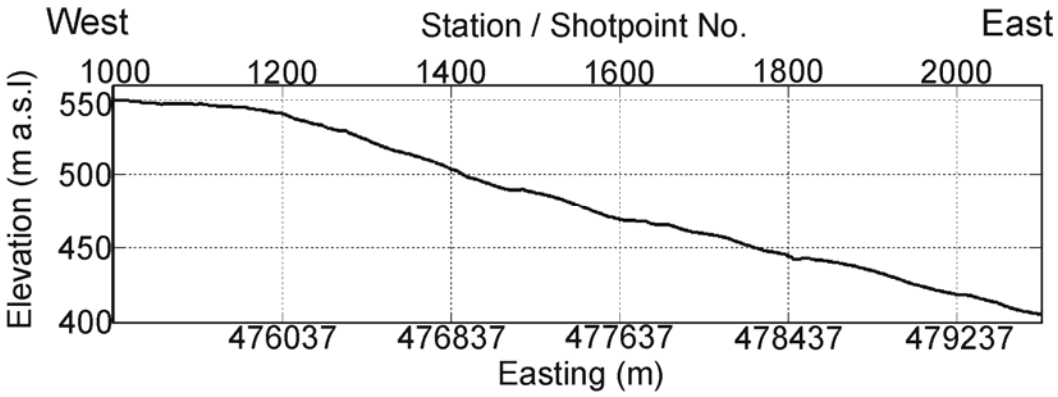

Figure 4.4. (a) Elevation profile along the seismic line in m above sea level. The corresponding UTM Zone 11N coordinates of the field-stations are also shown.

Most of the shotpoint and field-station (every third geophone) locations were surveyed during the geodetic data collection. The coordinates of the in-between field-station geophones and the unsurveyed locations were linearly interpolated such that every shot and receiver position on the 2D seismic line has an associated easting, northing, and elevation. These coordinates were subsequently saved in ASCII format for loading into Vista® seismic processing software (GEDCO, Calgary).

The substantial topography variation from west to east along the 2D seismic survey line is apparent on the surveyed elevation profile (Figure 4.4). Such considerable elevation differences along the line warrants accurate measurements for the purpose of calculating statics corrections for the reflection profile during seismic processing. To this end, the elevation data as obtained from the Differential GPS was validated with the elevation values from the high resolution LiDAR data.

4.2.2 Seismic Reflection Processing Sequence

In the seismic reflection method, reflected waves are the singular events that are of interest and significance for the purpose of generating a geological image of the subsurface. Raw seismic data could contain direct, refracted, surface, airwaves, and guided waves (that can all be referred to as noise in this circumstance) that are more often than not collected with the desired reflected waves during acquisition. Seismic reflection processing entails the analyses and corrections carried out on the raw field records to enhance the reflected events over the noise and the subsequent generation of a final structural image. The method of reflection seismic processing utilized in this thesis is the standard CMP method, described in detail by Yilmaz (2001).

Windows® based commercial Vista® seismic processing package of GEDCO, Calgary was employed in the processing of the seismic dataset. The implemented

seismic processing sequence, modified from Ogunsuyi and Schmitt (2010) is shown in Table 4.2 with the rationale behind some of the processing steps. Each step of the seismic processing flow is discussed in detail below.

4.2.2.1 Geometry

The raw field shot gathers were saved in SEG-2 format and loaded into Vista® software as a preprocessing step. Geometry assignment involves the allocation of coordinates (northing, easting, and elevation) to each trace in the dataset. This step is quite important in that the accuracy of subsequent stages of the seismic processing, like statics correction and CMP stacking are dependent on it. Proper geometry assignment is necessary to determine the relative location and elevation of each trace in all shot gathers and hence ensures accuracy during trace sorting. The geometries, as obtained from the differential GPS and LiDAR data, were saved in three ASCII files to facilitate loading onto the headers of the seismic traces: (1) shot station numbers with the associated coordinates; (2) receiver channel numbers with corresponding coordinates and; (3) field station numbers to connect the relative geometries of the shots and receivers. After loading the coordinates onto the seismic headers, the traces were sorted based on the shotpoint number and saved in the standard SEG-Y format for storage.

4.2.2.2 Trace Editing

Bad traces resulting from noisy channels and temporary equipment glitches could be dangerous to the rest of the seismic dataset. These noisy traces that could sometimes be revealed by abnormally high amplitude and frequency spikes could make some processing algorithm unstable and also create false events in the final processed image. It is therefore expedient to isolate and delete (or 'kill') these bad seismic traces. Accordingly, the noisy traces were identified by computing amplitude and frequency statistics of the seismic dataset and crossploting them respectively with the source receiver offsets; and thereafter deleting those with spurious amplitudes and frequencies. In addition, channels corresponding to

locations where geophones could not be planted, due to the intersection of the seismic profile line with a number of perpendicular roads, were also killed.

Some channels were also adversely affected by out-of-plane cultural (e.g., highway) noise during the seismic acquisition due to the proximity of the survey line to a major highway (Figure 4.3a). The trace editing in this instance was performed by carefully muting (i.e., zeroing) just the channels and the time intervals affected by the said noise in the unstacked raw shot gathers. Subsequently, the edited shot gathers were vertically stacked to enhance the seismic signals. A downside to this processing step is the occurrence of irregularly sampled spatial data gathers as an aftermath of dead/killed traces.

4.2.2.3 First-break Picking

First-breaks usually refers to the arrival times corresponding to the onset of recorded energy on shot or CMP gathers during seismic acquisition. The outset of seismic energy manifests as direct or refracted events that are often characterized by obvious kicks but could also be obscured by noise. Inversion of first-break traveltimes can be used to generate the velocity structure of the near-surface for statics correction and of deeper subsurface depths for depth migration or formation characterization based on their respective material velocities.

The success of the refraction-based method of statics computation and other inversion methods for generating the velocity field distribution of the subsurface is dependent on the picking procedure. The first-breaks on some of the recorded seismic shot gathers were masked by cultural and pre-signal noises; therefore the first-break picking was carried out manually to ensure accuracy.

Table 4.2. Processing sequence for the 2D seismic survey.

Processing Step	Justification
Geometry assignment	
Trace editing	Removal of bad traces
First-break picking	
Elevation/refraction statics corrections	Correction for lateral variations
Time- and offset-variant gain	Compensation for energy losses
Predictive deconvolution	Elimination of multiples
Spiking deconvolution	Compression of wavelet
Time-variant band-pass filtering	Suppression of low-frequency noise
Trace equalization	
CMP binning	
Initial velocity analyses	Determination of stacking velocities
NMO corrections	
Residual statics corrections	For near-surface velocity changes
Inverse NMO corrections	
Top muting	Removal of refracted waves
Radial domain processing	Removal of guided waves
Time power scaling & Spectral balancing	
Velocity analyses	Improvement of stacking velocities
NMO corrections	
Residual statics corrections	
Final velocity analyses	Improvement of stacking velocities
Final residual statics corrections	
NMO corrections	
Surgical muting	Removal of noise cone
CMP Stacking	
F-X prediction	Reduction of incoherent noise
2D finite-difference time migration	Place reflections in correct positions
Time-to-Depth conversion	Presentation of data in depth domain

4.2.2.4 Elevation/Refraction Statics Corrections

Reflection traveltime curve on a shot or CMP gather, theoretically demonstrated by a hyperbolic curvature (Steeples and Miller, 1990; Castle, 1994) may be distorted. Although these distortions could be as a result of deep structural complexities in the subsurface, they are mostly caused by near surface irregularities (Yilmaz, 2001). Near surface irregularities include changes in the elevation of the sources and receivers, and lateral variations in the thickness and velocity of the near-surface low-velocity layer generally described as the weathered layer. The departure from the ideal hyperbolic nature of the reflected traveltime curve can be rectified by time shifts, termed statics corrections, applied to the traces in a shot or CMP gather. Long-wavelength statics (i.e., more than a spread length) that could potentially degrade the reflections on the final CMP stack if left unresolved are normally accounted for by elevation and refraction statics computations and corrections.

Elevation statics corrections for positioning the data onto a common datum plane are performed on traces to account for the variations in the source and receiver elevations along the profile line. Selecting a correct average velocity that represents the material between the ground surface and datum is vital in carrying out an accurate elevation statics correction (Pelton, 2005). In general, a *replacement velocity*, usually considered to be the velocity of the first refractor is substituted as the material velocity of the depth interval between the base of the weathered layer and datum in order to adjust the traveltimes to the datum plane (Kearey et al., 2002). Such approximation may be acceptable for a situation in which the elevation variations between the sources and receivers are not significant, or the datum plane is placed below the land surface. However, in the case at hand, there is substantial elevation difference between the highest and lowest points in the land topography along the Peace River seismic profile line, and so placing the datum below the lowest elevation station will eliminate most of the shallow reflections that are of considerable interest in this study. Consequently, one is compelled to question the accuracy of the elevation statics

corrections for a profile having considerable land elevation variations with the flat datum placed at the highest point of the line if the velocity of the first refractor were chosen as the replacement velocity, as was implemented by Stucchi and Mazzotti (2009). However, the authors based the significance of using the first refractor velocity as replacement velocity on the increase in the continuity of the observed reflectors.

The near-surface low-velocity layer also contributes to the statics distortions experienced in shallow seismic data. Refraction statics corrections are used to account for the variable thickness and velocity of the weathered layer, mostly made up of unconsolidated materials. Knowledge of the model of the near-surface is required to compute the refraction statics corrections. Different refraction-based methods like the plus-minus method, generalized reciprocal method, and least-squares method can be employed to model the shallow subsurface for statics corrections as explained in Yilmaz (2001).

The first-break traveltimes were used to determine the model of the near-surface by plus-minus method (Hagedoorn, 1959). A single-layer refractor model with a weathering velocity of 500 m/s was assumed and the result (Figure 4.5a) shows the variable thickness of the weathered layer and lateral changes in the velocity of the refractor. The average velocity of the first refractor was ~ 1200 m/s and this was used as the replacement velocity for the elevation statics corrections. The statics corrections were computed with respect to a flat datum of 560 m a.s.l. elevation that is slightly above the highest point along the survey line. Total (sum of shot and receiver) refraction statics corrections ranged from about -40.6 ms to -6.6 ms whereas the total (shot and receiver) elevation statics shifts varied between +18 ms and +260 ms (Figure 4.5b). The gradual increase in the elevation statics shifts from west to east is due to the eastward-dipping nature of the surface topography along the profile line. Generally, statics corrections of high magnitudes are applied to a floating datum (i.e., a smoothed outline of the surface topography) first and then to a final flat datum in order to maintain the

hyperbolicity of reflection times in subsequent velocity analysis (Yilmaz, 2001). However, in our seismic dataset, the hyperbolic shape of the reflection traveltimes appears to be unaffected after skipping the step to position the shots and receivers to a floating datum; therefore the statics corrections were applied directly to the final datum. Nevertheless, for the purpose of accuracy in some processing steps, the elevation statics corrections were applied to the data after deconvolution and time-variant band-pass filtering.

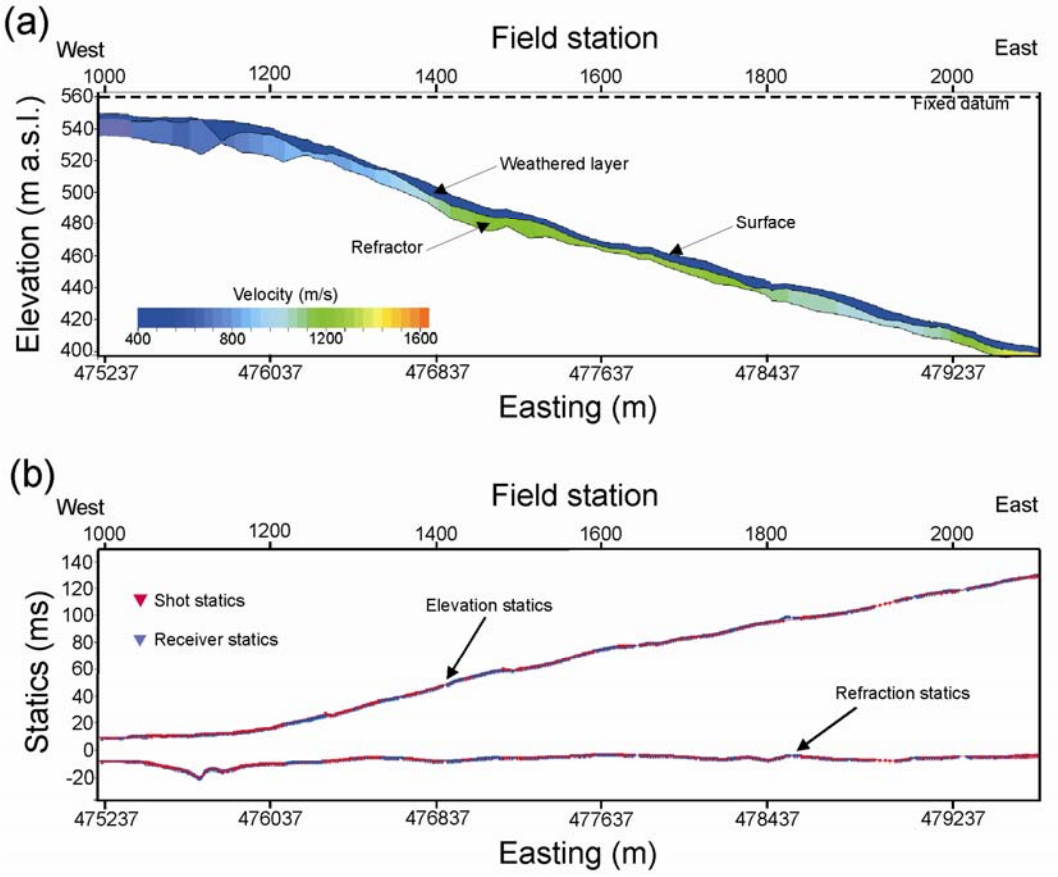

Figure 4.5. (a) One refractor model of the subsurface obtained by using plus-minus method to analyze the first-break traveltimes. Weathered layer velocity is 500 m/s while the average refractor velocity is 1200 m/s. (b) Computed elevation (top curve) and refraction (bottom curve) statics in ms for shots (red) and receivers (blue).

4.2.2.5 Compensation for Energy Losses

Seismic energy, propagating through a homogenous and isotropic body, is often dissipated by geometrical spreading and anelastic attenuation causing the seismic wave amplitudes to decrease with increasing time and distance. Geometric spreading is related to the spreading of energy due to the expansion of wavefronts and it is independent of frequency. Due to wavefront divergence, seismic body waves energy density decays by a proportion of $1/r^2$, and wave amplitude by $1/r$, with r being the radius of the wavefront (Lowrie, 1997; Kearey et al., 2002). On the other hand, anelastic attenuation is dependent on frequency and it is related to the interactions between the rock particles and/or pore fluids that cause loss of energy as a result of imperfect elasticity (e.g., anelasticity or viscoelasticity). These non-perfect elastic interactions convert part of the wave energy to frictional heat, with high frequencies attenuated preferentially above lower frequencies (Lowrie, 1997). Additionally, seismic energy can also be lost from scattering that is due to heterogeneities in the propagating medium. All three mechanisms are likely influential in the present study.

The energy loss due to geometrical spreading could mostly be revealed on shot records as a steady decay of seismic amplitudes at later traveltimes and farther offsets. It is therefore necessary to boost the diminished amplitudes by means of some type of gain function to counterbalance the energy losses. To achieve this, time- and offset-variant gain function was applied to each trace in the dataset. The gain function consists of control points, defined at 0 m and 800 m offsets with increasing energy decibel scaling values as traveltime and offset increase. It should be noted that such time- and offset-variant gain function defined is a simplistic approach to a complex problem; however, this technique fairly corrected for some seismic energy losses due to geometrical spreading. A better approach could be to generate a function based on the two-way traveltime and the root-mean-squared (rms) velocity of the primary reflections averaged over the

survey area (Yilmaz, 2001); however such scheme requires the knowledge of the subsurface velocity in the area.

A velocity-independent scaling function taking the form of exponential time power (i.e., t^{α}, where t is two-way traveltime and α is the time exponent) can also be used to correct for geometric spreading (Claerbout, 1985). This procedure was carried out after the removal of some of the guided waves (i.e., radial domain processing) so as to avoid boosting the amplitudes of the linear noise with the reflections. A value of 0.8 was used as the time exponent α in order to preserve the shallow reflection amplitudes relative to the deeper ones.

In order to compensate for frequency attenuation in the dataset, time-variant spectral whitening can be employed (Yilmaz, 2001). Time-variant spectral balancing involves splitting up each trace independently into different narrow band-pass ranges, applying a time-variant gain function (e.g., automatic gain control) to each band-pass component, and then summing up the results. The seismic traces were broken up into 10-Hz-width components with an automatic gain control (AGC) of 500 ms applied to each component before adding up the results. This procedure flattened the amplitude spectrum of the data within the analysis band and also boosted the higher frequencies that are more susceptible to absorption.

4.2.2.6 Deconvolution

Deconvolution can be used to compress the wavelet into a spike (i.e., broaden the frequency bandwidth) and attenuate multiples and reverberations, thereby increasing the vertical resolution of the seismic data. Assuming noise-free data, a recorded seismogram is a convolution of the earth's impulse response and basic seismic wavelet, with deconvolution process attempting to retrieve the earth's impulse response from the recorded seismogram. Deconvolution, however, requires some assumptions to be made in order to be effective as explained in Yilmaz (2001). One of the conditions required for obtaining a perfect result from

deconvolution is that the seismic wavelet has to be minimum phase, i.e., most of its energy is concentrated at its beginning. The seismic data being analyzed here is from a vibroseis source; thus the wavelet is an autocorrelated Klauder zero-phase (i.e., non-causal with peak amplitude at time zero) that violates the minimum phase requirement. However, despite the fact that the minimum-phase condition is breached for vibroseis data, spiking deconvolution without conversion of the zero-phase Klauder wavelet to its minimum phase correspondent appears to be successful for most field data (Yilmaz, 2001).

Applying a prediction filter to an input series results in the prediction of its value at a later time that corresponds to the prediction lag; this presents the prospect of estimating the periodic part (i.e., multiples or reverberations) of a reflection series. Predictive deconvolution works by applying a prediction filter to an input series to calculate its value at an advanced time; the estimation is then delayed by the prediction lag and subtracted from the initial input series to produce a multiple-free output series. Two passes of predictive deconvolution were applied to the data to attenuate multiples and reverberations. The first pass utilized an operator length of 40 ms and a prediction lag of 20 ms while the second was carried out with 70 ms operator length and 10 ms prediction distance. Comparing the initial shot gather (Figure 4.6a) with same record after predictive deconvolution (Figure 4.6b) shows the effectiveness of the procedure in suppressing multiples.

Spiking deconvolution was applied to the output of predictive deconvolution to collapse the basic wavelet into a spike. Spiking deconvolution is a particular case of predictive deconvolution with prediction lag set equal to one, thus producing a zero-lag spike output (Yilmaz, 2001). This procedure broadens the frequency content of the traces and increases the temporal resolution of the stacked data. After testing with different operator lengths for optimal results, 15 ms operator length was finally utilized (Figure 4.6c).

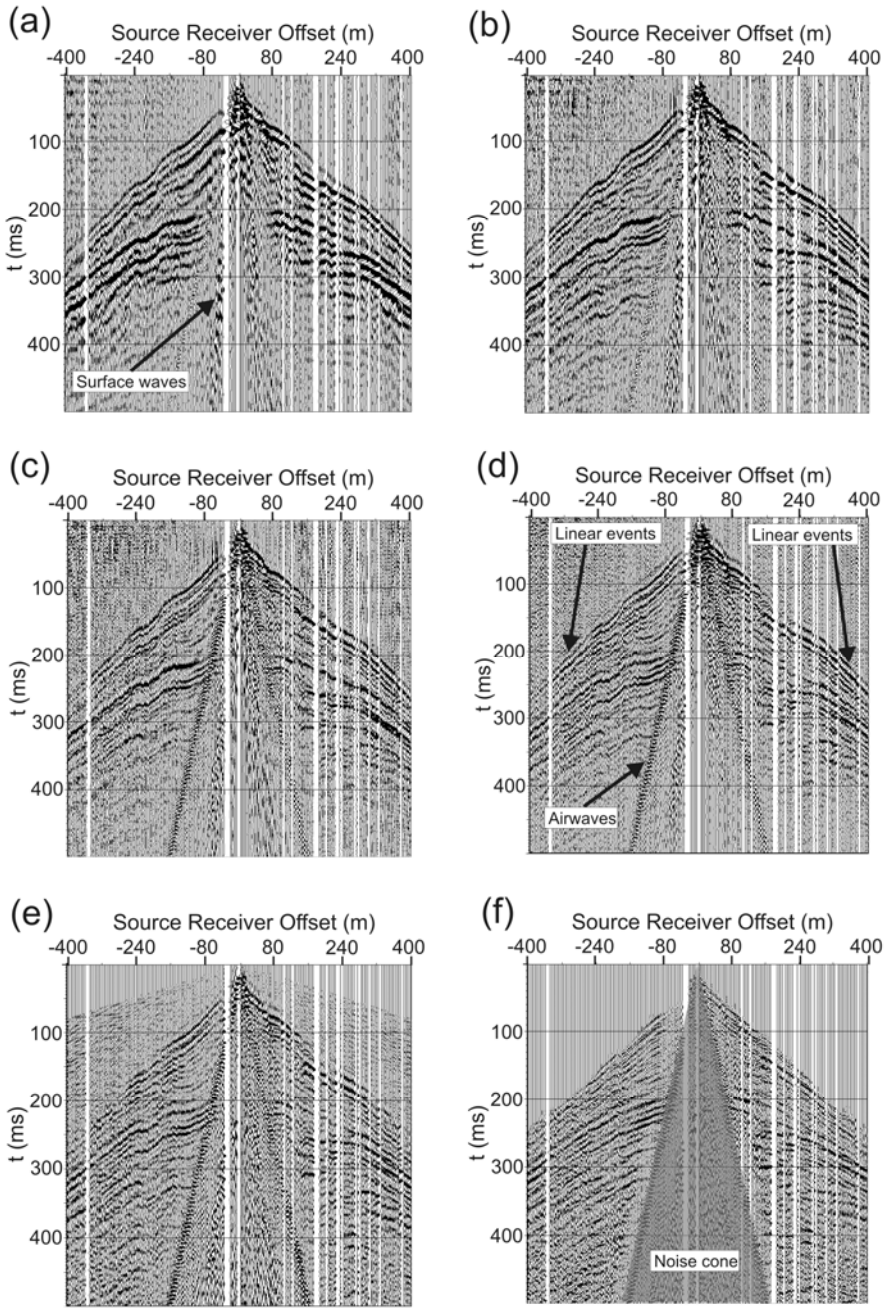

Figure 4.6. (a) A raw shot gather (shot 1360) after time- and offset-variant gain. (b) As for (a) after two passes of predictive deconvolution, demonstrating the suppression of multiples. (c) As for (b) after compressing the wavelet to a spike by means of spiking deconvolution. (d) As for (c) after time-variant band-pass filtering for suppression of low frequency surface waves. (e) As for (d) after radial domain processing for the suppression of linear events. (f) As for (e) after top mutes and residual statics corrections. The noise cone is highlighted in grey color.

Surface-consistent deconvolution is associated with the decomposition of the seismic trace into the deconvolutional effects of source, receiver, offset, and the earth's impulse response and the subsequent inverse filtering to recover the earth's response (Yilmaz, 2001). The assumption made is that the shape of the wavelet is surface-consistent, i.e., depends only on the source and receiver locations, and not on the wave path. Applying surface-consistent deconvolution did not appear to improve our data, and so the step was not included in the processing sequence.

4.2.2.7 Noise Suppression

Low frequencies in the amplitude spectrum of the seismic data are dominated by direct and surface waves. Frequency filtering in the form of a high-pass can be used to eliminate some of this undesirable noise. However, applying a low-cut frequency filter to the whole dataset may inadvertently remove some deeper reflections characterized by low frequencies too. Therefore, to avoid this, a time-variant band-pass filtering (60-250 Hz for 0-230 ms time interval and 45-180 Hz for 230-700 ms) was applied to the data. Additionally, some high-frequency ambient noise may be present in the data, thus the high-frequency side of the band-pass filter was not set to open. After the application of two passes of predictive deconvolution, spiking deconvolution, time-variant band-pass filtering and trace equalization, some of the noise has been suppressed (i.e., surface waves) and the reflections remarkably improved (Figure 4.6d). Nevertheless not all the noise has been eliminated and moreover, the guided waves concealed in the initial shot gather have been exposed.

Linear events (refracted and guided waves) that can adversely affect the interpretation of shallow seismic if they are not suppressed can still be observed. The first-break direct and refracted waves were successfully removed by top mute. On the other hand, mapping the data from the normal offset-time (x-t) domain into apparent velocity versus two-way time (radial or r-t) domain was utilized in the attempt to attenuate the coherent guided waves. The underlying

theory of this noise suppression process is that linear events in the *x-t* records transform into a relatively few radial traces with apparent frequencies shifting from the seismic band to sub-seismic frequencies (Henley, 1999). It follows that if a high-pass frequency filter is applied to the data in the radial coordinates, the linear waves can be eliminated to a certain extent. To this end, following transformation to *r-t* domain, a low-cut filter of 20 Hz was applied to the radial traces to eliminate the coherent noise mapped by *r-t* transform to low frequencies and the data was subsequently transformed back to *x-t* space (Figure 4.6e). A 20 Hz low-cut filter was chosen after a series of tests as a compromise between permitting a few linear events to remain in the data as an aftermath of using a lower-cut frequency filter as against removing some far offset reflections with a higher value of frequency filter. With consideration to the removal of some of the guided waves, the improvement of the new data over the old is obvious.

To further reduce the remnants of the source-generated noise (surface and guided waves) in the data, linear τ–p processing could be applied, where τ is intercept time and p is ray parameter (Spitzer et al., 2003). Linear and hyperbolic events in *x-t* domain are mapped into points and ellipses respectively in linear τ–p (or slant-slack) domain following linear τ–p transformation (Yilmaz, 2001). Hence, it is possible to isolate linear events from reflections in slant-slack gathers to facilitate noise suppression. However, aliasing of surface waves and airwaves could occur with the transform of irregularly spaced data (Marfurt et al., 1996) as observed in the Peace River seismic data probably due to significant amount of dead and killed traces in some gathers that produced irregular lateral live trace sampling. Also, improper incorporation of p values corresponding to dips absent in the data during τ–p mapping may produce noise in the reconstructed *x-t* data (Yilmaz, 2001). Moreover, spatially aliased events in the *x-t* domain may spread over a range of slowness including the pass region of the filter in the τ–p domain, therefore leaving some linear events in the data even after linear τ–p processing (Spitzer et al., 2001). Aliasing of surface waves and airwaves that introduced significant artifacts into the data were observed after performing τ–p processing

with various parameters. For this reason, linear τ–p processing was omitted from the processing sequence.

Events that are otherwise mapped to the same location in *x*-*t* domain may sometimes be separated and distinguished in frequency-wavenumber (*f*-*k*) coordinates. Reject zones in the form of polygons filters can be designed to zero out the areas where the undesirable events (e.g., coherent linear noise) are mapped to in *f*-*k* domain before transforming the data back to *x*-*t* space. Airwaves in this dataset were characterized by high frequencies; therefore making it extremely difficult to isolate them from the reflections in *f*-*k* space. Also, low frequency reflections were observed to be masked by surface waves in the *f*-*k* domain. In order to avoid muting the reflections in the process of removing the linear noise, *f*-*k* filtering was not performed on the data. As an alternative, surgical muting of the noise cone (Baker et al., 1998) was carried out on the data in order to eliminate the surface waves and airwaves (Figure 4.6f), thereby increasing the S/N ratio at the expense of any useful information that may lie within that zone.

4.2.2.8 CMP Binning

Raw seismic field records are acquired in shot-receiver mode, i.e., records are organized in such a way that each trace collected at all recording geophones are associated with their respective shotpoints. However, producing a suitable reflection profile image of the subsurface through seismic processing necessitates each trace to be positioned at the midpoint location between the respective source and receiver. Hence, all traces situated within a *common midpoint* area are grouped together in a procedure called CMP binning.

The choice of a CMP bin size is important in minimizing spatial aliasing during seismic data processing. The expected dip of structures is one of the most important criteria needed to be considered when choosing the best possible CMP trace interval (Spitzer et al., 2003). An optimum CMP bin size *b* can be determined by evaluating (Yilmaz, 2001)

$$b \le \frac{v_{\min}}{4 f_{\max} \sin\theta} \ , \qquad (4.4)$$

where v_{min} is the minimum velocity, f_{max} is the maximum frequency, and θ is the maximum expected dip of structures. The following parameter values were used for the dataset: a minimum velocity of ~1000 m/s for the shallowest sediments (averaged from the result of the seismic tomography – Section 4.3); maximum effective frequencies of ~ 240 Hz (from the shot gathers); and maximum expected dip of 20^0. The optimum CMP bin size was computed (Equation 4.4) with these parameters resulting in a value of 3 m.

4.2.2.9 Velocity Analyses and Normal Moveout (NMO)

As mentioned before, the reflection traveltime curve as a function of offset is hyperbolic in shape. Normal moveout (NMO) is the time difference between the two-way time at a given offset and the two-way time at zero offset. Before summing up the traces in a CMP gather, the reflection traveltimes are required to be NMO-corrected, i.e., the NMO at each offset trace must be subtracted from the traveltime so as to *flatten* the hyperbolic traveltime curve with the aim of properly aligning reflections for stacking. The NMO correction for a small-spread estimation (i.e., small offset compared to depth) Δt_{NMO} is given by (Yilmaz, 2001)

$$\Delta t_{NMO} = t - t_0 = t_0 \left[\sqrt{1 + \left(\frac{x}{v_{rms} t_0} \right)^2} - 1 \right] , \qquad (4.5)$$

where t is the two-way time at a given offset, t_0 is the two-way time at zero offset, x is the offset between the source and receiver positions, and v_{rms} is the rms velocity of the medium above the reflecting interface. Furthermore, the velocity that optimally renders the best fit of the traveltime curve on a CMP gather to a hyperbola is called the stacking velocity, which is derived from the rms velocity. The rms velocity v_{rms} down to the reflector is given by

$$v_{rms}^2 = \frac{1}{t_0} \sum_{i=1}^{N} v_i^2 \Delta t_i \ , \qquad (4.6)$$

where Δt_i is the vertical two-way time through the ith layer and v_i is the interval velocity of the ith layer. In general, the interval velocity and temporal thickness of each layer are not known, however the rms velocity, used to determine the stacking velocity can be estimated from the hyperbolic traveltime curves.

A technique that is commonly used to estimate rms velocities is the semblance method. Semblance is used to measure the energy of the coherency relating to reflections as obtained by means of hyperbolic searches of CMP gathers (Taner and Koehler, 1969). Semblance *S(k)* over a correlation window w centered at time k is given by

$$S(k) = \frac{\sum_{t=k-w/2}^{k+w/2} \left[\sum_{i=1}^{M} f_{i,t} \right]^2}{M \sum_{t=k-w/2}^{k+w/2} \sum_{i=1}^{M} \left[f_{i,t} \right]^2}, \qquad (4.7)$$

where $f_{i,t}$ is the amplitude value on the ith trace at two-way time t and M is the number of traces in the CMP gather. The method entails calculating semblance along stacking hyperbola associated with different trial stacking velocities at a given two-way zero-offset time t_0. The velocity corresponding to a maximal value of coherent energy is considered as the best estimate of the stacking velocity at that reflector.

Another technique often used to determine the stacking velocities is the constant velocity stack (CVS) method. The practice involves repetitively using a range of constant velocities to NMO-correct and then stack several CMP gathers (i.e., supergathers). The stacking velocity is then estimated on the basis of the amplitude and continuity of the stacked event by picking directly from the constant velocity stack panel.

After determining the stacking velocities, the CMP gathers are NMO-corrected prior to stacking. However, performing NMO correction on seismic gathers introduces a frequency distortion, especially for shallow events and at far offsets.

After NMO corrections, the dominant period of the waveform is stretched resulting in the lowering of the frequency in a phenomenon called NMO stretching. The stretching reduces the resolution of the data, particularly affecting the shallow events; and in the event that two or more reflection traveltimes hyperbolas intersects, the original reflectivity cannot be recovered (Buchholtz, 1972). A workaround to this problem is to automatically mute the stretched zones in the gather on the basis of the quantitative representation of the frequency distortion (Yilmaz, 2001) as defined by a percent stretch mute. The higher the stretch mute percentage, the greater is the amount of data in the CMP gather that is included in the stack.

In order to convert the picked rms velocities to interval velocities, Dix's formula (Dix, 1955) is used:

$$v_{\text{int}} = \sqrt{\frac{v_n^2 t_n - v_{n-1}^2 t_{n-1}}{t_n - t_{n-1}}} \ , \qquad (4.8)$$

where v_n and v_{n-1} are the rms velocities at layer boundaries n and n-1 respectively; and t_n and t_{n-1} are the two-way time at these layer boundaries. The interval velocity is the actual material velocity of the medium.

The velocity analyses were performed on CMP supergathers composed of 11 adjacent composite CMPs, by creating a panel of offset sort/stack records, constant velocity stacks, and semblance output. The stacking velocities estimation was refined in an iterative manner (Table 4.2) to ensure accuracy. On some CMP supergathers, the velocities were difficult to pick with confidence because of the discontinuous nature of some reflections probably emanating from within the landslide body. Further, velocity picking difficulties due to low fold coverage were likewise encountered. The final stacking velocities from the CMP velocity analyses (Figure 4.7a) and the corresponding interval velocities after conversion using Equation 4.8 (Figure 4.7b) show the lateral variations in the velocities along the profile line. After NMO, a relative large stretch mute of 70% (determined from testing with different values) was applied to the data before stacking.

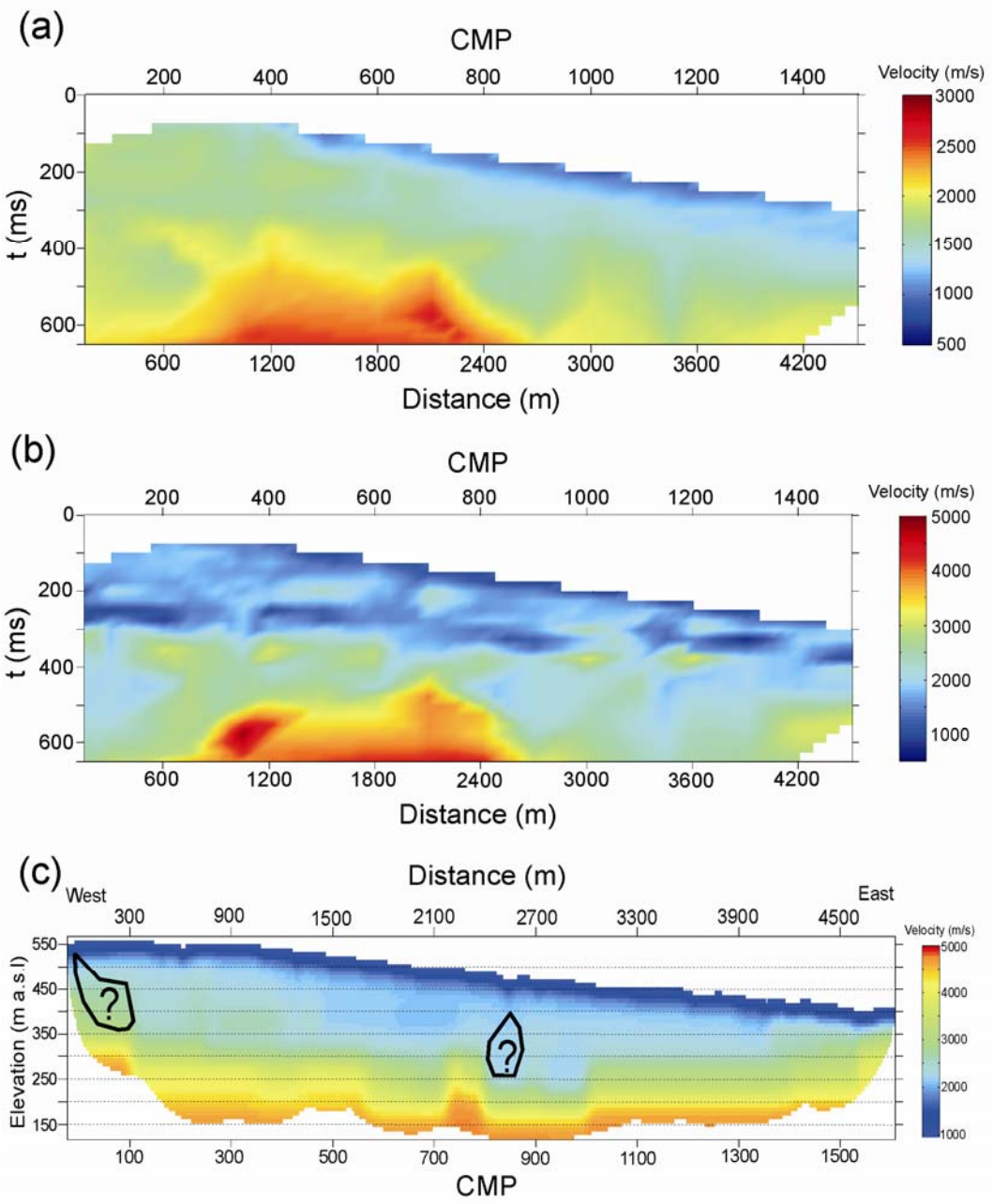

Figure 4.7. (a) Final stacking velocities picked on CMP supergathers. (b) As for (a) after conversion to interval velocities by using Dix's equation. (c) The possible interval velocities of the subsurface as obtained from the traveltime inversion. The polygons labeled with question marks in (c) are areas with no hit count obtained from Figure 4.9. The horizontal axes are CMP and distance along profile from origin (i.e., 475006 m easting, equivalent to CMP 0). Vertical axis for (a) and (b) is two-way time in ms while that for (c) is elevation in m a.s.l.

4.2.2.10 Residual Statics Corrections

Residual statics corrections are required to correct for short wavelength variation in the shallow velocity underneath each sources and receivers. If the corrections were not made, stacked section could be degraded resulting in losses in reflections continuities. In calculating residual statics, a basic assumption made is that the statics shifts are surface-consistent, i.e., associated with a constant time delay that depends on the source and receiver locations on the surface and not on the wave path (Taner et al., 1974). This supposition is valid for the case where a low velocity layer overlies a higher velocity bed, thus causing the raypaths to be vertical within the low velocity layer.

Surface consistent residual statics estimation by a stack power maximization algorithm (Ronen and Claerbout, 1985) based on minimizing the difference between the modeled and real traveltime deviations associated with reflections on NMO-corrected gathers (Yilmaz, 2001) was utilized in this study. The algorithm, always applied to NMO-corrected data, involves creating 2 supertraces – one from the traces of the common-shot or common-receiver record under consideration in sequence, and the second from all the traces of the associated part of the stack, also in sequence, without the contribution of the traces from that common-shot or common-receiver gather – and crosscorrelating them. The correlation lag corresponding to the maximum crosscorrelation value is deemed the residual static shift of that shot or receiver gather, depending on the gather under consideration. This process is carried out for all shot and receiver stations iteratively to converge on a solution of shot and residual statics time shifts.

Residual statics corrections are normally carried out iteratively in conjunction with the conventional velocity analyses and NMO corrections for the removal of the short wavelength distortions observed on the hyperbolic traveltime trends. Thus, after each round of velocity analyses (Table 4.2), surface consistent residual statics by means of stack power maximization algorithm (Ronen and Claerbout, 1985) was calculated from the NMO-corrected data and the estimated corrections

applied to the data. Residual statics time shifts ranging from about -8 ms to +8 ms were obtained during the 3 cycles of the computations. It is observed that the distortions in the hyperbolic curvature of the reflection traveltimes for a shot gather after 3 passes of residual statics corrections has been reduced considerably (Figure 4.6f) in comparison to the original record (Figure 4.6e).

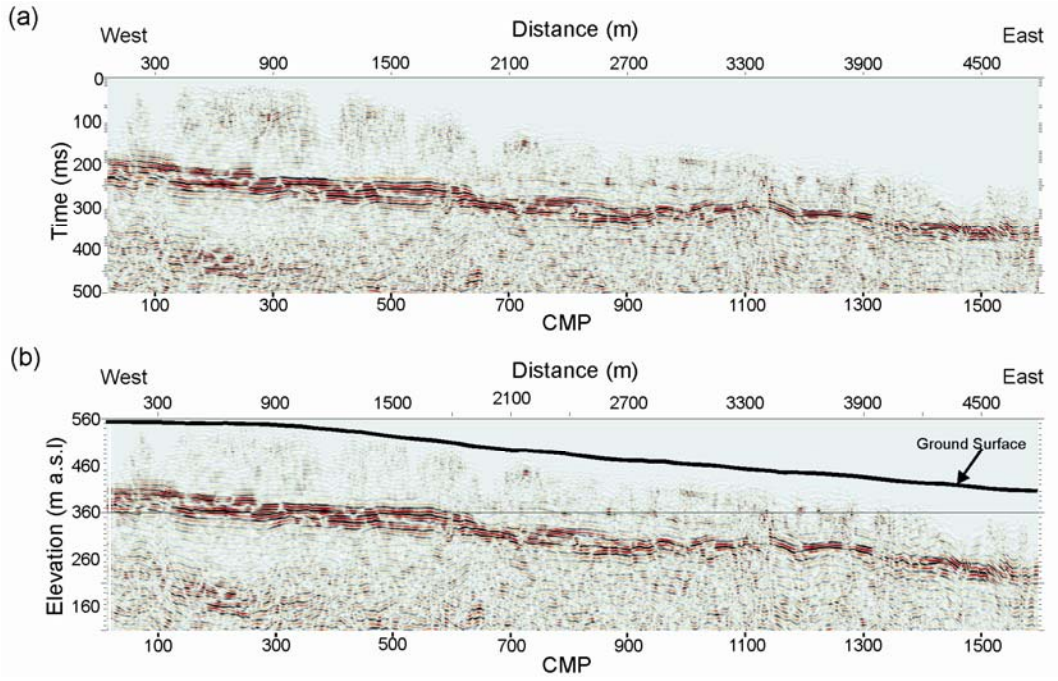

Figure 4.8. (a) Poststack time-migrated seismic section with two-way traveltime in ms as vertical axis. (b) Corresponding final depth converted seismic profile with vertical axis as elevation in m a.s.l. The horizontal axes for the images are CMP and distance along profile from origin (i.e., 475006 m easting, equivalent to CMP 0).

4.2.2.11 CMP Stacking and Poststack Processing

The stacking velocities estimated from the final velocity analyses were used to perform NMO corrections on the CMP gathers. Thereafter, the traces in each CMP gather were summed in a process called CMP stacking. In addition, *f-x* prediction was performed on the data to reduce incoherent noise in the seismic

data (Canales, 1984). This prediction, in the *f-x* domain, works by creating a model for the signal via the summation of complex exponentials of the spatial variable *x* and then estimating a least-squares approximation of the predictable part of the signal for each particular frequency *f* by the use of Wiener filter theory. The data in *f-x* domain is then transformed back to *t-x* coordinates to generate an enhanced image.

Migration collapses diffractions and moves dipping reflections to their true positions, thus increasing the lateral resolution of the seismic data (Yilmaz, 2001). Black et al. (1994) developed a flow chart on whether migration of an arbitrary shallow reflection profile is worthwhile. Based on the migration test, 2D poststack finite-difference time migration was performed on the reflection data to create a representative image of the subsurface (Figure 4.8a).

For the purpose of correlating the seismic data with actual depth values, the seismic data was converted from time to depth by using the average velocities (flattened to ground elevation) from the typical CMP velocity analyses. The time-to-depth conversion procedure entails, first, interpolating the input velocity function (i.e., final stacking velocities obtained from traditional CMP velocity analyses, in the case for this study) for every CMP in the dataset. Second, the velocity functions at each CMP are averaged (i.e., smoothed), and third, a suitable conversion table that will associate the time input samples to the corresponding depth output samples is built from the velocity functions. The conversion table is subsequently used to transform the dataset from time-sampled to depth-sampled (Figure 4.8b).

4.3 Seismic Refraction Tomography

Seismic refraction tomography is aimed at providing a representative seismic wave velocity distribution of the subsurface through the inversion of first arrival

traveltimes from multiple sources and receivers. It should be noted that seismic tomography generation is not limited to using first arrival traveltimes as input only, but some algorithms utilize both refracted and reflected traveltimes (e.g., Zelt and Smith, 1992). Regardless, the interpretation of the generated model follows the reasoning that it is possible to delineate the various geological formations in the subsurface on the basis of the material velocities presented by the tomography. The tomography generated for this study makes use of only the first arrival traveltimes, i.e., direct and refracted events.

The data obtained during seismic reflection acquisition normally contains both refracted and reflected waves; hence, there is no need to collect additional dataset. Furthermore, the seismic acquisition cable length determines the maximum depth of investigation that will be observed on the refraction tomography results, i.e., longer spread length is associated with deeper depths. Accordingly, the far offset shots recorded during the data acquisition are valuable in illuminating deep targets in the study area.

Linearized traveltime inversion techniques require the use of a starting/initial model that represents the probable velocity structure of the area as input into the scheme (e.g., White, 1989; Bergman et al., 2006; Zelt et al., 2006) in order to determine the final model by iteratively minimizing the difference between the observed and calculated traveltimes. Consequently, the resulting seismic tomography is often prejudiced by the initial model used (Van der Hilst and Spakman, 1989; Kissling et al., 1994). It is therefore important to collate and incorporate all the applicable information about the area in the construction of an appropriate starting velocity model. Although in this study there is some available information about the geology of the research area, however the seismic velocity responses of the various geological units are not known because of insufficient wellbore information. Utilizing a poor starting velocity model that is not representative of the area may introduce some undesirable bias into the resulting model causing the inversion to converge to an inaccurate solution.

To this end, a nonlinear optimization technique (Pullammanappallil and Louie, 1994) that does not necessitate supplying a starting model was employed for the inversion of the first arrivals in this study as against the method of Zelt and Smith (1992). The initial model used in the method is determined arbitrarily by the algorithm to avoid any bias in the final model. The initial model independency of the method was demonstrated by the authors and its performance compared against a linearized inversion scheme. The algorithm has been used to provide useful information about landslides (e.g., Narwold and Owen, 2002).

4.3.1 Inversion Algorithm

The algorithm involves the inversion of the first arrival traveltimes based on a nonlinear optimization technique called generalized simulated annealing (Pullammanappallil and Louie, 1994). The model is parameterized into numerous blocks, all having the same size, with dimensions chosen in accordance to the preferred resolution. A low resolution model has bigger cell sizes compared to a higher resolution model. A fast finite-difference scheme based on a solution to the eikonal equation (Vidale, 1988) that accounts for all types of primary arrivals and turning rays is applied for computing the traveltimes through models without ray tracing. The implementation of the algorithm, from Pullammanappallil and Louie (1994), is detailed below:

(1) Compute traveltimes through an initial velocity model as well as the least-square error E_0. For any iteration i, the least-square error E_i is given by

$$E_i = \frac{1}{n}\left(\sum_{j=1}^{n} \left(t_j^{obs} - t_j^{cal} \right)^2 \right), \qquad (4.9)$$

where n is the number of observations, j signifies each observation, and t^{obs} and t^{cal} are the observed and calculated travel times respectively.

(2) Perturb the model by adding random constant-velocity boxes, followed by smoothing so as to prevent enforcing any unwarranted precision on the model. The added boxes can be any velocity between two fixed values chosen by the user

and of any aspect ratio and size. Thereafter, calculate the least-square error E_1 for this new model.

(3) The new model is unconditionally accepted if its error is less than that of the previous model (i.e., $E_1 \leq E_0$); and when $E_1 > E_0$, it is provisionally accepted with the probability:

$$P_c = \exp\left(\frac{(E_{\min} - E_1)^q \, \Delta E}{T}\right), \tag{4.10}$$

where $\Delta E = E_0 - E_1$, T is the *temperature*, q is an empirical parameter, and $E_{\min}$ is the value of the least-square error at the global minimum (ideally equal to zero). Accepting models with a larger least-square error provisionally prevents being trapped in local minima in the search for the global minimum. As the inversion approaches the global minimum, the likelihood of accepting an unfavorable step toward local minimum tends to zero by reason of the factor $(E_{\min} - E_1)^q$.

(4) Repeat steps (2) to (4) until the inversion converges based on a specified criterion. The convergence condition requires the difference in the least-square error between consecutive models and the chance of accepting new models having greater error to be very small.

The convergence of simulated annealing is controlled by the rate of *cooling*, i.e., the variation of T with iteration (Pullammanappallil and Louie, 1994 and references contained); namely, the higher the temperature T, the greater is the likelihood of accepting models with negative ΔE, and vice versa. A cooling scheme to allow the algorithm to jump out of local minimum early on in the inversion, and still converge to the global minimum solution towards the end of the procedure needs to be designed. The process employed to do this is to compute several short runs of the algorithm for various fixed temperature values and then determine the critical temperature T_c from the mean least-square error for each run. During the actual inversion scheme, the optimization is started at a high constant temperature T, so as to remove any bias from the initial model. The value of T is reduced by a factor of 10 i.e., $T/10$ after every 1000 iterations until the critical temperature T_c is realized. This encourages better convergence by

allowing the system to reach a representative thermal equilibrium. Thereafter, the rate at which the value of *T* is reduced is cut by a factor of two after every 10000 iterations to allow the inversion to converge to the global minimum (Pullammanappallil and Louie, 1994).

The simulated annealing provides a suite of final models with comparable least-square error, enabling the choice of a model that best represents the geology of the area. The optimization algorithm was incorporated into SeisOpt® Pro™ software (provided by Optim Software and Data Solutions, USA) and this was used to carry out the inversion of first arrival times in this study.

4.3.2 Inversion Implementation

The implementation of the optimization algorithm requires a large number of iterations (50000 or more) that is computer-intensive. Consequently, the computer clusters at the processing center of Optim Software and Data Solutions (USA) was utilized to generate the seismic refraction tomography for this study.

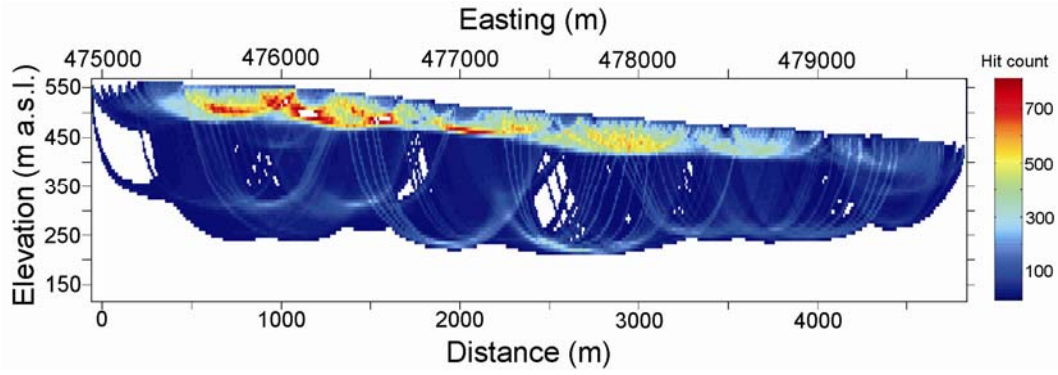

Figure 4.9. Hit counts showing ray coverage after the inversion implementation. The vertical axis is elevation above sea level (a.s.l) in m while the horizontal axis is easting in UTM co-ordinates and distance along profile from origin (i.e., 475006 m easting, equivalent to CMP 0).

The size of the blocks to which the model is parameterized determines the resolution of the model. The dimension of the cells must be chosen such that it is small enough to resolve small features and sufficiently large to allow satisfactory ray sampling, i.e., non-zero hit counts in each block.

The Vista® processing package (GEDCO, Calgary) was used to pick 39554 first arrival traveltimes on 181 shot gathers and then exported as a text file. Matlab® was used to format the file into the 3 files required by SeisOpt® Pro™, i.e., shots, receivers, and picks files. The final model was ~ 4.9 km long and ~ 0.4 km at the deepest section. The grid size of 8.9 x 8.9 m was chosen bringing the total number of blocks in the final model to 19865. After the inversion, a least-square error of 0.001 s^2 between the observed and calculated traveltimes was realized for the tomographic results (Figure 4.7c). This error value is considered a reasonable fit for the optimization results. In addition, the ray coverage was observed to be very comprehensive with a number of comparatively small areas having zero hit count (Figure 4.9). The areas with no ray passage are questionable and so less confidence is placed on the tomographic results at those locations.

4.4 Vertical Seismic Profiling

A zero-offset and four sets of walkaway vertical seismic profiling (VSP) surveys were conducted in the PR08-03 wellbore located at the Town of Peace River (Figures 3.1 and 3.2) in November 2009. The zero-offset VSP was conducted to first, understand the acoustic reflectivity signature of the various formations near the borehole in order to correlate with the surface seismic reflection data; second, ascertain the one-way traveltime to various subsurface depths for the purpose of establishing a time-to-depth relation; and third, to determine the interval velocities of the rocks in the wellbore. The latter reason is able to provide information in lieu of the sonic log. Three of the walkaway VSP surveys, oriented in west-east direction, were carried out to generate a structural image of the subsurface in the

vicinity of the borehole while the fourth, oriented in north-south direction, was conducted to provide a measure of anisotropy in the area. The quality of the results from the VSP surveys was not as good as anticipated, thus defeating to a certain extent, some of the purpose of the survey. Nevertheless, some useful information about the area was garnered from the VSP survey. The acquisition and processing of the VSP data are discussed in this section of the thesis.

4.4.1 Data Acquisition

The zero-offset VSP data was acquired in a dry steel-cased geotechnical well (PR08-03). Although the total depth of the borehole was ~ 125.6 m, we could only conduct the VSP to a maximum depth of 101.85 m because the hole was plugged at that depth. The data was collected bottom-up because of ease of acquisition. A spatial depth sampling of 0.5 m was used for the data acquisition from the plugged bottom of the wellbore to ~ 97 m depth before switching to a spacing of 1 m because of time and logistical constraints.

The University of Alberta's IVI Minivib™ unit was utilized as the source with linear sweeps of 7 s from 15 Hz to 250 Hz at a force of about 22240 Newtons (5000 pounds). Moreover, instead of employing the P-wave seismic mode as energy source, we chose to experiment with S-wave energy source type, with the objective that we can recover both P- and S-wave data from the procedure. The shear wave was generated by re-orienting the vibrator mass horizontally as opposed to vertically during P-wave generation. Accordingly, we collected data in two 'polarizations' designated 0^0 for vibrator mass facing north, and 180^0 for south-facing mass. Although, care was taken to ensure that the orientations of the vibrator mass were exactly at 180^0 to each other for the different polarizations, however we cannot validate that this was always the case. Generally, about 5 – 8 shots were conducted for each sampling depth and vibrator mass orientation.

The receiver was a wireline 3-component geophone tool with electrically operated retractable pivot arm (manufactured by SIE Pty, Australia). The tool consists of 2 horizontal geophones and one vertical 14-Hz geophone in orthogonal configuration. The wall-locking device integrated with the tool ensures the firm clamping of the geophones to the wall of the wellbore in order to provide good coupling. The recording equipment was a semi-distributed seismograph Geode™ (manufactured by Geometrics Ltd., San Jose, CA). The acquired zero-offset VSP data was sampled at 0.5 ms with a record length of 1.19 s from 101.85 m to 5.85 m depth below the ground. Cross-correlation of the seismic traces with the sweep pilot signal was not carried out in the field so as to preserve the raw records that were saved in SEG-2 format.

The four walkaway VSP surveys were conducted with the same seismic S-wave energy source, geophone tool, recording system, and acquisition parameters (i.e., record time sampling rate and length) as the zero-offset data. The three walkaway surveys in west-east direction have vibrator mass orientation as the zero-offset VSP while the fourth survey in north-south direction has vibrator device facing west for 0^0 polarization and east for 180^0. The downhole receiver was positioned at 30, 60, and 99 m depths for the west-east vertical profiles and 99 m depth for the north-south survey. The west-east profiles spanned 146 m (with farthest offsets at 48 m to the west and 98 m to the east of the wellhead) at 5 m shot spacing, while the north-south profile was about 45 m long with nearest and farthest offsets at 53 m and 98 m to the south of the wellbore respectively, also carried out at 5 m shot spacing. Due to ATCO high-pressured gas pipelines in the survey area, we could not discharge shots at the wellhead's southern near offsets.

In general, the coupling of the vibrator plate to the ground was good during the VSP surveys as indicated by the uniformity of the force level observed over each sweep. However, traffic, random and pre-signal noises proved to be problematic in the acquired data, especially in the walkaway surveys. After the zero-offset data acquisition, the correlated traces collected during the walkaway VSP surveys

on the vertical component of the geophone showed substantial noise increase (Figures 4.10a and 4.10b), possibly attributable to newly-developed electrical defect within the tool. Similarly, harmonic noise became apparent on the correlated traces recorded in the course of the walkaway data acquisition on all the receiver components (e.g., Figure 4.10b). On the whole, the data had a very low S/N ratio; hence specifically tailored processing steps are required in an attempt to obtain useful information from it.

4.4.2 Data Processing

The first step in the processing sequence of the VSP data was to assign geometry to the seismic traces in Vista® seismic processing package; after which the traces were sorted into the two vibrator mass orientations, i.e., 0^0 and 180^0. It was observed that the pilot traces from the energy source were clipped along the amplitude axis from the beginning of the signals to ~ 5000 ms and entirely uncharacteristic of vibroseis linear sweeps from 0 to ~ 200 ms (Figure 4.11a). The reason for the abnormal nature of the pilot traces is unknown; moreover utilizing the traces without further processing may produce undesirable results. For the reason that seismic source signals may not always be exactly repeatable in real-life data acquisition ventures due to the excitation of the near surface beyond its elastic limits (Aritman, 2001), a single synthetic vibroseis sweep trace was considered inappropriate for crosscorrelation with the raw traces. The clipped parts of the signals were observed to be characterized by superimposed frequencies that were higher than the predominant frequencies at those particular times in the vibroseis linear sweeps (Figure 4.11a). Following, a time-variant band-pass filter proved valuable in correcting the anomalous features on the pilot traces (Figure 4.11b). The time-variant band-pass filter applied was 16 – 19 Hz for 0 to 100 ms; 15 – 60 Hz for 50 to 1000 ms; 15 – 80 Hz for 800 to 2000 ms; 15 – 130 Hz for 1800 to 3500 ms; 15 – 180 Hz for 3300 to 5000ms; and 15 – 230 Hz for 4800 to 8192 ms. The raw traces were subsequently crosscorrelated with the

refined pilot traces and the resulting traces from the same receiver depths stacked for enhanced S/N ratio.

Although a horizontal force seismic source, as was used in this research, creates wavefield that is dominated by S-wave energy, the data recorded by the vertical receivers in areas with flat and horizontal stratigraphic beds are expected to be dominated by downgoing and upgoing P-wave modes for a zero-offset VSP configuration (Hardage, 2000). Furthermore, S-waves are expected to dominate the data recorded by the horizontal geophones. Hence, making the assumption that the stratigraphic layers near the borehole are flat and horizontal, the vertical-component data can be processed as a standard P-wave-source zero-offset VSP data to provide information about the seismic reflectivities of the various formations.

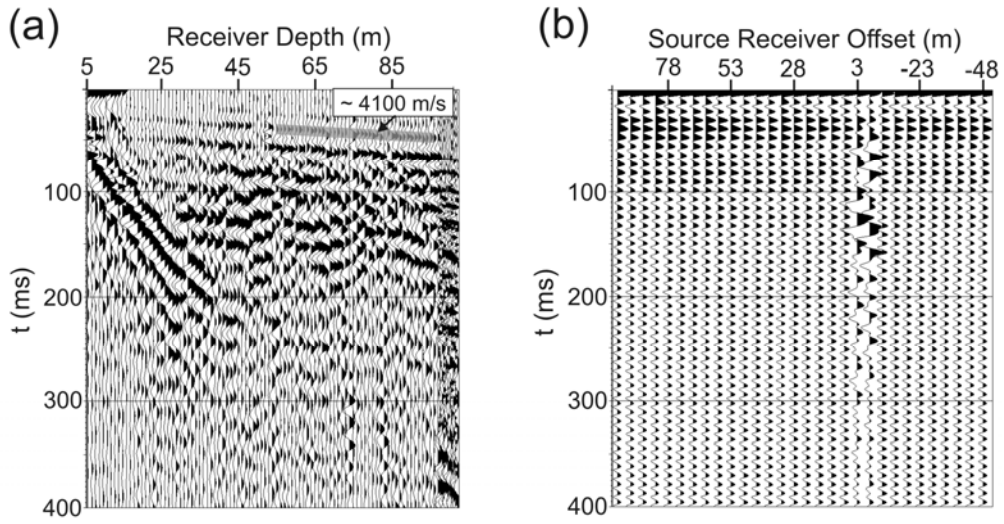

Figure 4.10. Vertical component of correlated 0^0 polarization vsp data for (a) zero-offset and (b) walkaway data with positive source receiver offsets to the west of the well head and negative offsets to the east. Also shown on (a) is the apparent velocity of a segment of the first break picks (grey highlight) as obtained from a simple intercept-time refraction method. The walkaway data is noisy due to a possible defect in the downhole receiver tool subsequent to the zero-offset data acquisition.

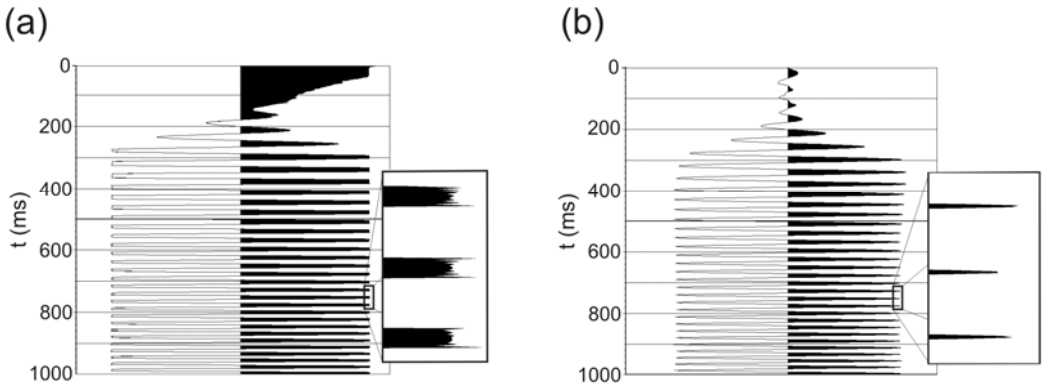

Figure 4.11. (a) A typical raw pilot trace from the vsp data acquisition. (b) As for (a) after time-variant band-pass filtering. It is obvious from the zoomed-in area (rectangular boxes) that the pilot data has been improved.

The next step in the processing sequence was the separation of the data into horizontal (X and Y) and vertical (Z) components. First arrivals were then picked on the Z components of both 0^0 and 180^0 vibrator mass orientations. Interval velocities, as well as traveltime-depth relationship (i.e., checkshot) can be derived from the first break picks. A preliminary analysis of the first break picks showed P-wave velocities of over 4500 m/s at depths of about 90 m in glacial sediments (e.g., Figure 4.10a). The P-wave velocities in the vicinity of the borehole for depths shallower than 100 m were expected to be less than 2300 m/s as revealed by the results of the seismic tomographic inversion. The high interval velocities observed in the VSP data could possibly be due to waves travelling through the wellbore steel casing and the formation. Thus, to process the zero-offset data effectively, the arrivals through the steel casing are required to be eliminated.

A variety of wavefield separation techniques to separate downgoing signals from the upgoing events have been used in VSP data processing. Some common separation methods include *f-k* velocity filtering (Embree et al., 1963), median filtering (Stewart, 1985), and τ–p filtering method (Hu and McMechan, 1987). In τ–p filtering method, restricting the range of p (slowness) values to the desired τ–p quadrant and applying a filter during the forward transform can enhance the

separation results to a great extent (Moon et al., 1986). Thus, the downgoing events with opposite dips to the upgoing wavefield can be separated by limiting the permitted p values. It also follows that diverse dips in the downgoing wavefield can be separated based on the range of slowness values allowed. Consequently, and based on the large difference in the P-wave velocity through steel (> 5000 m/s) and that through the glacial deposits in this study (< 2300 m/s), an attempt was made to separate the arrivals through the steel casing from that through the formation by restricting the range of p values during the forward τ–p transformation. To the best of my knowledge, I have not been able to find in near surface VSP literature anywhere such process has been adopted to separate waves travelling through steel casing and the geologic formation. Hence, this procedure may require closer attention to better understand its effectiveness.

In order to isolate the downgoing P-wave through the formation from the VSP vertical component data, a limited range of p values from 0.5 to 2.0 ms/m (i.e., 500 to 2000 m/s) was allowed during the forward τ–p transform for both 0^0 and 180^0 polarized data. After inverse τ–p transformation, the P-wave first arrivals were re-picked separately on the different band-passed filtered (i.e., 20/35 to 235/250 Hz) 0^0 (Figure 4.12a) and 180^0 (Figure 4.12b) VSP records. For each VSP polarization data, the traveltimes of the earliest coherent amplitude peak of each trace were picked manually. The amplitude peak was selected as the first-breaks because it allows for better accuracy in the picking, thus providing for better estimation of the desired relative times between different depths that are used in the determination of the interval velocities, as against absolute traveltimes at each depth. From the separate graphs of the picked first-breaks as a function of depth (i.e., plots of traveltimes) for the 0^0 (Figure 4.12e) and 180^0 (Figure 4.12f) data, the associated P-wave interval velocities in the wellbore were determined by least squares fitting of a line to 5 congruous time points and calculating the local tangent slope of the traveltime curve (e.g., Schmitt et al., 2007). The interval velocities obtained from the data after τ–p filtering are comparative with the results of the tomographic inversion, thus signifying the prospect of the method.

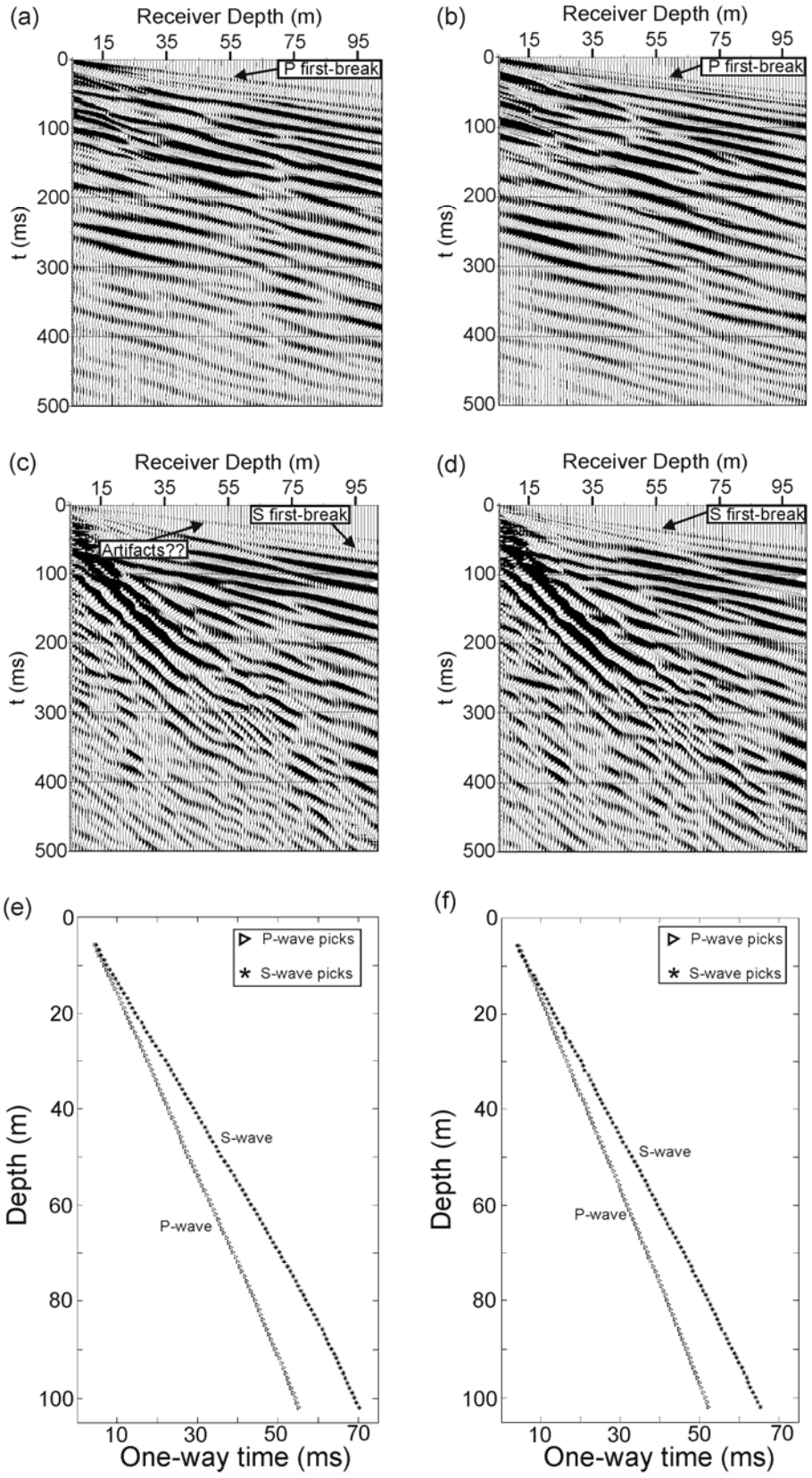

Figure 4.12. Figure caption on next page.

Figure 4.12. (a) Downgoing wavefield from vertical component of zero-offset 0^0 polarization vsp obtained from τ–p filtering. (b) Downgoing wavefield from vertical component of zero-offset 180^0 polarization vsp obtained from τ–p filtering. (c) Downgoing wavefield from a horizontal component of zero-offset 0^0 polarization vsp obtained from τ–p filtering. A possible artifact is shown on the record. (d) Downgoing wavefield from a horizontal component of zero-offset 180^0 polarization vsp obtained from τ–p filtering. (e) Plot of P- and S-wave first-break traveltimes against receiver depth for 0^0 polarization vsp data obtained from (a) and (c). (f) Plot of P- and S-wave first-break traveltimes against receiver depth for 180^0 polarization vsp data obtained from (b) and (d).

For the isolation of downgoing S-wave through the formation on a VSP horizontal (X) component for both 0^0 and 180^0 polarized data, the allowable slowness values were limited to 0.5 – 5.0 ms/m (i.e., 200 to 2000 m/s) range (Figures 4.12c and 4.12d). Just one of the resulting VSP horizontal components was utilized to determine the S-wave interval velocities, because performing a hodogram analysis on the X and Y components data appears not to have effect on the results. Similar to the P-wave first-breaks picking on the vertical component, the first coherent amplitude peak on the VSP X component data was manually picked as the S-wave first arrivals for the band-passed filtered (i.e., 20/35 to 235/250 Hz) 180^0 polarization data (Figure 4.12d). However, the first coherent amplitude peak on the 0^0 polarization X component VSP record were not picked as the first arrivals because they appear too fast and could be possibly associated with τ–p transformation artifacts, thus the second coherent amplitude peak was selected as the first-breaks (Figure 4.12c). After picking the first breaks on the new horizontal records, the S-wave interval velocities in the wellbore were determined using the same method employed for obtaining the P-wave velocities from the different plot of S-wave traveltimes for 0^0 (Figure 4.12e) and 180^0 (Figure 4.12f) VSP records.

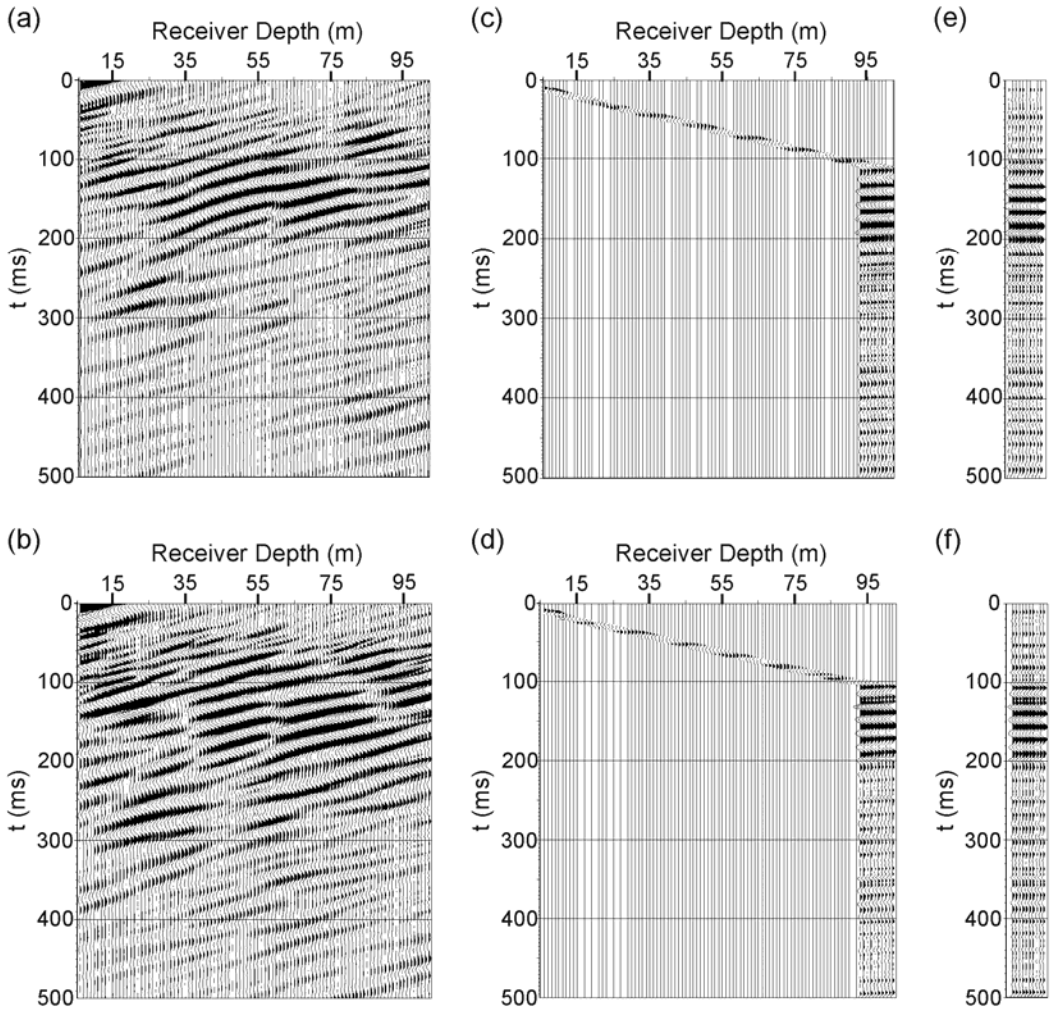

Figure 4.13. (a) Upgoing wavefield from vertical component of zero-offset 0^0 polarization vsp obtained from τ–p filtering. (b) Upgoing wavefield from vertical component of zero-offset 180^0 polarization vsp obtained from τ–p filtering. (c) As for (a) after exponential gain, normal moveout correction, reverse flattening on the first break picks, band-pass filtering, and corridor muting. (d) As for (b) after exponential gain, normal moveout correction, reverse flattening on the first break picks, band-pass filtering, and corridor muting. (e) As for (c) after stacking. (f) As for (d) after stacking.

The upgoing reflections from zero-offset VSP data are required to generate the acoustic reflectivities near the borehole for the purpose of conducting a tie with the seismic reflection data. The upgoing reflections on the vertical component of the 0^0 (Figure 4.13a) and 180^0 (Figure 4.13b) polarized data were obtained by using τ–p filtering wavefield separation technique. The range of p values allowed for isolating the upgoing wavefield was -1.0 to -0.4 ms/m. VSP deconvolution, normally performed to improve the vertical resolution of the resulting image was deemed unnecessary for this dataset because there appears to be no improvement to the data after experimenting with it.

Energy losses through absorption and transmission were accounted for in the upgoing wavefield by applying an exponential gain to the traces, i.e., each time sample t is multiplied by e^{nt}, where n is the exponential constant. A value of 1.25 was utilized as n for both 0^0 and 180^0 VSP polarized datasets. Subsequently, a normal moveout correction was applied using the velocities from the first break picks (Figures 4.12e and 4.12f). In order to place the data in two-way time, a reverse flattening on the first break picks was carried out. Such time statics shift vertically aligns the upgoing reflections prior to stacking (Hardage, 2000). A band-pass filter of 40/60 to 230/250 Hz was later applied to the data in order to increase the vertical resolution of the final image.

Restricted vertical summation (also called corridor stacking) may be adopted in eliminating some noise caused by early downgoing and upgoing multiples that may be present in the VSP composited trace (Hardage, 2000). Hence, data within 10 ms corridor width of the first break pick from top of the wellbore to 92 m depth in addition to all traces below 92 m (Figures 4.13c and 4.13d) were stacked to produce the final P-wave reflectivity signature of the various formations near the wellbore for both 0^0 (Figure 4.13e) and 180^0 (Figure 4.13f) polarizations. Due to the considerable elevation variation in the study area, the resulting VSP images are required to be static corrected with a replacement velocity of 1200 m/s (as was

used during the reflection data processing) in order to tie properly with the surface seismic reflection data.

Considering the processing sequence performed for the VSP datasets, it is important to point out that these results are considered to be speculative, subject to further analysis to determine the accuracy of the τ–p filtering method used to separate the waves travelling through the steel casing and that through the geologic formations in the vicinity of the wellbore.

4.5 Summary

Beginning with an overview of basic seismic concepts, the seismic methodology utilized in the study of the Peace River landslide was discussed in this chapter. The acquisition and processing of the reflection seismic data that is used to create a structural image of the subsurface from the reflections emanating from various geologic units was later described. The technicalities and difficulties related to the acquisition and customized processing of the reflection dataset was adequately explained. In addition, the inversion algorithm employed for the generation of a tomographic velocity distribution of the subsurface using the associated refraction data of the seismic dataset was discussed. The seismic tomography was intended for the delineation of the various geological formations in the subsurface on the basis of the material velocities. Also discussed in this chapter of the thesis is the acquisition and unconventional processing of the vertical seismic profiling (VSP) dataset. The unconventional processing method involve the correction of the anomalous features on the field vibroseis pilot traces, and the separation of the desired waves travelling through the geologic formations in the vicinity of the wellbore from that propagating through the wellbore steel casing. Although the quality of the VSP data was not as good as anticipated, the processing was helpful in providing some useful information from the datasets.

Chapter 5

Electrical Resistivity Tomography Methodology

In this chapter, the electrical resistivity tomography (ERT) methodology used for the landslide investigation will be described. Electrical resistivity concepts relevant to the application of the geophysical technique will first be treated. The ERT data acquisition efforts carried out at the Town of Peace River and the corresponding inversion algorithm and results will later be discussed. The chapter will also explain an ERT data modeling procedure carried out to determine the resistivity measurements that will be made over a specified resistivity model to assist in the subsequent interpretations of the ERT results.

5.1 Electrical Resistivity Method Overview

Electrical resistivity is a measure of the resistance of a volume of material to the flow of electric current. Electrical resistivity (or geoelectrical) surveys are used to determine the resistivity distribution of the subsurface. This is commonly carried out by utilizing a variety of electrode array configurations to introduce electric currents into the ground by means of a pair of conductors and then measure the ensuing potential differences between another pair of receiver electrodes. A different mode of conducting resistivity surveys is by inducing currents into the earth through time-varying magnetic fields with coils that are not in contact with the ground. Geoelectrical methods are broadly used for subsurface investigations with applications in groundwater, environmental, geologic, and engineering studies (e.g., Worthington, 1977; Dahlin et al., 2002; Chambers et al., 2006).

At shallow depths, electric current flow is influenced by three major mechanisms, i.e., ionic, electronic, and surface conduction (see Knight and Endres, 2005). As described by the authors, ionic conduction refers to the movement of charged ions due to an applied electric field while electronic conduction involves the movement of electrons. Surface conduction is related to the excess charge in the double layer at the solid-fluid interface, prevalent in materials with large surface areas (e.g., high clay contents). Thus, the resistivity (reciprocal of conductivity) of a given rock is controlled by a combination of its various material properties, and it can span over a range of values for a particular rock type. At near-surface depths in most environmental and engineering studies, the resistivity is primarily influenced by the porosity, fluid resistivity, and the amount of clay in the rocks (Zonge et al., 2005).

The practicality of the electrical resistivity method was established on the pioneering work of the Schlumberger brothers in the early 1920's (see Daily and Owen, 1991), evolving from wireline logging in boreholes through surface-based vertical electric sounding surveys to electrical resistivity tomography (ERT). A typical vertical electric sounding method entails the measurement of the apparent resistivity of a single location as a function of depth by systematically increasing the spacing of the survey's electrode array centered on that particular location (Parker, 1984), resulting in a one-dimensional resistivity model of the subsurface. A different type of survey arrangement is the profiling technique that involves fixing the spacing of the electrodes and moving the whole array along a profile line to simply provide lateral resistivity information.

ERT surveys, on the other hand, provide two- or three-dimensional resistivity information about the earth, i.e., laterally and vertically. ERT is a technique that estimates the electrical resistivity distribution of the subsurface from a large number of resistance measurements from conductors arranged in an arbitrary geometric design (Daily et al., 2005). The geometry patterns adopted during ERT data acquisition could include placing electrode arrays on the ground surface, in

boreholes, or a combination of both, depending on the objective of the survey. ERT is a blend of conventional electrical investigation and the inversion methods of tomography, thereby creating a high resolution resistivity representation of the plane containing the electrode arrays.

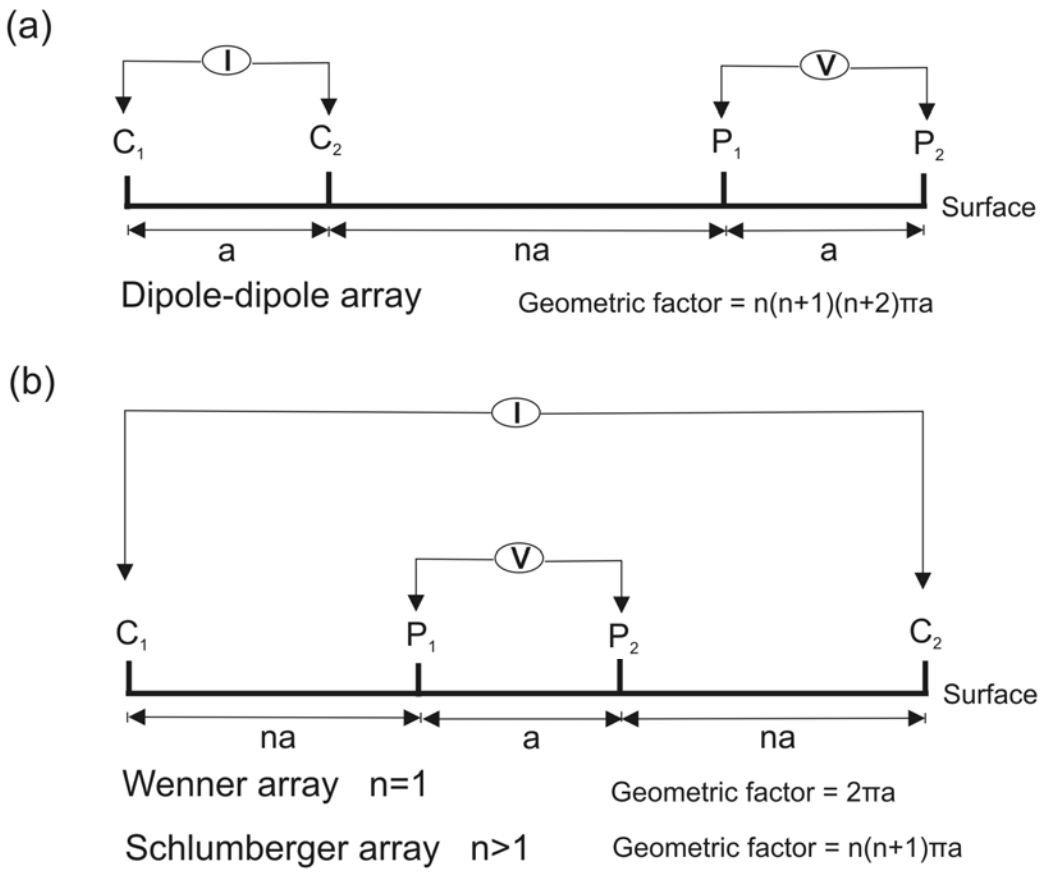

Figure 5.1. Common arrays in resistivity surveys with their various geometric factors. The electrode array consists of a pair of conductors that supplies electric current into the earth, i.e., C_1 and C_2, and another pair that measures the potential difference, i.e., P_1 and P_2. (a) Dipole-dipole array. (b) Wenner and Schlumberger arrays.

There are numerous electrode arrays that could be employed during resistivity surveys, tailored for specific targets; the common ones being dipole-dipole, Wenner, and Schlumberger arrays (Figure 5.1). Readers are referred to Loke (2010) for a description of the relative sensitivities and advantages of each array type. Apparent resistivities are calculated from the injected electric currents, measured potential differences, and the applicable geometric factor of the array (Figure 5.1). In order to display the measured apparent resistivity data for a 2-D survey, the data point under consideration is typically placed horizontally at the midpoint of the set of electrodes used to carry out that measurement and vertically at a location that is proportional to the spacing between the electrodes. These resistivities are not true resistivities because they are a function of the volume of earth beneath the electrodes and the array geometry, hence the word *apparent* (Zonge et al., 2005). The possible actual resistivities are estimated by means of modeling and inversion procedures.

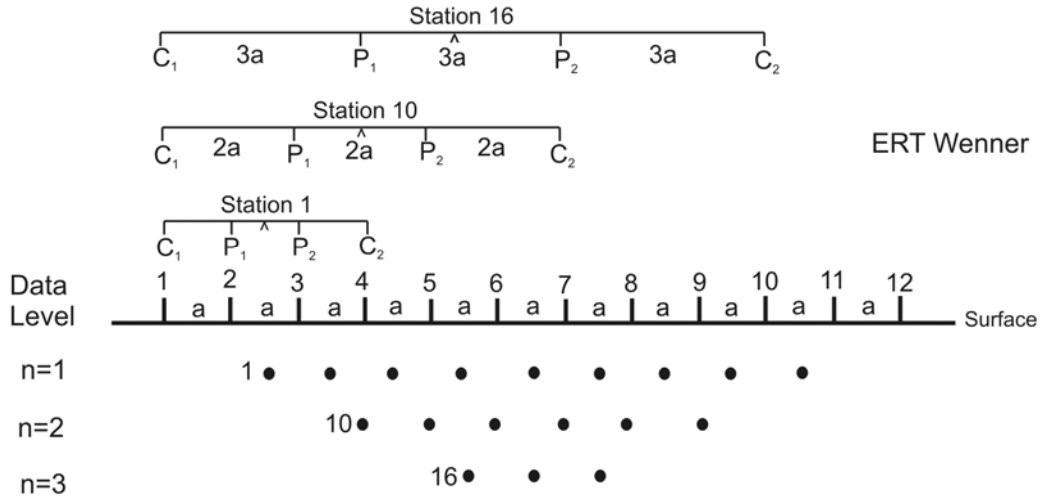

Figure 5.2. ERT data acquisition sequence with Wenner array configuration. The electrode array consists of a pair of conductors C_1 and C_2 that supplies electric current and another pair P_1 and P_2 that measures the ensuing potential difference.

ERT data acquisitions are typically performed with numerous electrodes in some preferred array geometry, e.g., Wenner, Schlumberger, dipole-dipole array, etc. The choice of array is dependent on the depth and structure being investigated, sensitivity of the array to vertical and lateral changes in subsurface resistivity, horizontal data coverage, and signal strength (Loke, 2010). In Wenner array configuration for 2D surface-based ERT acquisition, the electrodes, connected to a multi-core cable are placed at equal spacing on the ground. With the aid of an electronic switching device, four electrodes are automatically selected during each measurement to inject current into the ground and measure the resulting potential difference based on Wenner array pattern (Figure 5.2). The apparent resistivity is thus recorded for many such measurements over the entire spread length of the array. In order to extend the investigation line beyond one spread length, the array of electrodes is laterally shifted along the profile line and all the measured data is combined. The apparent resistivity data are then inverted using an appropriate algorithm to generate a possible true resistivity distribution of the survey area subsurface. For more information about ERT imaging techniques, readers are referred to Daily et al. (2005).

5.2 ERT Data Acquisition

Three sets of ERT data were collected parallel to Highway 2, inside the southern ditch of the highway, within the Alberta Transportation right-of-way on the west side of the Town of Peace River in June 2009. The combined ERT lines covered the whole extent of the seismic profile line and extended beyond it in both west and northeast directions (Figures 3.1 and 3.2). The ERT survey was carried out commercially with WorleyParsons Ltd's equipments and personnel from the University of Alberta, Alberta Geological Survey, and WorleyParsons Ltd. The ERT survey was conducted to image the Cretaceous bedrock and the Quaternary sediments in order to delineate the Peace River landsliding and also provide

information about the associated processes on the basis of the contrasts in the subsurface resistivities.

Wenner array was used for the data acquisition with parameters shown in Table 5.1. ERT Line 1 was a combination of two profile lines acquired with an electrode spacing of 22.5 m. The first part of the line, trending from west to east, was ~ 4.9 km in length and it has the same origin in the west-east direction as the seismic line; whereas the second segment, lying to the east of the first part and also overlapping it by about 450 m, has a total length of ~ 1.8 km. The large electrode spacing associated with the survey allows for a deeper depth of investigation; however it is at the expense of reduction in resolution. ERT Line 2 was also acquired in west-east direction, but with an electrode spacing of 10 m spanning a total profile length of ~ 4.6 km. Its origin is about 500 m to the east of the seismic line's origin. The highest resolution ERT data collected was ERT Line 3. The line has an electrode spacing of 5 m and it covers a total length of ~ 400 m in the west-east direction. ERT Line 3 was located closer to the Peace River bank and its origin was about 5 km to the east of the seismic line's starting point.

Table 5.1. Acquisition parameters for the ERT survey.

Parameter	**ERT Line 1**	**ERT Line 2**	**ERT Line 3**
Electrode spacing (m)	22.5	10	5
Length of profile (km)	~ 6.2	~ 4.6	~ 0.4
Depth of investigation (m)	~ 300	~ 150	~ 75
Number of electrodes	280	461	80
Number of data points	1882	3099	389
Array type	Wenner		
Equipments	Controller: ABEM Terrameter SAS 1000 Multi-electrode system: ABEM Lund (ES464 switching box and multi-conductor cables)		
Electrode length	30 cm		

The ERT data was acquired with an ABEM Terrameter SAS 1000 and an ABEM Lund (electrode selector ES464 with multi-conductor cables) system connected to a 12 V DC battery. To avoid ground disturbances, 30-cm long electrodes were utilized. It should be noted, however, that electrodes could not be planted on the surface of the few roads that intersected the ERT profile lines. At sites with dry surfaces, good electrical coupling between the electrodes and ground that is critical during resistivity data acquisition may be difficult to realize (Hauck et al., 2003) leading to current leakage. This problem was not encountered at our survey location because of the wetness of the ground from rain showers.

In order to avoid errors in the ERT data measurements and the reconstructed true resistivity image, the locations of the electrodes need to be accurately determined (Oldenborger et al., 2005). To this end, almost every electrode position was surveyed with the University of Alberta's Trimble Differential Global Positioning System (GPS) and specified in Universal Transverse Mercator (UTM) zone 11 North coordinate system based on North American Datum of 1983 (NAD83) to give an easting, northing, and elevation value. For higher level of accuracy in the elevation values, the GPS data was validated against the high resolution LiDAR data.

5.3 ERT Data Inversion

The inversion algorithm employed for the ERT data was a nonlinear smoothness-constrained least-squares inversion method (Loke and Barker, 1996) applied in a commercial software called RES2DINV by Geotomo Software, Malaysia (Loke, 2010). The objective of the ERT data inversion is to produce a possible resistivity distribution of the subsurface (i.e., a model) that offers a response (i.e., forward modeling) that agrees with the observed apparent resistivities (i.e., data) according to certain criteria. The model is parameterized into cells, with the

model parameters being the resistivity value of each block. The model response, i.e., the calculated apparent resistivity values are derived from the model parameters by finite-difference or finite-element methods.

Since the inversion problem is a nonlinear one, an initial model is required. In the implementation of the ERT inversion algorithm, a homogenous earth model is assumed as the starting model. For a set of observed data and model response (i.e., calculated data) represented by vectors **y** and **f** respectively, the discrepancy vector **g** is given by

$$\mathbf{g} = \mathbf{y} - \mathbf{f} \,. \tag{5.1}$$

Similarly, the model parameters can be represented by a vector **q** with *n* elements. The optimization method seeks to minimize the least-square error *E* given by,

$$E = \mathbf{g}'\mathbf{g} = \sum_{i=1}^{n} g_i^2 \tag{5.2}$$

where g_i and **g'** are the elements and transpose of vector **g** respectively. In order to minimize the error *E*, Gauss-Newton equation

$$\mathbf{J}'\mathbf{J}\Delta\mathbf{q} = \mathbf{J}'\mathbf{g} \tag{5.3}$$

is used to determine the necessary changes in the model parameters (Loke, 2010 and references contained). **J** is the Jacobian matrix containing elements $\partial f_i/\partial q_j$, i.e., the change in the *i*th model response due to a change in the *j*th model parameter, **J'** is the transpose of matrix **J**, and $\Delta\mathbf{q}$ is the model parameter change vector. Equation 5.3 is solved iteratively by calculating the parameter change vector and updating the model parameters with the changes.

In order to minimize the spatial variations in the model parameters, thus producing a smoothness-constrained least-squares solution, and also to avoid the problem of singularity that may occur in **J'J** matrix product, the Gauss-Newton equation is modified to (Loke, 2010 and references contained)

$$(\mathbf{J}'\mathbf{J} + \lambda\mathbf{F})\Delta\mathbf{q}_k = \mathbf{J}'\mathbf{g} - \lambda\mathbf{F}\mathbf{q}_k \,, \tag{5.4}$$

where λ is the damping factor, k is the iteration number, and **F** is the smoothness constrain matrix given by $\mathbf{F} = \alpha_x \mathbf{C'}_x \mathbf{C}_x + \alpha_y \mathbf{C'}_y \mathbf{C}_y + \alpha_z \mathbf{C'}_z \mathbf{C}_z$. Smoothing matrices in the x-, y-, and z-axis are $\mathbf{C}_x$, $\mathbf{C}_y$, and $\mathbf{C}_z$ respectively, with α_x, α_y, and α_z being the relative weights given to the respective filters.

Table 5.2. Inversion parameters and results for the ERT datasets.

Inversion Parameters			
Inversion algorithm	Smoothness-constrained least-squares (l_2-norm)		
Optimization method	Standard Gauss-Newton		
Jacobian matrix calculation	Recalculated for the first 4 iterations; Quasi-Newton approximation used for subsequent ones		
Model discretization	Blocks with equal widths; increasing thickness as depth increases. Number of model parameters allowed to exceed data points		
Forward model method	Finite-element		
Topographic modeling	Finite-element mesh with damping		
Damping factor	Damping factor of 0.3 for first iteration; calculated automatically for subsequent iterations		
Vertical/horizontal flatness filter ratio	0.001		
Results			
	ERT Line1	ERT Line 2	ERT Line3
No. of data points after editing	1704	3021	385
Number of model blocks	3552	6088	766
Number of iterations	6	6	5
Final RMS error (%)	6.7	8.15	3.3

The ERT inverse problem is ill-posed and non-unique (Daily et al., 2005), resulting in more than one model producing same response that fits the measured data. Thus, the accuracy of the selected final result depends considerably on the constraints applied during the inversion procedure. If the constraints are representative of the actual situation, then the result will be comparable to the true subsurface resistivity distribution. Additionally, topographic effects can conceal important features in the apparent resistivity data, therefore making topographic modeling key to accurate results in areas with significant elevation variations (Zonge et al., 2005). Consequently, topographic modeling was incorporated into the inversion scheme (Loke, 2010).

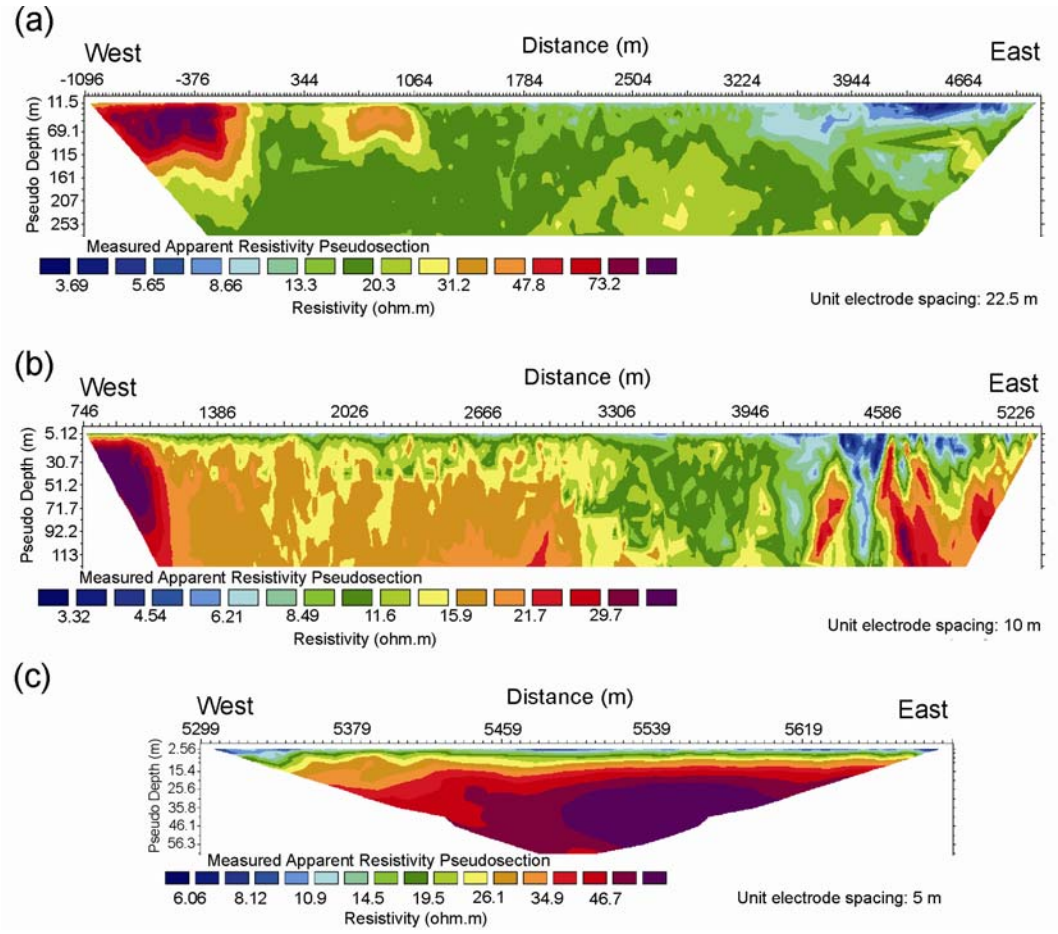

Figure 5.3. Measured apparent resistivities for (a) ERT Line 1 at 22.5 m electrode spacing, (b) ERT Line 2 at 10 m spacing, and (c) ERT Line 3 at 5 m spacing. The

horizontal axis is distance from the start of the seismic profile line (i.e., 475006 m easting in UTM Zone 11N coordinate system) in m and the vertical axis is pseudo depth in m. Note that only ERT Lines 1 and 2 overlap while Line 3 is to their east.

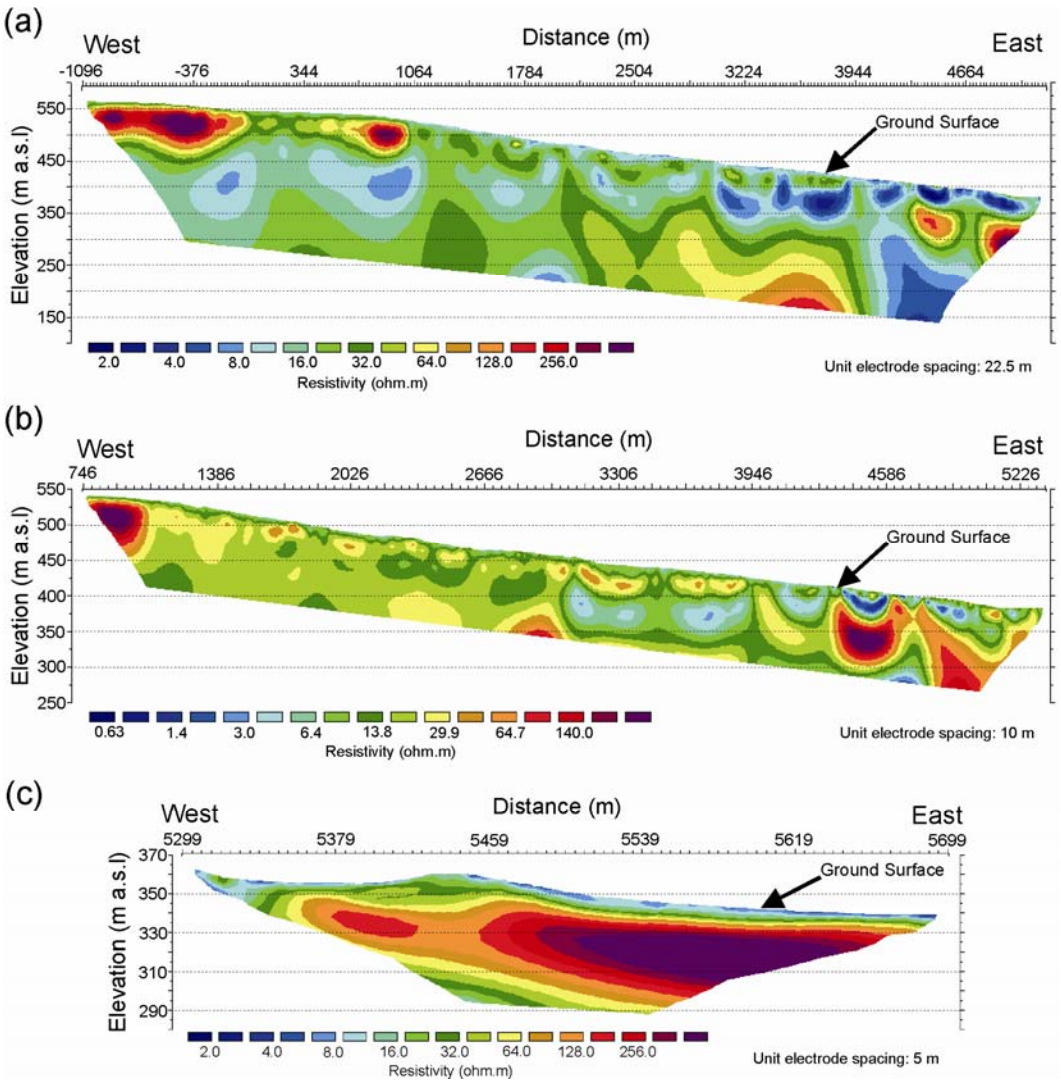

Figure 5.4. Results of the ERT data inversion for (a) ERT Line 1 at 22.5 m electrode spacing, (b) ERT Line 2 at 10 m spacing, and (c) ERT Line 3 at 5 m spacing. The horizontal axis is distance from the start of the seismic profile line (i.e., 475006 m easting in UTM Zone 11N coordinate system) in m and the vertical axis is elevation in m a.s.l.

Before carrying out the inversion procedure, the data for the three ERT lines were examined on a profile plot so as to identify systematic noise that could be problematic to a final image. The systematic noise could be identified as unusually low or high values and they were eliminated from the data as a pre-inversion step. The inversion parameters for the three ERT lines were selected after careful testing for best possible results (Table 5.2). After inversion, the final RMS error for each ERT line was not more than 8.15 % (Table 5.2), signifying a good fit between the observed apparent resistivities (Figure 5.3) and the inversion results (Figure 5.4) model responses.

5.4 ERT Data Modeling

The ERT forward modeling procedure is used to compute the apparent resistivities that will be measured over a specified resistivity model. It can be utilized in the designing phase of a survey or used to determine the consequent resistivity response over a given geological structure. Finite-difference and finite-element methods are mostly employed in engineering and environmental surveys to compute resistivity responses due to their inherent advantage of being able to handle arbitrary resistivity distribution of the subsurface, parameterized into thousands of cells with diverse resistivity values (Loke, 2010).

It was observed in the resistivity log of PR08-03 wellbore that there exists a high electrical resistivity (> 200 ohm-m) sandy formation at ~ 328 m a.s.l. elevation with thickness of about 10 m (Figure 3.7). The sandy unit lies on top of a thin layer of Shaftesbury shale formation that is expected to have low resistivities due to its high clay content and depositional history in marine environment. In turn, the Shaftesbury Formation overlies the Peace River Formation sandstones (i.e., Paddy and Cadotte members) that are likely to be characterized by higher resistivities. However, it is uncertain whether or not the ERT survey would be able to clearly image the top of the thin conductive Shaftesbury Formation that is

sandwiched between two highly resistive sand units. Hence, to resolve this uncertainty, a forward modeling procedure was carried out over a presupposed model of the subsurface.

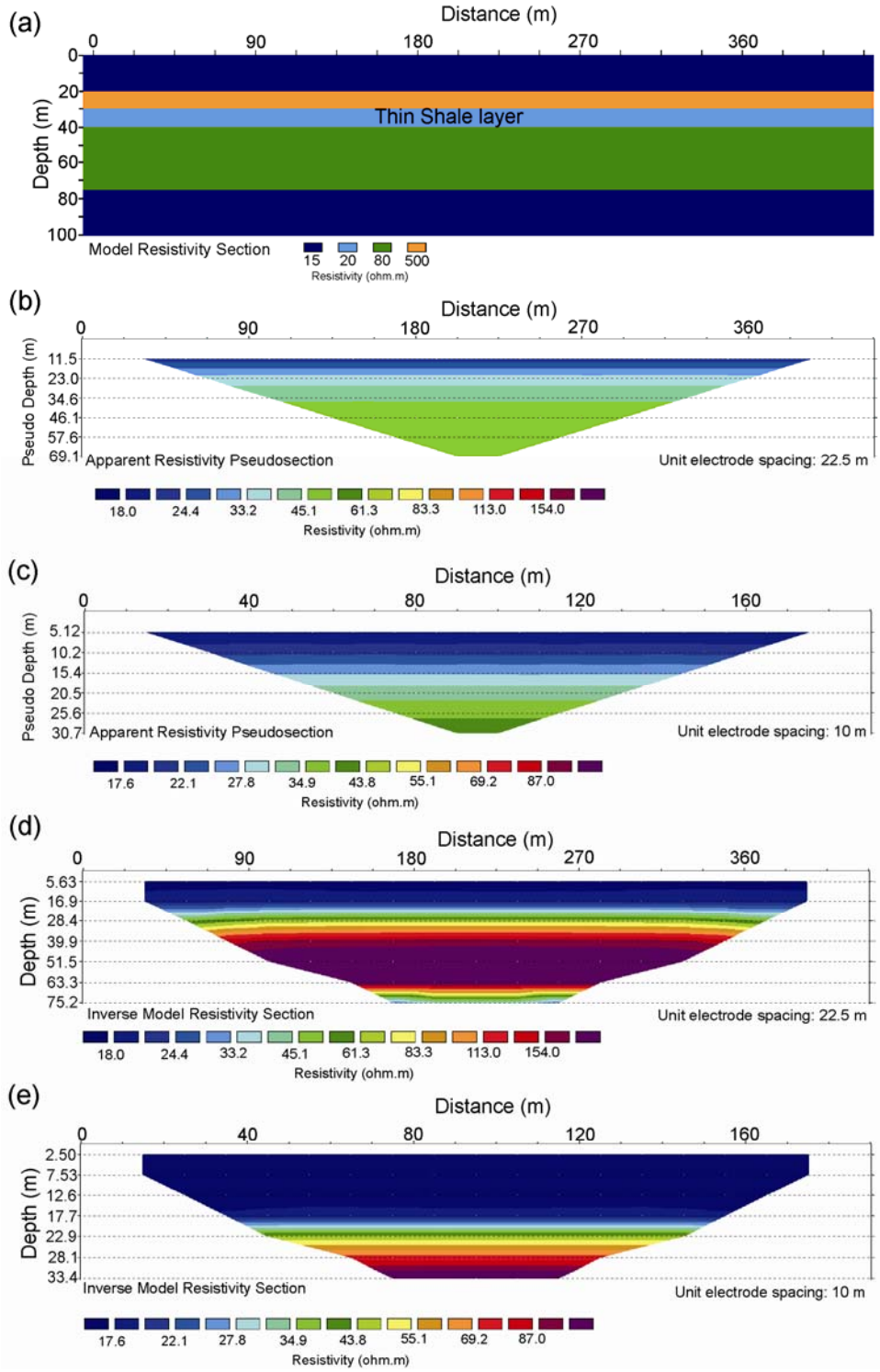

Figure 5.5. Figure caption on next page.

Figure 5.5. Forward modeling procedure carried out to determine how a thin shale layer will be imaged by ERT technique. (a) Model resistivity section. (b) Apparent resistivities response with 22.5 m electrode spacing. (c) Apparent resistivities response with 10 m electrode spacing. (d) Results of the inversion of (b). (e) Results of the inversion of (c).

The model consists of a 20 m thick homogenous conductive (i.e., 15 ohm.m) layer representing glacial sediments overlying a 10 m thick highly resistive (i.e., 500 ohm.m) bed corresponding to the sandy unit (Figure 5.5a). Underneath the highly resistive unit is a 10 m conducting (i.e., 20 ohm.m) layer, signifying the Shaftesbury shale that in turns lies over another relatively high resistive (i.e., 80 ohm.m) unit of 35 m thickness corresponding to the Peace River Formation sandstones (Figure 5.5a). The base of the model was a layer with resistivity of 15 ohm.m. The thicknesses and resistivities of the constituting layers in the model were estimated from the geophysical well logs.

A freeware called RES2DMOD by Geotomo Software, Malaysia (Loke, 2010) was employed to solve the forward modeling problem. Similar to the actual ERT surveys that was physically conducted, two sets of modeling exercise was performed with two different electrode spacings in Wenner array configuration to determine their respective apparent resistivities responses. The forward modeling was implemented to compute the apparent resistivities that will be measured in the case of 20 electrodes at 22.5 m spacing (Figure 5.5b) and 20 electrodes at 10 m spacing (Figure 5.5c). Subsequent to the forward modeling, the appropriate apparent resistivities were inverted with same parameters as outlined in Table 5.2 to produce a possible resistivity distribution that yielded the respective model responses for the 22.5 m electrode spacing (Figure 5.5d) and 10 m electrode spacing (Figure 5.5e). The inversion for both electrode spacing designs converged at 3 iterations with the final RMS error less than 2 %.

It is apparent from Figure 5.5d and Figure 5.5e that the ERT survey will not be able to clearly image a conductive Shaftesbury Formation lying between two highly resistive sand units. A possible reason for this could be the small thickness associated with the conductive layer and the low resolution results expected from the large electrode spacings. Smaller electrode spacing may likely image the conductive layer; however, the corresponding low depth of investigation would be insufficient to penetrate to the depths at which the Shaftesbury Formation occurs in the subsurface (i.e., > 100 m).

5.5 Summary

The electrical resistivity methodology utilized for the Peace River landslide study has been described in this chapter. Geoelectrical concepts pertinent to the implementation of the resistivity method were firstly discussed in the opening section of the chapter. Moving on to the description about the ERT data acquisition, the associated technicalities were explained. The nonlinear smoothness-constrained least-squares inversion technique used to generate a possible resistivity distribution of the subsurface was also discussed. The results of the ERT methodology were intended to supply a means by which the Peace River landsliding could be delineated and equally provide information about its associated processes on the basis of the contrasts in the subsurface resistivities. In addition, an ERT modeling procedure performed to determine the resistivity measurements that will be made over a specified resistivity model was described. The results of the modeling, which is valuable during subsequent interpretation of the inverted ERT data, revealed that a similar ERT survey such as was carried out at the Town of Peace River will not be able to clearly image a conductive layer (e.g., Shaftesbury shales) lying between two highly resistive (e.g., sandy) units, possibly because of limit in resolution associated with the ERT survey. As a result, the Shaftesbury Formation might not be discernable on the inverted ERT images.

Chapter 6

Results and Joint Interpretation

The results of the geophysical techniques utilized in the investigation of the Peace River landslide will be presented in detail in this chapter of the thesis. The results include the seismic reflection profile, seismic refraction tomography, zero-offset VSP data, and the inverted ERT images. These geophysical results will be subsequently interpreted jointly in order to understand the said landslide's extents and processes.

6.1 Results

A product of the 2D seismic reflection processing sequence is the poststack time-migrated seismic profile (Figure 6.1a). The horizontal axes of the profile are in terms of CMP at 3 m bin size and distance from west to east in m referenced from CMP 0 (i.e., 475006 m easting according to UTM Zone 11N) (Figure 3.1b), while the vertical coordinate is two-way traveltime in ms. The other product from the seismic reflection processing is the depth converted profile (Figure 6.1b). The seismic depth profile has the same line direction and horizontal axes as the time-migrated data; however the vertical coordinate is elevation in m a.s.l. The reflection profiles (Figures 6.1a and 6.1b) were normalized to the mean amplitudes of the respective data and displayed in color scale with positive amplitudes represented by black colors and negative amplitudes by red. Some particular areas on the 2D seismic reflection profile do not have data at shallow depths, e.g., around distances 0 to 500 m, 1100 to 1300 m, 1550 to 1650 m, 1900 to 2100 m, 4200 to 4500 m, and 4750 to 4800 m. The reason for this occurrence is minimal amount of short-offset data and low CMP folds in these areas.

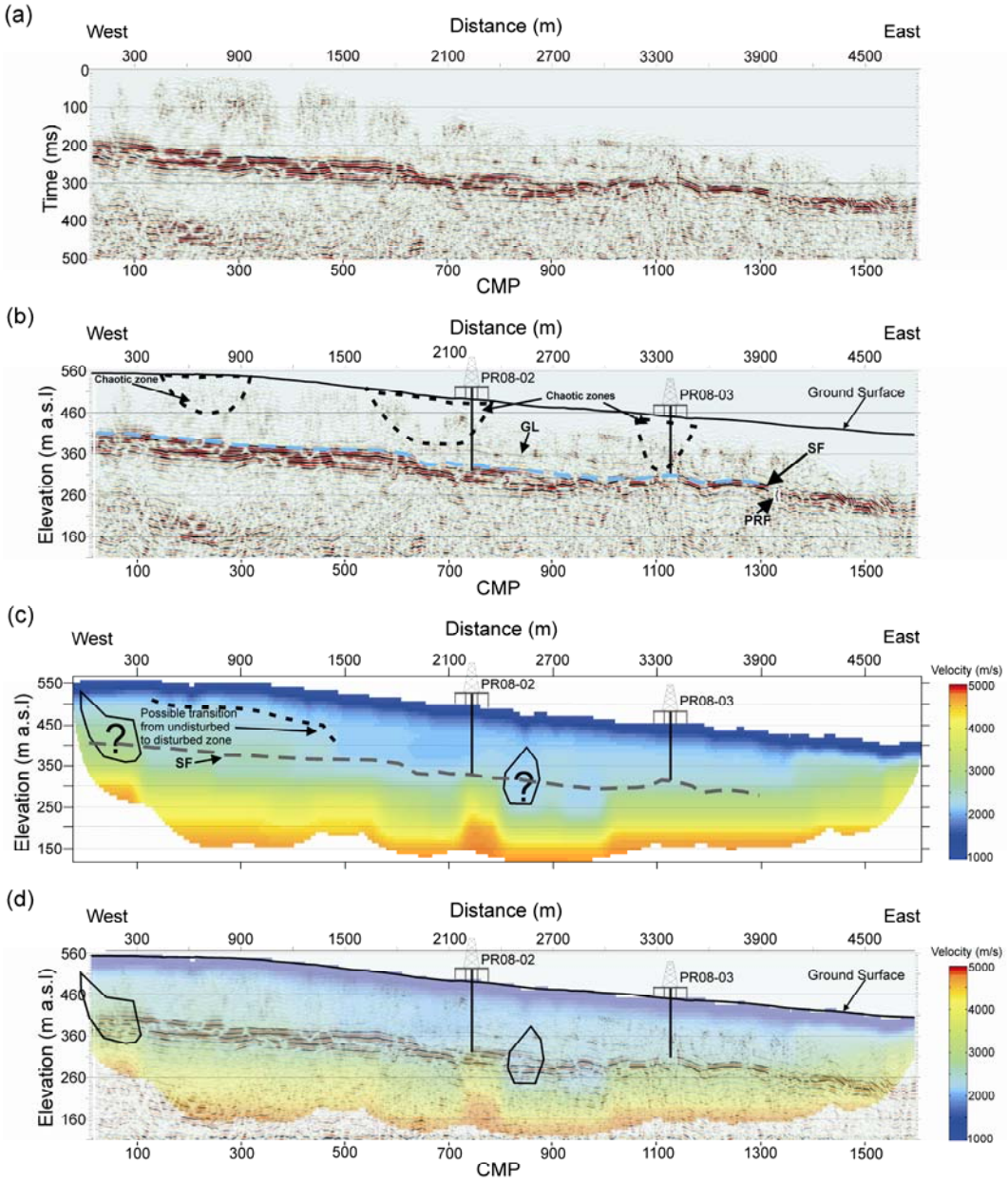

Figure 6.1. (a) Poststack time-migrated seismic section with two-way time in ms as vertical axis. (b) Corresponding final depth converted seismic profile. Chaotic zones (black broken lines) and possible top of the Shaftesbury Formation (blue broken line) are shown. (c) The interval velocities of the subsurface as obtained from the traveltime inversion with a vertical exaggeration of ~ 10. The polygons labeled with question marks are areas with no hit count obtained from Figure 4.9. Possible top of Shaftesbury Formation (gray broken line) and landslide scarp (black broken line) are shown. (d) As for (b) overlaid with the traveltime

inversion velocities and polygons indicating area of no hit count. The horizontal axis of the images is distance from CMP 0 (i.e., 475006 m easting in UTM Zone 11 N). The vertical axis of the depth images is elevation in m a.s.l. Wells PR08-02 and PR08-03, located at about distances 2230 m and 3380 m respectively, are shown on the depth images. The interpretation tags shown are **GL**: lacustrine deposits; **SF**: Shaftesbury Formation; and **PRF**: Peace River Formation.

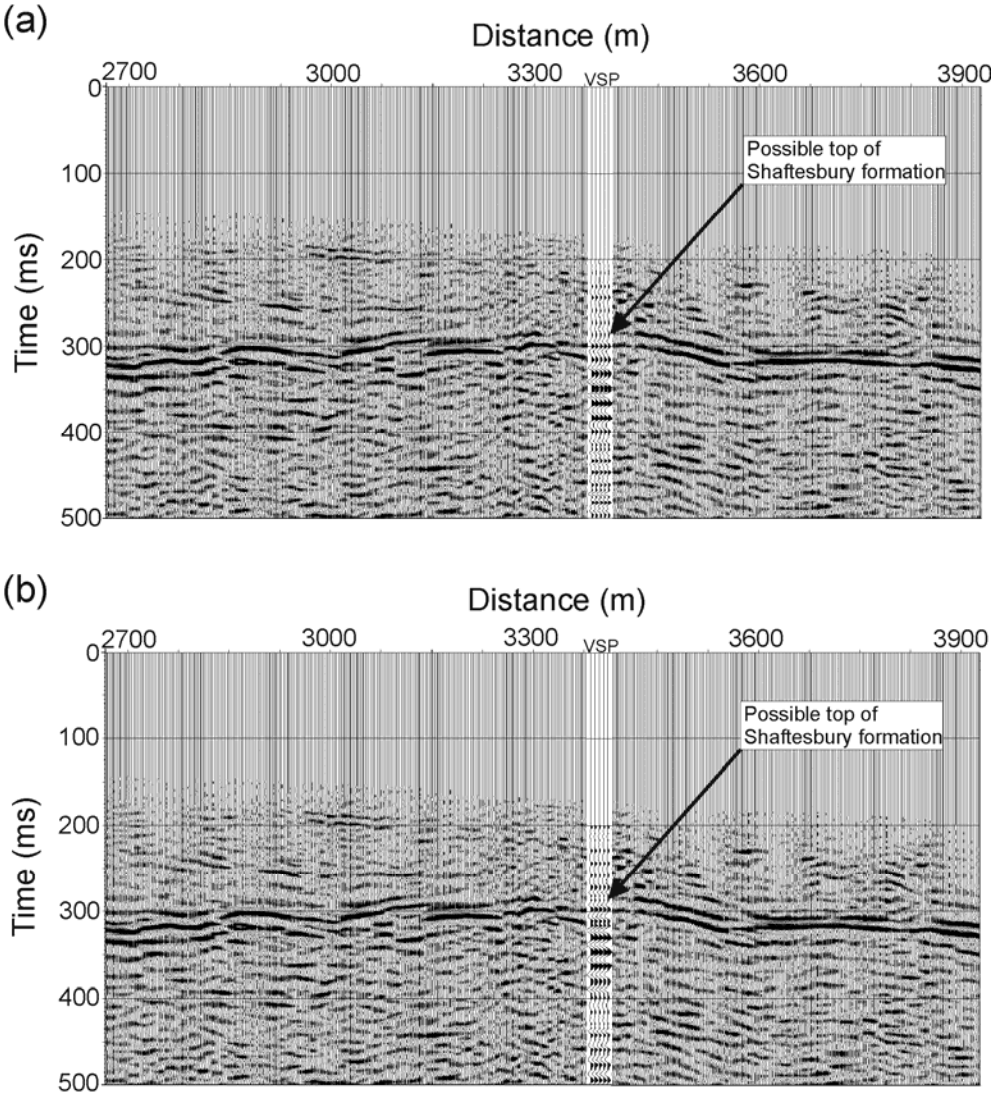

Figure 6.2. VSP data inserted into the time-migrated seismic reflection profile at the location of wellbore PR08-03 for correlation. (a) Processed reversed-polarity 0^0 VSP data. (b) Processed 180^0 VSP data. Possible top of the Shaftesbury bedrock is shown in both images.

The possible velocity distribution of the subsurface was obtained from the seismic traveltime inversion tomography (Figure 6.1c) as described in section 4.3. The value of the velocity in m/s for each point in the subsurface is represented by a color according to the scale displayed beside the tomography results. The polygons on the velocity image are areas with no ray hit coverage count (Figure 4.9) and so less confidence is placed on the tomographic results at those locations. In order to present a clear representation of the correlation between both depth-sampled images for subsequent interpretation, the seismic depth profile was overlaid with the velocity field from the traveltime tomography (Figure 6.1d).

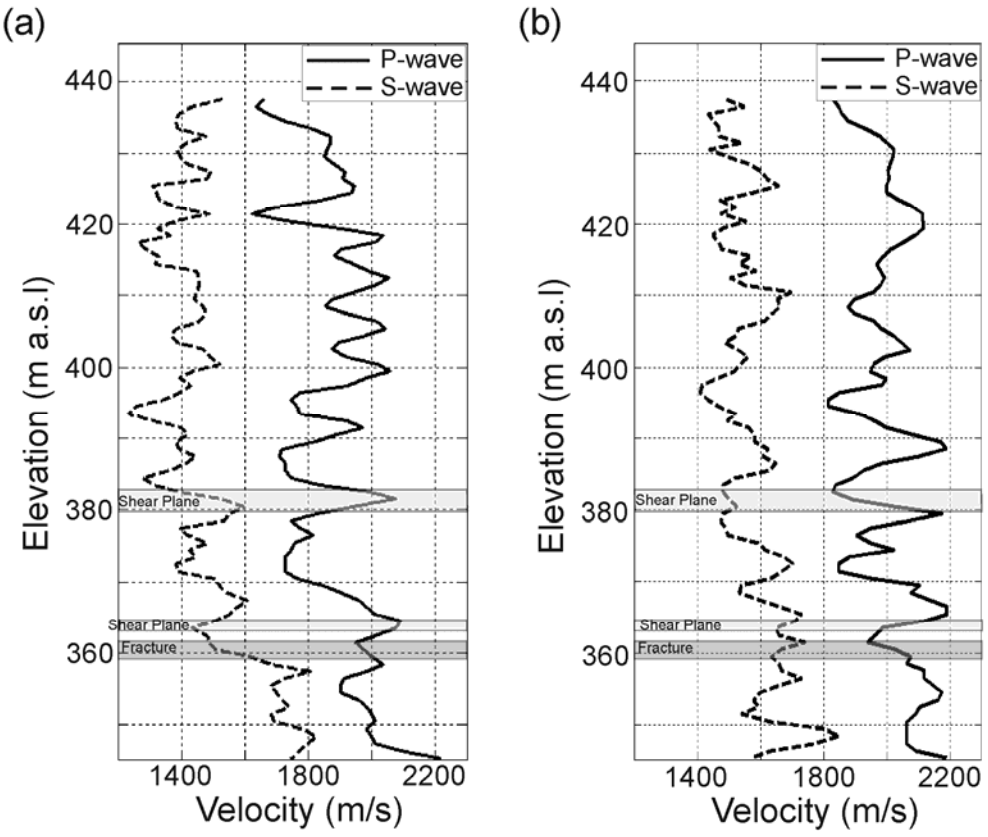

Figure 6.3. P- and S-wave interval velocities obtained from the VSP data for (a) 0^0, and (b) 180^0 polarizations. The depths at which the shear planes and fractures occur are also shown.

The seismic response of the earth near the PR08-03 borehole was determined from the zero-offset VSP dataset. The result from the VSP processing for 0^0 polarization (i.e., vibrator mass facing north) was compared to the time-migrated seismic reflection data; however, reversing the polarity of the VSP is necessary to tie the two datasets satisfactorily (Figure 6.2a). On the other hand, the 180^0 polarized VSP data (i.e., vibrator mass facing south) tied sufficiently with the seismic data without changing its polarity (Figure 6.2b). Furthermore, the possible top of the Shaftesbury Formation was identified on the two separate VSP data. However, it is uncertain whether the 0^0 VSP data is a polarity-reversed equivalent of the 180^0 VSP data or not. Moreover, close examination of the two separate polarized VSP data reveals that they do not match perfectly when the polarity of either of them is reversed, indicating that the system might not have possibly functioned in the way intended, i.e., the vibrator operation is not truly reversible when the mass is rotated.

The other purpose for performing a VSP survey in this study was to determine the interval velocities of the various formations encountered by the wellbore. The S-wave energy source used for the VSP data acquisition offered the prospect of obtaining both P- and S-wave seismic velocities in the borehole. Hence, the data was processed accordingly to obtain the compressional and shear wave interval velocities for both 0^0 (Figure 6.3a) and 180^0 VSP data polarization (Figure 6.3b). Although they were not exactly alike in trends and magnitudes, the P-wave velocities from both polarizations were less than 2250 m/s (Figure 6.3), in agreement with the velocities from the low-resolution tomography results (Figure 6.1c). Moreover, a common general drift in the two separate P-wave velocities could be established somewhat, broadly characterized by increase in velocities with depth. Although the S-wave velocities obtained from the 0^0 polarization data appear to be lower between depth sections 425 to 415 m a.s.l. and 395 to 385 m a.s.l. than at any other section; however this trend could barely be established for the 180^0 polarization S-wave velocities. Apart from these aforementioned depth sections, the observed general trend of the S-wave velocities for the two

polarization directions is that the values increase with depth to a maximum value of ~ 1800 m/s at about 345 m a.s.l. elevation.

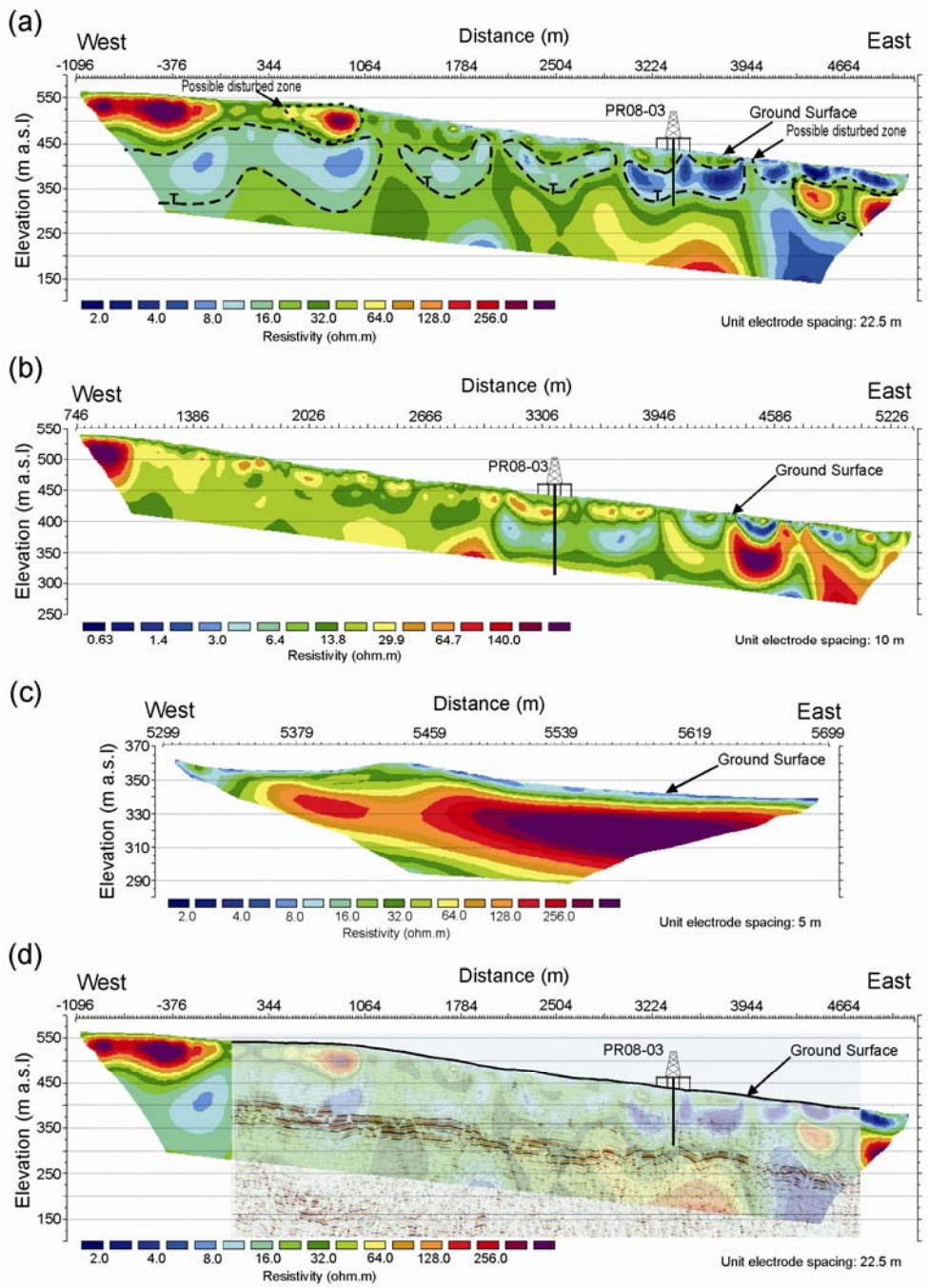

Figure 6.4. Results of the ERT data inversion. (a) 22.5 m electrode spacing line 1 overlaid with interpretation lines and tags illustrating some features. The interpretations are **T**: till, **G**: gravels, and possible disturbed zones. (b) 10 m electrode spacing line 2. (c) 5 m electrode spacing line 3. (d) 22.5 m electrode

spacing line 1 overlaid with the depth-converted seismic reflection profile. The location of well PR08-03 is displayed on the respective ERT lines it intersects.

After the inversion of the ERT datasets, the resulting resistivity field of the study area was generated for ERT line 1 (Figure 6.4a), line 2 (Figure 6.4b), and line 3 (Figure 6.4c). Similar to the seismic profile display, the horizontal axis of the ERT lines is distance from CMP 0 (i.e., 475006 m easting according to UTM Zone 11N) in m from west to east. The vertical axes for the ERT lines are elevations in m a.s.l. and each point in the subsurface for the area the data covers has an associated resistivity value specified by colors according to the logarithmic scale underneath each image. It is interesting to note that the features observed on the low-resolution ERT line 1 are also apparent on the higher-resolution independently-acquired ERT line 2, thus supporting the existence of these features from two independent measurements at differing resolutions. Additionally, for the purpose of appreciating the relationship between the ERT and seismic data, the depth-converted reflection profile was overlaid on the low-resolution ERT image (Figure 6.4d).

6.2 Joint Interpretation

The strong reflector **SF** dipping from west to east on the time and depth reflection profiles from distance 0 to ~ 3950 m between two-way traveltimes 180 and 320 ms and elevations 420 and 280 m a.s.l., respectively is the possible top of the Shaftesbury Formation (Figures 6.1a and 6.1b). The top of this formation has an uneven topography, suggesting a buried erosional surface. This erosional surface is likely to be the pre-glacial valley that was shaped by the pre-glacial Peace River and later filled with glacial sediments during the advance/retreat of the Laurentide ice sheet (J. Morgan, personal communication, 2010). Although it is not improbable to reason that the top of the Shaftesbury Formation was shaped by

erosional processes due to the shale's friability (e.g., Leslie and Fenton, 2001; Morgan et al., 2008), yet one cannot rule out the possibility that complications associated with the seismic processing caused such unevenness in the horizon's topography. According to a vertical cross-section of the area generated by Morgan et al. (2008) using logs from geophysical and geotechnical wellbores and findings from field mapping exercises, the Shaftesbury Formation has been eroded to become a few meters thick, or absent in some places near the Peace River; this appears to be in agreement with the abrupt termination of the horizon towards the Peace River at ~ 3950 m distance on the seismic sections (Figures 6.1a and 6.1b).

An interesting feature about the possible top of the Shaftesbury Formation **SF**, as observed on the reflection profiles is the surface's topographic trough from about distance 1900 to 3000 m. This feature is similar to the structure of a glacially buried valley where glacial meltwaters incised into existing bedrock to create a valley that is subsequently filled with sediments and covered up such that it is not apparent at the earth's surface (e.g., Ogunsuyi and Schmitt, 2010). It is expected that the sediments constituting the valley are not as consolidated as the stiffer Cretaceous bedrock, hence giving rise to lower compressional wave velocities. A lower material velocity trough could be observed on the tomography image between distances 1900 to 3000 m (Figure 6.1c) suggesting the presence of a small erosional channel. Although the topographic trough on the velocity image (Figure 6.1c) appears deeper than what is observed on the depth seismic reflection profile at distance 2800 to 3000 m, however the other parts of the buried valley on the 2D line seem to match on both images with the exception of the questionable area characterized by zero hit count (Figure 6.1d).

The Shaftesbury Formation is a dark grey fish-scale bearing marine shale (Hamilton et al., 1999) and it is expected to be electrically conductive because of its high clay content and established depositional history in marine environment (see Figure 3.9). However, the top of the Shaftesbury Formation is not distinguishable on the ERT data (Figure 6.4), in agreement with the results of the

ERT data modeling (see Chapter 5). The thickness of the Shaftesbury Formation is estimated to be as thin as a few meters or absent at the eastern side of the profile line (J. Morgan, personal communication, 2010) such that the low resolution (22.5 m electrode spacing) and relatively higher resolution (10 m electrode spacing) ERT surveys are unable to delineate it from the overlying and underlying higher resistivity sandy units. A higher resolution ERT survey might be required to image the Shaftesbury Formation; however the implementation would be almost impossible because the depth of investigation of the higher resolution survey is expected to be much smaller than the depth at which the formation occurs in the subsurface.

At distances between 0 to ~ 3950 m, the boundary of the Peace River Formation **PRF** with the Shaftesbury Formation cannot be clearly distinguished on the reflection profiles (Figures 6.1a and 6.1b) without additional wellbore information, although sufficient acoustic impedance contrast is expected across the Shaftesbury-Paddy interface as inferred from the geophysical logs of wellbore 00/02-27-083-22W5/0 (see Chapter 3). A possible reason for the uncertainty associated with distinguishing the Peace River Formation from the Shaftesbury Formation could be the diminishing thickness of the Shaftesbury Formation as one moves towards the east along the geophysical survey line (J. Morgan, personal communication, 2010) in conjunction with limitations in the seismic data resolution. However, the series of strong reflections observed below the Shaftesbury Formation between ~ 300 ms and ~ 350 ms on the VSP data could be associated with the Peace River Formation (Figure 6.2).

The ERT data shows a high heterogeneity in the electrical resistivities of the subsurface materials in the study area (Figures 6.4a and 6.4b). Several low resistivity sedimentary packages **T** with resistivities < 10 ohm.m are evident in the ERT data and they are interpreted to be clayey silt tills as indicated on the borehole logs (Morgan et al., 2009). Also noticeable is a high resistivity (> 128 ohm.m) package **G** at distance ~ 4300 m that is interpreted as a fluvial sand and

gravel unit. The same sand and gravel unit was observed at locations close to the Peace River at the study area (J. Morgan, personal communication, 2010), and also identified on the ERT line 3 image (i.e., highest-resolution line near the Peace River) where it was characterized by high resistivity values (> 128 ohm.m) (Figure 6.4c). However, because of the elevation at which the unit is observed, the possibility of the **G** package being a combination of gravel and the underlying Peace River Formation sandstones cannot be ruled out.

A moderately resistive area (about 48 to 128 ohm.m) below 350 m a.s.l. is observed at about distance 2150 to 3950 m (Figure 6.4a). The values registered in this area is likely to be a 'smearing' of the resistivities responses associated with the oldest fluvial sediments lying on top of the Shaftesbury Formation, the Shaftesbury shales, and the Peace River Formation sandstones. It is observed that this moderately resistive area is absent to the west of distance ~ 2150 m and to the east of ~ 3950 m (Figure 6.4a). A possible explanation for this could be the variable distribution and thickness associated with the deposition of the fluvial sediments, likely deposited by a braided river channel system that carved the pre-glacial bedrock valley (J. Morgan, personal communication, 2010). Towards the west of distance ~ 2150 m, a substantial portion of the Peace River Formation (with top at about 310 m a.s.l. elevation; Figure 3.5) might not be apparent on the data due to the limit in the depth of penetration of the ERT survey, and so a smearing of its resistivity response and that from the Shaftesbury Formation could possibly have resulted in the values observed at about 310 m a.s.l. (i.e., ~ 20 ohm.m). Below 300 m a.s.l. elevation and at distance ~ 3900 m, a sharp resistivity transition from higher to lower values is observed. At this location, the Shaftesbury Formation has possibly been completely eroded just as was noticed on the seismic reflection profile (Figure 6.1b); hence the formation is not expected to be seen beyond this point to the east on the ERT data. Furthermore, a lower resistivity (< 12 ohm.m) area is observed from this location to the east at about 250 m a.s.l. elevation (Figure 6.4a). The lower resistivities observed in this area is likely to be associated with the shaley Harmon member of the Peace River

Formation that underlies the Paddy and Cadotte sandstones, supported by the fact that the top of the Harmon member was encountered at an elevation of ~ 276 m a.s.l. in the 00/02-27-083-22W5/0 petroleum wellbore (marker top not shown in Figure 3.5 but retrieved from the IHS Canada database).

Nearly horizontal relatively strong reflectors **GL** at elevation of about 360 m a.s.l. (~ 240 ms two-way time) are noticeable on the reflection profiles at distance ~ 1900 to ~ 3200 m (Figures 6.1a and 6.1b). These **GL** reflectors could possibly be related to lacustrine sedimentation from lakes formed by the glacial meltwaters within the valley. A borehole drilled with no complementary geophysical logging by AGS (i.e., PR08-02) reveals the lithology between elevations 397 and 341 m a.s.l. to be dark grey clayey silt with fine grained sand. The **GL** events, embedded within the clayey silt package, are likely to be associated with quiet-water depositional environment (like lakes) resulting in the deposition of fine grained particles, e.g., silts and clays. These events, observed to be broken up on the seismic sections could also be related to the low-strength overconsolidated glaciolacustrine deposits that are prone to slope failures in the western Peace River Lowlands (see Chapter 3).

Slightly dipping events from east to west at ~ distance 1000 m and elevation 500 m a.s.l. (~ 80 ms) were observed on the 2D seismic line (Figures 6.1a and 6.1b). In order to determine if these features are actual reflections or stacked coherent events arising from various enhancement processing steps (e.g., Steeples and Miller, 1990; Sloan et al., 2008), nearby shot gathers were examined to validate their true nature. However, these dipping events that were observed to have lower frequencies in comparison to deeper reflections on shot records could not be confidently correlated to any true reflection and so are considered to be artifacts.

From the possible top of the Shaftesbury Formation **SF** up to ~ 460 m a.s.l. (~ 150 ms two-way time), there exist flat-lying horizons from distance 0 to ~ 1200 m (Figures 6.1a and 6.1b). The continuous nature and coherency of these reflections

could be indicative of areas unaffected or minimally affected by the landslide processes. Conversely, discontinuous and chaotic reflections were observed inside the zone bordered by black broken lines at the top of the continuous reflections from around distance 500 to 1000 m (Figure 6.1b). Such chaotic zone could be interpreted to be an area that is more disturbed by the landsliding, as a result of the seismic waves scattering taking place inside the landslide body (Figure 6.1b; e.g., Stucchi and Mazzotti, 2009).

Some other locations exhibiting discontinuous reflections indicative of areas more disturbed by the landslide include distances from ~ 1600 to ~ 2300 m and from ~ 3200 to ~ 3500 m (Figure 6.1b). Additionally, at around distance 3900 to 4700 m, upward-curved events are observed. Although these features could be related to artifacts introduced by inaccurate stacking velocities, however, similar small concave-upward features coinciding with minor landslides were also observed by Stucchi and Mazzotti (2009) within a larger landslide. Notwithstanding, the Peace River landslide has been previously determined to be a relict, retrogressive, translational earth slide (J. Morgan, personal communication, 2010), hence the concave-upward events evident on the seismic profile (Figure 6.1b) could be likely related to undulating rupture surfaces that characterize translational slides (e.g., Cruden and Varnes, 1996). Considering the extent of the interpretations made from the seismic data, one can infer that the characters of various seismic reflections observed on any carefully and accurately processed reflection profile is able to provide valuable information in distinguishing the areas more affected by landslides from the undisturbed or relatively less disturbed zones.

From the ground surface down to elevation of about 325 m a.s.l., a lateral variation in the interval velocities is evident (Figure 6.1c). Particularly at distance ~ 1500 m, a transition from higher velocities (~ 2500 m/s) to lower velocities (~ 2100 m/s) from west to east is observed. Such velocity evolution from west to east could likely indicate transition from relatively undisturbed to more disturbed areas with lower velocities likely associated with regions affected by the landslide

processes (e.g., Jongmans and Garambois, 2007). Moreover, the boundary between the relatively undisturbed to more disturbed zone could indicate a possible scarp of the landslide (Figure 6.1c). Furthermore, a decrease in velocities from ~ 2100 m/s to ~ 1800 m/s is obvious at distance ~ 1900 m from west to east. The region associated with the velocity decrease at distance ~ 1900 m corresponds to a region where discontinuous reflections were observed on the seismic reflection profile (i.e., distance from ~ 1600 to ~ 2300 m; Figure 6.1b). Since P-wave velocities are typically lower within landslide bodies than in undisturbed rocks (Jongmans and Garambois, 2007), the lowering of velocities in this area suggests the presence of a disturbed mass containing fractures and broken-up materials. At about distance 3900 to 4700 m, shallow seemingly concave-upward features, similar to what was observed on the reflection profile are apparent (Figure 6.1). Again, these features could be artifacts, however the possibility of them been real events cannot be overruled, more so that two different geophysical methods support their existence.

The interval velocities estimated from the VSP (Figure 6.3) may be unable to exactly reveal the small scale variations in the properties of the rock as would a higher frequency sonic log because of limit in sensitivity and the associated averaging method by which the velocities were obtained, i.e., least squares fitting of a line to a number of congruous time picks. Moreover, without a sonic log to validate the accuracy of the velocities, it is reasonable to avoid over-interpreting the velocities from the VSP. At the depths where the shear planes and fractures occur in the PR08-03 wellbore, there appears to be no clear relationship between the defects and the velocities (Figure 6.3). At the depth sections where shear planes and fractures occur, the P- and S-wave velocities are expected to be lower than at other undisturbed sections; however this was not always the case, e.g., increase in velocities at the shear plane interval at 382 m a.s.l. elevation were observed on the 0^0 polarization data (Figure 6.3a). Additionally, considering the differences in the velocities obtained from the 0^0 and 180^0 polarization data, it may not be possible without additional information to determine which data is a

better accurate representation of the physical properties of the materials in the borehole. Furthermore, there appears to be no obvious correlation between the lithology of the wellbore and the interval velocities (Figures 3.7 and 6.3). Again, this is likely in part to the poor vertical resolution of the times determined.

The high electrical resistivity (> 128 ohm.m) area at distance ~ 450 to ~ 1050 m and elevation ~ 500 m a.s.l. observed on the low resolution ERT data (Figure 6.4a) coincides with the region associated with discontinuous reflections on the seismic profile (Figure 6.1b). In the near surface region where electrical conductivity is mostly due to ionic conduction through the groundwater (Knight and Endres, 2005), such high resistivities can be interpreted to be associated with a dry formation. The likely disturbed area, characterized by high resistivity values can be contrasted with the unaffected areas exhibiting lower values of resistivity (< 50 ohm.m). Higher resistivities have been observed within landslide bodies in comparison to that noticed within undisturbed areas due to presence of voids inside the fractured landslide mass (e.g., Meric et al., 2005). Accordingly, the high resistivity values in the landslide body could be as a result of substantial degree of fracturing related to air-filled spaces in the deformed mass. Alternatively, this high resistivity area could possibly be gravel deposits, as observed at distance ~ 4300 m (Figures 6.4a and 6.4b) and so the interpreted landslide affected area might be related to the retrogressed part of the landslide that probably started further away from the east. Without additional information, however, the cause of the slope failure at this location could not be ascertained.

Similar concave-upward features as were observed on both seismic reflection profile and tomography images are also apparent on the ERT data at about distances 3950 to 4700 m (Figure 6.4a and b). The agreement between the results of the three geophysical methods at this location substantiates the interpretation that there is a possible occurrence of translational landslide with undulating surface of rupture at this area. In contrast to the possible landslide at distance ~ 450 to ~ 1050 m, the interpreted landslide body at distance ~ 3950 m has lower

resistivity values (< 4 ohm.m) than the surrounding materials. This could be due to a high content of clayey material and/or increase in water content within the interpreted landslide mass. With clay materials having low natural strength (e.g., Cruden and Varnes, 1996), the landslide could have been triggered by considerable water influx into the lacustrine sediments, probably from the ancient Peace River, which might have resulted in loss of cohesion between the clay minerals, thus causing the slide to occur. This zone, interpreted to have high clay content might also be related to the glaciolacustrine deposits that are prone to slope failures in the region. Contrasts in layered sequences like permeable sands alternating with weak impermeable clays (or shales) can also cause slope failures (e.g., Cruden and Varnes, 1996); hence, the high resistivity package sandwiched between two low resistivity sequences could be a source of weakness. For this particular zone of the Peace River study area, lithology could be assumed to have played a major role in the slope stability.

An extended interpretation of these data would be to integrate what is observed on the LiDAR image with the geophysical results. From the LiDAR data, the landslide seems to begin at about distance 1300 m (marked with an arrow) and end just to the east of the PR08-03 wellbore (Figure 6.5a). The elevation model obtained from the LiDAR provides the topography of the ground surface along the geophysical profile line and this was used to determine five possible boundaries of sliding block units, shown in broken lines and labeled 1 to 5 (Figure 6.5b). The reflection seismic signature do not appear to change laterally at the locations of the slide unit boundaries 1, 2, and 4 (Figure 6.5c). On the other hand, lateral variations in the reflection seismic character, defined by transitions from coherent reflection to less coherent events are observed at locations of the slide unit boundaries 3 and 5 (Figure 6.5c). These boundary locations could be related to the rupture surfaces of individual sliding block units. The seismic refraction tomography of the subsurface also shows transitions in velocities at the locations of slide unit boundaries 1 to 5 (Figure 6.5d). Further, there are noticeable but subtle changes in the resistivity values across slide unit boundaries 1, 3, and 5

(Figure 6.5e). As a result, there is possibility that there are changes in stratigraphy across boundaries 1, 3, and 5. The interpretations made here demonstrate that if there are significant contrasts in the physical properties of the different sliding block units within a landslide, it is possible to obtain valuable information about the boundaries and the rupture surfaces of the units. Integrating results of geophysical studies with the digital elevation model data obtained from LiDAR suggests a promising approach in the investigation of landslides.

The interpretations made herein are from a geophysical viewpoint and they are considered to be incomplete and deemed to represent the condition (i.e., static representation) of the Peace River mass movement at the time of the data acquisition because they are based on the results from a one-time geophysical characterization and available wellbore information about the landslide. In addition, these results may need to be combined with existing and future geotechnical data as well as time-lapsed geophysical studies to assess the future state of the mass movement in order to determine if it will stay inactive or become active. Furthermore, for a more complete analysis of the Peace River landslide processes, it is necessary to complement the geophysical interpretations made in this research with a comprehensive geological evaluation of the mass movement. To this end, performing an additional interpretation using the comprehensive regional geological report of the Peace River landslide that is currently being prepared by AGS (J. Morgan, personal communication, 2010) in combination with the above geophysical inferences will be very valuable in providing a broader picture of the landslide processes.

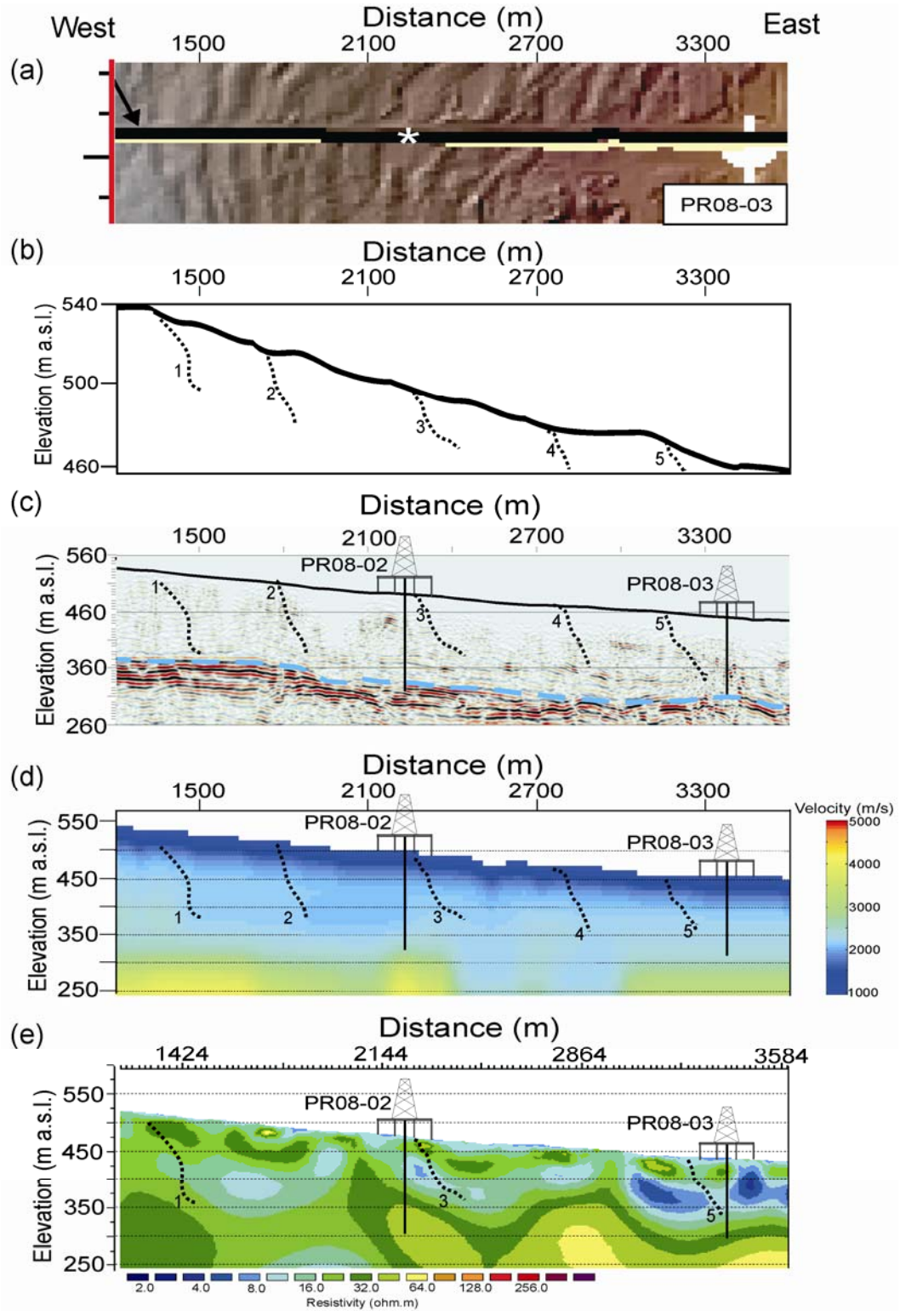

Figure 6.5. Magnified sections of the landslide zone as determined from the LiDAR data, i.e., distance 1200 to 3600 m. (a) LiDAR data with arrow showing

probable location of the beginning of the landslide. (b) Ground topography data. (c) Seismic reflection profile. (d) Seismic refraction tomography. (e) Low resolution ERT line 1 data. The broken lines on figures (b) to (e) are possible boundaries of the translational sliding block units as determined from the LiDAR.

6.3 Summary

The results of the geophysical tools employed (i.e., seismic reflection, seismic refraction tomography, VSP, and ERT) to investigate the Peace River landslide have been presented in this chapter. Also, a combined interpretation of the results of the geophysical methods and wellbore geophysical logs was also performed and discussed. Consequently, the top of the slide-prone Shaftesbury bedrock was interpreted to be shaped by erosional processes due to its uneven topography. In addition, a small erosional channel was identified near the top section of the Shaftesbury bedrock in the middle of the seismic profile line, indicated by the presence of a topographic trough on the Shaftesbury horizon and corresponding lower material velocities.

On the basis of the continuity of reflections or lack of it on the seismic profile, coherent reflections were interpreted to characterize areas less affected by the landslide processes while chaotic reflections were inferred to occur within more disturbed bodies. To this end, one can infer that the characters of various seismic reflections observed on any carefully and accurately processed reflection profile is able to provide information in distinguishing the areas affected by landslides from the undisturbed zones, or perhaps levels of disturbance within landslide debris. Also, velocity evolution from west to east along the profile line was interpreted to indicate transition from undisturbed to disturbed areas with lower velocities likely associated with regions affected by the landslide processes due to the presence of fractures and broken-up materials inside the landslide bodies.

Two systems of landslide processes were interpreted to occur in the study area based on the results from the ERT dataset. High resistivity values characterize the location of the first landslide process at the western side of the profile and it is presumed to be associated with a substantial degree of fracturing related to air-filled spaces in the deformed mass. Alternatively, this affected area could be associated with the retrogressed part of the landslide that probably started at the eastern side, in which case the high resistivity observed on the ERT profile can then be attributed to sand/gravel deposits. Without additional information, the cause of the slope failure at this area cannot be established. The second system, occurring at the eastern side of the line, is typified by low resistivity values and the area is interpreted to contain high content of clayey material and/or high water saturation. Lithology is therefore inferred to play a major role in the slope stability at the location of the second landslide process. In addition, the boundaries of the different sliding block units within the landslide were somewhat demarcated by integrating the geophysical results with the LiDAR data; thus highlighting the potential effectiveness of this approach to landslide investigations. However, these geophysical interpretations are deemed to be incomplete, subject to a comprehensive geological evaluation of the Peace River landslide.

Chapter 7

Conclusions and Future Work

7.1 Conclusions

The Peace River Lowlands of Alberta and British Columbia is one of the most historically active mass movement areas in Western Canada with landslides occurring throughout the Holocene epoch and presently in the region. The purpose of this research was to provide an understanding of the processes and extents of one such landslide situated on a major slope at the Town of Peace River, Alberta by means of geophysical techniques with the aim of reducing the landslide risk to lives and infrastructure. Due to the anticipated contrasts between the physical properties of the disturbed and the undisturbed mass, the results from the geophysical characterization of the landslide is expected to provide valuable knowledge about the subsurface structure and the possible processes associated with the slope instability.

Seismic and electrical resistivity methods in combination with existing geophysical wellbore logs were employed in carrying out the study of the landslide. The research involved the acquisition, processing, and interpretation of the seismic and electrical resistivity datasets. These geophysical methods were utilized to peer beneath the ground surface, thus resulting in the generation of static images of the earth's interior on the basis of the differing physical properties of the materials in the subsurface.

A P-wave 2D high-resolution seismic reflection dataset was acquired at the Town of Peace River over a location established, by means of high-resolution LiDAR image, to span landslide disturbed and undisturbed areas. The data was

subsequently processed in a processing sequence optimized to suppress source-generated noise that characterized the data. The result was a seismic reflection profile image that revealed the architecture of the various geologic units in the subsurface down to the Cretaceous bedrock. The acquired seismic reflection data also contained refraction waves that were used to generate a tomographic velocity distribution of the subsurface through first arrival traveltimes inversion. The seismic tomographic image offers a means whereby the velocity contrasts of the different subsurface materials can be used to distinguish them.

Zero-offset and walkaway vertical seismic profiling (VSP) were carried out in a nearby geotechnical wellbore to determine the seismic response of the formations in the vicinity of the borehole for the purpose of performing a tie with the reflection data and to provide information about seismic anisotropy, respectively. However the walkaway VSP data were unusable due to faulty downhole tool and noise, and so the analysis was limited to the zero-offset data only. S-wave type of energy source was used for the data acquisition with the objective that both P- and S-wave information could be obtained from the exercise. However, several problems were encountered with regard to the data collected, thus warranting an unconventional approach to process the data. One of the problems was the uncharacteristic behavior exhibited by the vibroseis field pilot traces that are required for cross-correlation purposes. A time-variant band-pass filter was successfully designed and used to correct the traces' anomalous nature without any apparent adverse effect on the data. In addition, preliminary analysis performed on the first-breaks of the correlated VSP data appeared to suggest that the seismic waves generated during the data acquisition travelled through both the wellbore steel casing and the geologic formation, thus causing the desired energy through the formation to be masked by that through the steel casing on the resulting data. In order to suppress the seismic energy travelling through the steel casing, τ–p filtering method was used to limit the range of permitted slowness. The fair tie of the resulting VSP images to the seismic reflection data appears to suggest that the τ–p procedure was able to suppress the wavefield through the

steel casing. To the best of my knowledge, I have not been able to establish in available near-surface VSP literature anywhere similar processes have been adopted to solve such problems. However, the results from these unconventional VSP procedures performed here should be treated as work in progress, pending further studies.

Additionally, electrical resistivity tomography (ERT) datasets were acquired at the study area. The measured apparent resistivities were inverted to produce an image of the possible true resistivities of the subsurface. The ERT method was expected to provide details about the landsliding and its associated processes on the basis of the resistivity field distribution obtained from the inverted image. ERT data modelling was also performed to aid in the data interpretation by providing information about the consequent response of the resistivity method over a model that contains a thin layer of low resistivity that is sandwiched between two higher resistivity units.

The slide-prone Shaftesbury bedrock, interpreted to be erosional due to its uneven topography, was identified on both the seismic reflection and the zero-offset VSP data. However, the top of the shaly Shaftesbury that is expected to have low resistivity response was indistinguishable on the ERT due to the surrounding higher resistivity bodies that obscured it and the inherent limit in the resolution of the ERT survey. The inadequacy of the ERT survey to image the top of the Shaftesbury Formation clearly was not unexpected because it was consistent with the results from the resistivity modeling.

Based on the reflections continuity or lack of it, interpretations were made on the 2D seismic reflection profile to determine the possible areas more affected by the landsliding and the relatively less disturbed zones. Chaotic reflections were interpreted to occur within the more disturbed bodies due to wave scattering, and continuous reflections were presumed to characterize the comparatively less disturbed areas. In addition, velocity decrease along the profile line from west to

east, as was observed on the seismic tomography was interpreted to indicate transition from less disturbed to more disturbed areas, with regions affected by the landslide processes deduced to be characterized by lower relative velocities due to presence of fractures and broken-up materials.

An area with concave-upward events was inferred to be associated with translational landslides. These events were somewhat observed on the seismic reflection, tomography, and ERT data at about the same location, thus substantiating the interpretation that there is a possible occurrence of translational slide with undulating rupture surface at this area. Based on the results from the ERT dataset, two regimes of landslide processes were interpreted to occur in the study area. The first system was observed to occur at a location characterized by high resistivities that is presumed to be associated with a substantial degree of fracturing in air-filled spaces in the deformed mass and also possibly related to the retrogressed part of the landslide that probably started further to the east. However, additional information is required to ascertain the cause of the slope failure at this location. The second regime, typified by low resistivities, is inferred to contain high content of clayey material and/or high water saturation. At this location, lithology is interpreted to play a major role in slope stability. In addition, the boundaries of the different sliding block units within the landslide were somewhat delineated by integrating the geophysical results with the LiDAR data; thus highlighting the potential usefulness of this approach to landslide investigations. However, these geophysical interpretations are considered to be incomplete, subject to a comprehensive geological evaluation of the landslide.

Landslides can be very complex and heterogeneous, and imaging them can be equally challenging as a result of the often associated rough terrain and complicated nature of the landslide bodies. Although employing geophysical methods comes with its challenges, e.g., correlating generated images of physical properties to actual material properties, limitations in resolution, artifacts introduced by cultural and source-generated noises that could cause

misinterpretations, etc., nevertheless the advantages associated with using geophysics make it a preferred approach in investigating landslides. Utilizing a single geophysical method may be insufficient in conducting a comprehensive landslide study, however employing various complementary geophysical techniques and performing a joint interpretation of the results, as carried out in this thesis, could provide important insights into the landslide processes and the causes of the mass movement. The subsurface information provided by this study would be very useful to the geotechnical personnel and engineers for the purpose of carrying out a feasible and effective landslide mitigation procedure at the Peace River area. In conclusion, putting a lot of efforts into the acquisition and processing of geophysical datasets can yield important functional details, as demonstrated in this geophysical study of the Peace River landslide.

7.2 Future Work

A simple time-to-depth conversion using the stacking velocities picked on conventional CMP supergathers was carried out on the seismic reflection data in this study. Although the results are not considered inaccurate, a better representative image of the subsurface might be a prestack depth migrated section. In order to determine if the result of the time-to-depth conversion is adequate, it is suggested that a prestack depth migration (PSDM) procedure using velocities from the seismic tomography should be performed on the dataset. Although the velocities from the seismic tomography that serve as input into the PSDM algorithm could be used successfully as it is for the procedure (e.g., Ogunsuyi and Schmitt, 2010), however, an iterative refinement of the velocities might be necessary for improved results (e.g., Bradford and Sawyer, 2002; Bradford et al., 2006).

The seismic and ERT profiles presented in this study illustrate a 2D image of the subsurface. Since landslides are generally complex, the 2D geophysical methods

may not have provided a complete and descriptive image of the landslide area. Firstly, the north-south lateral geometry of the landslide cannot be determined from the 2D data. Secondly, there is a possibility that one is imaging an uneven 3D structure into the 2D profile that could result in data misinterpretation. In order to address these challenges and thus provide a 3D geometry of the landslide, 3D seismic and ERT surveys would be essential. A geophysical time-lapse data acquisition might also be necessary in providing information about the mass movement evolution over time.

Cores from the geotechnical wellbores located at the study area might present more information about the landslide processes. Potential future work would be to perform various laboratory measurements on these cores, including P- and S-wave velocities estimations, which could provide valuable insight about the stability, strength, and anisotropy of the materials affected by the landsliding. Incorporating these measurements with the results obtained in this study, a representative subsurface model of the area could be generated.

The validity and accuracy of the analyses performed on the VSP data in this study require further investigations, since the procedures are considered preliminary. The analyses are novel approaches employed in resolving the problems associated with the vibroseis field pilot traces and in separating the desired seismic energy travelling through the formation from that traveling through the steel casing. In addition, the horizontal components of the zero-offset VSP datasets could also be processed to obtain the S-wave acoustic reflectivity signature of the various formations near the borehole. Furthermore, a future VSP survey should attempt to use instead only the P-wave vibrator that yields much greater signal strength.

In an attempt to obtain more information about the Peace River landslide, other geophysical methods like microseismic monitoring that might serve to predict impending movement, gravimetric measurements, and magnetic field observations could be utilized.

References

Agnesi, V., M. Camarda, C. Conoscenti, C. Di Maggio, I. S. Diliberto, P. Madonia, and E. Rotigliano, 2005, A multidisciplinary approach to the evaluation of the mechanism that triggered the Cerda landslide (Sicily, Italy): Geomorphology, **65**, 101–116.

Aritman, B. C., 2001, Repeatability study of seismic sources signatures: Geophysics, **66**, 1811–1817.

Azzoni, A., S. Chiesa, A. Frassoni, and M. Govi, 1992, The Valpola landslide: Engineering Geology, **33**, 59–70.

Baker, G. S., D. W. Steeples, and M. Drake, 1998, Muting the noise cone in near-surface reflection data: An example from southeastern Kansas: Geophysics, **63**, 1332–1338.

Batayneh, A. T., and A. A. Al-Diabat, 2002, Application of a two-dimensional electrical tomography technique for investigating landslides along the Amman–Dead Sea highway, Jordan: Environmental Geology, **42**, 399–403.

Beaty, K. S., and D. R. Schmitt, 2003, Repeatability of multimode Rayleigh-wave dispersion studies: Geophysics, **68**, 782–790.

Bergman, B., A. Tryggvason, and C. Juhlin, 2006, Seismic tomography studies of cover thickness and near-surface bedrock velocities: Geophysics, **71**, no. 6, U77–U84.

Bichler, A., P. Bobrowsky, M. Best, M. Douma, J. Hunter, T. Calvert, and R. Burns, 2004, Three-dimensional mapping of a landslide using a multi-geophysical approach: the Quesnel Forks landslide: Landslides, **1**, 29–40.

Black, R. A., D. W. Steeples, and R. D. Miller, 1994, Migration of shallow seismic reflection data: Geophysics, **59**, 402–410.

Bogoslovsky, V. A., and A. A. Ogilvy, 1977, Geophysical methods for the investigation of landslides: Geophysics, **42**, 562–571.

Brabb, E. E., and B. L. Harrod, eds., 1989, Landslides: extent and economic significance: Proceedings of the 28th International Geological Congress Symposium, Washington D.C., A. A. Balkema Publisher.

Bradford, J. H., and D. S. Sawyer, 2002, Depth characterization of shallow aquifers with seismic reflection – Part II: Prestack depth migration and field examples: Geophysics, **67**, 98–109.

Bradford, J. H., L. M. Liberty, M. W. Lyle, W. P. Clement, and S. Hess, 2006, Imaging complex structure in shallow seismic-reflection data using prestack depth migration: Geophysics, **71**, no. 6, B175–B181.

Bruno, F., and F. Marillier, 2000, Test of high-resolution seismic reflection and other geophysical techniques on the Boup landslide in the Swiss Alps: Surveys in Geophysics, **21**, 333–348.

Buchholtz, H., 1972, A note on signal distortion due to dynamic (nmo) corrections: Geophysical Prospecting, **20**, 395–402.

Canales, L. L., 1984, Random noise reduction: 54th Annual International Meeting, SEG, Expanded Abstracts, 525–527.

Caris, J. P. T., and Th. W. J. Van Asch, 1991, Geophysical, geotechnical and hydrological investigations of a small landslide in the French Alps: Engineering Geology, **31**, 249–276.

Castle, R. J., 1994, A theory of normal moveout: Geophysics, **59**, 983–999.

Catto, N. R., D. G. E. Liverman, P. T. Bobrowsky, and N. Rutter, 1996, Laurentide, Cordilleran, and montane glaciation in the western Peace River – Grande Prairie, Alberta and British Columbia, Canada: Quaternary International, **32**, 21–32.

Chambers, J. E., O. Kuras, P. I. Meldrum, R. D. Ogilvy, and J. Hollands, 2006, Electrical resistivity tomography applied to geologic, hydrogeologic, and engineering investigations at a former waste-disposal site: Geophysics, **71**, no. 6, B231–B239.

Claerbout, J. F., 1985, Imaging the earth's interior: Blackwell Scientific Publications.

Crosta, G. B., S. Imposimato, and D. G. Roddeman, 2003, Numerical modelling of large landslides stability and runout: Natural Hazards and Earth System Sciences, **3**, 523–538.

Cruden, D. M., M. Ruel, and S. Thomson, 1990, Landslides along the Peace River, Alberta: 43rd Canadian Geotechnical Conference Proceedings, **1**, 61–68.

Cruden, D. M., and D. J. Varnes, 1996, Landslides types and processes, *in* A. K. Turner, and R. L. Schuster, eds., Landslides investigation and mitigation:

Transportation Research Board, National Research Council, Special Report, **247**, 36–75.

Cummings, D., 2000, Transient electromagnetic survey of a landslide and fault, Santa Susanna Mountains, southern California: Environmental and Engineering Geoscience, **6**, 247–254.

Dahlin, T., C. Bernstone, and M. H. Loke, 2002, A 3-D resistivity investigation of a contaminated site at Lernacken, Sweden: Geophysics, **67**, 1692–1700.

Daily, W., and E. Owen, 1991, Cross-borehole resistivity tomography: Geophysics, **56**, 1228–1235.

Daily, W., A. Ramirez, A. Binley, and D. LaBrecque, 2005, Electrical resistivity tomography – theory and practice, *in* D. K. Butler, ed., Near-surface geophysics, Investigations in Geophysics, **13**: Society of Exploration Geophysicists, 525–561.

Davies, M. R., R. C. Paulen, and A. S. Hickin, 2005, Inventory of Holocene landslides, Peace River area, Alberta (NTS 84C): Alberta Energy and Utilities Board, EUB/AGS Geo-Note 2003-43.

Del Gaudio, V., J. Wasowski, P. Pierri, U. Mascia, and G. Calcagnile, 2000, Gravimetric study of a retrogressive landslide in southern Italy: Surveys in Geophysics, **21**, 391–406.

Dillon, P. B., and R. C. Thomson, 1984, Offset source vsp surveys and their image reconstruction: Geophysical Prospecting, **32**, 790–811.

Dix, C. H., 1955, Seismic velocities from surface measurements: Geophysics, **20**, 68–86.

Drahor, M. G., G. Göktürkler, M. A. Berge, and T. O. Kurtulmuş, 2006, Application of electrical resistivity tomography technique for investigation of landslides: a case from Turkey: Environmental Geology, **50**, 147–155.

Eisbacher, G. H. and J. J. Clague, 1984, Destructive mass movements in high mountains: hazard and management: Geological Survey of Canada Paper, **84-16**.

Ellis, D. V., and J. M. Singer, 2007, Well logging for earth scientists: Springer.

Embree, P., J. P. Burg, and M. M. Backus, 1963, Wide-band velocity filtering—the pie-slice process: Geophysics, **28**, 948–974.

Eshraghian, A., C. D. Martin, and D. M. Cruden, 2007, Complex earth slides in the Thompson River Valley, Ashcroft, British Columbia: Environmental and Engineering Geoscience, **13**, 161–181.

Fenton, M. M., 1984, Quaternary stratigraphy, Canadian Prairies, *in* R. J. Fulton, ed., Quaternary Stratigraphy of Canada – A Canadian contribution to IGPC Project 24: Geological Survey of Canada Paper, **84-10**, 57–68.

Ferrucci, F., M. Amelio, M. Sorriso-Valvo, and C. Tansi, 2000, Seismic prospecting of a slope affected by deep-seated gravitational slope deformation: the Lago Sackung, Calabria, Italy: Engineering Geology, **57**, 53–64.

Froese, C. R., 2007, The Peace River Landslide Project: Hazard and Risk Assessment for Urban Landslides: Proceedings of the 60th Canadian Geotechnical Conference Ottawa, ON, 699–704.

Gardner, L.W., 1939, An aereal plan of mapping a subsurface structure by refraction shooting: Geophysics, **4**, 247–259.

Geyer, R. L., 1970, The vibroseis system of seismic mapping: Canadian Journal of Exploration Geophysics, **6**, 39–57.

Godio, A., and G. Bottino, 2001, Electrical and electromagnetic investigation for landslide characterization: Physics and Chemistry of the Earth, Part C: Solar, Terrestrial and Planetary Science, **26**, 705–710.

Godio, A., C. Strobbia, and G. De Bacco, 2006, Geophysical characterisation of a rockslide in an alpine region: Engineering Geology, **83**, 273–286.

Göktürkler, G., Ç. Balkaya, and Z. Erhan, 2008, Geophysical investigation of a landslide: The Altındağ landslide site, İzmir (western Turkey): Journal of Applied Geophysics, **65**, 84–96.

Green, R., 1974, The seismic refraction method—a review: Geoexploration, **12**, 259–284.

Hack, R., 2000, Geophysics for slope stability: Surveys in Geophysics, **21**, 423–448.

Hagedoorn, J. G., 1959, The plus-minus method of interpreting seismic refraction sections: Geophysical Prospecting, **7**, 158–182.

Hamilton, W. N., M. C. Price, and C. W. Langenberg (compilers), 1999, Geological map of Alberta: Alberta Energy and Utilities Board, EUB/AGS Map 236, scale 1:1000000.

Hampson, D., and Russell B., 1984, First-break interpretation using generalized linear inversion: Canadian Journal of Exploration Geophysics, **20**, 40– 50.

Hardage, B. A., 2000, Vertical seismic profiling method: principles: Seismic exploration, vol. **14**, Pergamon, Elsevier Science.

Hauck, C., D. V. Mühll, and H. Maurer, 2003, Using dc resistivity tomography to detect and characterize mountain permafrost: Geophysical Prospecting, **51**, 273–284.

Havenith, H. -B., D. Jongmans, K. Abdrakhmatov, P. Trefois, D. Delvaux, and I. A. Torgoev, 2000, Geophysical investigations of seismically induced surface effects: case study of a landslide in the Suusamyr valley, Kyrgyzstan: Surveys in Geophysics, **21**, 349–369.

Heincke, B., T. Günther, E. Dalsegg, J. S. Rønning, G. V. Ganerød, and H. Elvebakk, 2010, Combined three-dimensional electric and seismic tomography study on the Åknes rockslide in western Norway: Journal of Applied Geophysics, **70**, 292–306.

Heincke, B., H. Maurer, A. G. Green, H. Willenberg, T. Spillmann, and L. Burlini, 2006, Characterizing an unstable mountain slope using shallow 2D and 3D seismic tomography: Geophysics, **71**, no. 6, B241–B256.

Henley, D. C., 1999, The radial trace transform: an effective domain for coherent noise attenuation and wave field separation: 69th Annual International Meeting, SEG, Expanded Abstracts, 1204–1207.

Hu, L. Z., and G. A. McMechan, 1987, Wave-field transformations of vertical seismic profiles: Geophysics, **52**, 307–321.

Hunter, J. A., S. E. Pullan, R. A. Burns, R. M. Gagne, and R. L. Good, 1984, Shallow seismic reflection mapping of the overburden-bedrock interface with the engineering seismograph—some simple techniques: Geophysics, **49**, 1381–1385.

Israil, M., and A. K. Pachauri, 2003, Geophysical characterization of a landslide site in the Himalayan foothill region: Journal of Asian Earth Sciences, **22**, 253–263.

Jongmans, D., G. Bièvre, F. Renalier, S. Schwartz, N. Beaurez, and Y. Orengo, 2009, Geophysical investigation of a large landslide in glaciolacustrine clays in the Trièves area (French Alps): Engineering Geology, **109**, 45–56.

Jongmans, D., and S. Garambois, 2007, Geophysical investigation of landslides: a review: Bulletin de la Société géologique de France, **178**, 101–112.

Juhlin, C., H. Palm, C. Müllern, and B. Wållberg, 2002, Imaging of groundwater resources in glacial deposits using high-resolution reflection seismics, Sweden: Journal of Applied Geophysics, **51**, 107–120.

Kearey, P., M. Brooks, and I. Hill, 2002, An introduction to geophysical exploration: Blackwell Publishing.

Kennett, P., R. L. Ireson, and P. J. Conn, 1980, Vertical seismic profiles: their applications in exploration geophysics: Geophysical Prospecting, **28**, 676–699.

Kissling, E., W. L. Ellsworth, D. Eberhart-Phillips, and U. Kradolfer, 1994, Initial reference models in local earthquake tomography: Journal of Geophysical Research, **99**, 19635–19646.

Klassen, R. W., 1989, Quaternary geology of the southern Interior Plains, *in* R. J. Fulton, ed., Quaternary geology of Canada and Greenland: Geological Survey of Canada, Geology of Canada, **1**, 138–174.

Knight, R. J., and A. L. Endres, 2005, An introduction to rock physics principles for near-surface geophysics, *in* D. K. Butler, ed., Near-surface geophysics, Investigations in Geophysics, **13**: Society of Exploration Geophysicists, 31–70.

Lankston, R. W., 1989, The seismic refraction method: a viable tool for mapping shallow targets into the 1990s: Geophysics, **54**, 1535–1542.

Lapenna, V., P. Lorenzo., A. Perrone, S. Piscitelli, E. Rizzo, and F. Sdao, 2005, 2D electrical resistivity imaging of some complex landslides in the Lucanian Apennine chain, southern Italy: Geophysics, **70**, no. 3, B11–B18.

Lapenna, V., P. Lorenzo., A. Perrone, S. Piscitelli, F. Sdao, and E. Rizzo, 2003, High-resolution geoelectrical tomographies in the study of Giarrossa landslide (southern Italy): Bulletin of Engineering Geology and the Environment, **62**, 259–268.

Lee, C. -C., C. -H. Yang, H. -C. Liu, K. -L. Wen, Z. -B. Wang, and Y. -J. Chen, 2008, A Study of the hydrogeological environment of the Lishan landslide area using resistivity image profiling and borehole data: Engineering Geology, **98**, 115–125.

Leslie, L. E., and M. M. Fenton, 2001, Quaternary stratigraphy and surficial geology Peace River final report: Alberta Energy and Utilities Board, Special Report SPE-10.

Liu, S., S. Zhang, and J. Li, 2001, Investigation of a landslide in the new site of Badong County by integrated geophysical survey: Science in China Series D: Earth Sciences, **44**, 426–436.

Liverman, D. G. E., N. R. Catto, and N. W. Rutter, 1989, Laurentide glaciation in west-central Alberta: a single (Late Wisconsinan) event: Canadian Journal of Earth Sciences, **26**, 266–274.

Loke, M. H., 2010, Tutorial: 2D and 3D electrical imaging surveys: Geotomo Software, Malaysia. http://www.geoelectrical.com/ accessed May 1, 2010.

Loke, M. H., and R. D. Barker, 1996, Rapid least-squares inversion of apparent resistivity pseudosections by a quasi-Newton method: Geophysical Prospecting, **44**, 131–152.

Lowrie, W., 1997, Fundamentals of geophysics: Cambridge University Press.

Lykousis, V., D. Sakellariou, and J. Locat, eds., 2007, Submarine mass movements and their consequences: Proceedings of the 3rd International Conference, Santorini, Advances in Natural and Technological Hazards Research, **27**, Springer.

Marfurt, K. J., R. V. Schneider, and M. C. Mueller, 1996, Pitfalls of using conventional and discrete Radon transforms on poorly sampled data: Geophysics, **61**, 1467–1482.

Mathews, W. H., 1980, Retreat of the last ice sheets in northeastern British Columbia and adjacent Alberta: Geological Survey of Canada Bulletin, **331**.

McCann, D. M., and A. Forster, 1990, Reconnaissance geophysical methods in landslide Investigations: Engineering Geology, **29**, 59-78.

McConnell, R. G. and R. W. Brock, 2003, Report on the great landslide at Frank, Alta., 1903: Edmonton Geological Society.

Meric, O., S. Garambois, D. Jongmans, M. Wathelet, J. L Chatelain, and J. M. Vengeon, 2005, Application of geophysical methods for the investigation of the large gravitational mass movement of Séchilienne, France: Canadian Geotechnical Journal, **42**, 1105–1115.

Meric, O., S. Garambois, J. -P. Malet, H. Cadet, P. Gueguen, and D. Jongmans, 2007, Seismic noise-based methods for soft-rock landslide characterization: Bulletin de la Société géologique de France, **178**, 137–148.

Miller, B. G. N., and D. M. Cruden, 2002, The Eureka River landslide and dam, Peace River Lowlands, Alberta: Canadian Geotechnical Journal, **39**, 863–878.

Miller, R. D., and D. W. Steeples, 1994, Applications of shallow high-resolution seismic reflection to various environmental problems: Journal of Applied Geophysics, **31**, 65–72.

Moon, W., A. Carswell, R. Tang, and C. Dilliston, 1986, Radon transform wave field separation for vertical seismic profiling data: Geophysics, **51**, 940–947.

Moreno, F., and C. Froese, 2006, Turtle Mountain field laboratory monitoring and research summary report, 2005: Alberta Energy and Utilities Board, EUB/AGS Earth Sciences Report 2006-07.

Morgan, A. J., R. C. Paulen, and C. R. Froese, 2008, Ancestral buried valleys of the Peace River: Effects on the town of Peace River: Proceedings of the 61st Canadian Geotechnical Conference, Edmonton, Alberta, 1219–1226.

Morgan, A. J., S. R. Slattery, and C. R. Froese, 2009, Results of sediment coring at the Town of Peace River, northwestern Alberta: Alberta Energy and Utilities Board, ERCB/AGS Open File Report 2009-18. http://www.ags.gov.ab.ca/publications/abstracts/OFR_2009_18.html

Narwold, C. F., and W. P. Owen, 2002, Seismic refraction analysis of landslides: Proceedings of the 2nd annual conference on the application of geophysical and NDT methodologies to transportation facilities and infrastructure, FHWA-WRC-02-001.

Naudet, V., M. Lazzari, A. Perrone, A. Loperte, S. Piscitelli, and V. Lapenna, 2008, Integrated geophysical and geomorphological approach to investigate the snowmelt-triggered landslide of Bosco Piccolo village (Basilicata, southern Italy): Engineering Geology, **98**, 156–167.

Novosad, S., P. Blaha, and J. Kneijzlik, 1977, Geoacoustic methods in slope stability investigations: Bulletin of Engineering Geology and the Environment, **16**, 229–231.

Ogunsuyi, F. O., and D. R. Schmitt, in press 2010, Integrating seismic velocity tomograms and seismic imaging: application to the study of a glacially buried valley, *in* R. Miller, J. Bradford, and K. Holliger, eds., Near surface seismology and ground penetrating radar: Society Exploration Geophysicists.

Oldenborger, G. A., P. S. Routh, and M. D. Knoll, 2005, Sensitivity of electrical resistivity tomography data to electrode position errors: Geophysical Journal International, **163**, 1–9.

Oristaglio, M. L., 1985, A guide to current uses of vertical seismic profiles: Geophysics, **50**, 2473–2479.

Palmer, D., 1981, An introduction to the generalized reciprocal method of seismic refraction interpretation: Geophysics, **46**, 1508–1518.

Park, S. -G., and J. -H. Kim, 2005, Geological survey by electrical resistivity prospecting in landslide area: Geosystem Engineering, **8**, 35-42.

Parker, R. L., 1984, The inverse problem of resistivity sounding: Geophysics, **49**, 2143–2158.

Paulen, R. C., 2004, Surficial geology of the Grimshaw area (NTS 84C/SW): Alberta Energy and Utilities Board, EUB/AGS Map 291, scale 1:100000.

Pelton, J. R., 2005, Near-surface seismology: surface-based methods, *in* D.K. Butler, ed., Near-surface geophysics, Investigations in Geophysics, **13**: Society of Exploration Geophysicists, 219–263.

Pettapiece, W. W., 1986, Physiographic subdivisions of Alberta: Land Resource Research Centre, Research Branch, Agriculture Canada, scale 1:1500000.

Pullammanappallil, S. K., and J. N. Louie, 1994, A generalized simulated-annealing optimization for inversion of first-arrival times: Bulletin of the Seismological Society of America, **84**, 1397–1409.

Roch, K. -H., W. Chwatal, and E. Brückl, 2006, Potentials of monitoring rock fall hazards by GPR: considering as example the results of Salzburg: Landslides, **3**, 87–94.

Ronen, J., and J. F. Claerbout, 1985, Surface-consistent residual statics estimation by stack-power maximization: Geophysics, **50,** 2759–2767.

Sass, O., R. Bell, and T. Glade, 2008, Comparison of GPR, 2D-resistivity and traditional techniques for the subsurface exploration of the Öschingen landslide, Swabian Alb (Germany): Geomorphology**, 93**, 89–103.

Schmitt, D. R., B. Milkereit, T. Karp, C. Scholz, S. Danuor, D. Meillieux, and M. Welz, 2007, In situ seismic measurements in borehole LB-08A in the Bosumtwi impact structure, Ghana: preliminary interpretation: Meteoritics and Planetary Science, **42**, 755–768.

Schmutz, M., Y. Albouy, R. Guérin, O. Maquaire, J. Vassal, J. -J. Schott, and M. Descloîtres, 2000, Joint electrical and time domain electromagnetism (TDEM) data inversion applied to the Super Sauze earthflow (France): Surveys in Geophysics, **21**, 371–390.

Sloan, S. D., D. W. Steeples, and P. E. Malin, 2008, Acquisition and processing pitfall associated with clipping near-surface seismic reflection traces: Geophysics, **73**, no. 1, W1–W5.

Socco, L. V., D. Jongmans, D. Boiero, S. Stocco, M. Maraschini, K. Tokeshi, and D. Hantz, 2010, Geophysical investigation of the Sandalp rock avalanche deposits: Journal of Applied Geophysics, **70**, 277–291.

Spitzer, R., F. O. Nitsche, and A. G. Green, 2001, Reducing source-generated noise in shallow seismic data using linear and hyperbolic τ–p transformations: Geophysics, **66**, 1612–1621.

Spitzer, R., F. O. Nitsche, A. G. Green, and H. Horstmeyer, 2003, Efficient acquisition, processing and interpretation strategy for shallow 3D seismic surveying: a case study: Geophysics, **68**, 1792 –1806.

Steeples, D. W., 1998, Shallow seismic reflection section—Introduction: Geophysics, **63**, 1210-1212.

Steeples, D. W., and R. D. Miller, 1990, Seismic reflection methods applied to engineering, environmental, and groundwater problems, *in* S. H. Ward, ed., Geotechnical and Environmental Geophysics 1: Society of Exploration Geophysicists, 1–30.

Steeples, D. W., and R. D. Miller, 1998, Avoiding pitfalls in shallow seismic reflection surveys: Geophysics, **63**, 1213–1224.

Stefani, J. P., 1995, Turning-ray tomography: Geophysics, **60**, 1917–1929.

Stewart, R. R., 1985, Median filtering: review and a new f/k analogue design: Journal of the Canadian Society of Exploration Geophysicists, **21**, 54 –63.

Stucchi, E., and A. Mazzotti, 2009, 2D seismic exploration of the Ancona landslide (Adriatic Coast, Italy): Geophysics, **74**, no. 5, B139–B151.

Taner, M. T., and F. Koehler, 1969, Velocity spectra—digital computer derivation and applications of velocity functions: Geophysics, **34**, 859–881.

Taner, M. T., F. Koehler, and K. A. Alhilali, 1974, Estimation and correction of near-surface anomalies: Geophysics, **39**, 441–463.

Theune, U., D. Rokosh, M. D. Sacchi, and D. R. Schmitt, 2006, Mapping fractures with GPR: a case study from Turtle Mountain: Geophysics, **71**, no. 5, B139–B150.

Theune, U., M. D. Sacchi, and D. R. Schmitt, 2005, Least-squares local Radon transforms for dip-dependent GPR image decomposition: Journal of Applied Geophysics, **59**, 224–235.

Tingey, B. E., J. H. McBride, T. J. Thompson, W. J. Stephenson, J. V. South, and M. Bushman, 2007, Study of a prehistoric landslide using seismic reflection methods integrated with geological data in the Wasatch Mountains, Utah, USA: Engineering Geology, **95**, 1–29.

Toshioka, T., T. Tsuchida, and K. Sasahara, 1995, Application of GPR to detecting and mapping cracks in rock slopes: Journal of Applied Geophysics, **33**, 119–124.

Van der Hilst R. D., and W. Spakman, 1989, Importance of the reference model in linearized tomography and images of subduction below the Caribbean plate: Geophysical Research Letters, **16**, 1093–1096.

Varnes, D. J., 1978, Slope movement types and processes, *in* R. L. Schuster and R. J. Krizek, eds., Landslides—Analysis and Control: Transportation Research Board, National Academy of Sciences, Washington, D.C., Special Report, **176**, 11–33. Citation: Figure 2-1 (inserted in pocket in back of book; gives complete classification with drawings and explanatory text).

Vidale, J. E., 1988, Finite difference calculation of travel times: Bulletin of the Seismological Society of America, **78**, 2062–2076.

Voight, B., ed., 1978, Rockslides and avalanches 1, Natural phenomena: Developments in Geotechnical Engineering, **14A**, Elsevier.

Wehr, A., and U. Lohr, 1999, Airborne laser scanning – an introduction and overview: ISPRS Journal of Photogrammetry and Remote Sensing, **54**, 68–82.

White, D. J., 1989, Two-dimensional seismic refraction tomography: Geophysical Journal, **97**, 223–245.

Widess, M. B., 1973, How thin is a thin bed?: Geophysics, **38**, 1176–1180.

Wieczorek, G. F., M. C. Larsen, L. S. Eaton, B. A. Morgan, and J. L. Blair, 2001, Debris-flow and flooding hazards associated with the December 1999 storm in coastal Venezuela and strategies for mitigation: U.S. Geological Survey Open-File Report 01-0144. http://pubs.usgs.gov/of/2001/ofr-01-0144/ accessed September 8, 2009.

Worthington, P. F., 1977, Geophysical investigations of groundwater resources in the Kalahari basin: Geophysics, **42**, 838–849.

Yilmaz, Ö., 2001, Seismic data analysis: processing, inversion, and interpretation of seismic data (Investigations in Geophysics, no. 10): Society of Exploration Geophysicists.

Zelt C. A., A. Azaria, and A. Levander, 2006, 3D seismic refraction traveltime tomography at a groundwater contamination site: Geophysics, **71**, no. 5, H67–H78.

Zelt, C. A., and R. B. Smith, 1992, Seismic traveltime inversion for 2-D crustal velocity structure: Geophysical Journal International, **108**, 16–34.

Zonge, K., J. Wynn, and S. Urquhart, 2005, Resistivity, induced polarization, and complex resistivity, *in* D. K. Butler, ed., Near-surface geophysics, Investigations in Geophysics, **13**: Society of Exploration Geophysicists, 265–300.

Appendix

A version of the invited paper on the subject of a buried valley that is in press with Society of Exploration Geophysicists for publication in an upcoming book:

Title: Advances in Near-Surface Seismology and Ground-Penetrating Radar
Editors: R. Miller, J. Bradford, and K. Holliger
Year: 2010
Publishers: Society Exploration Geophysicists
http://segdl.org/ebooks/

Integrating Seismic Velocity Tomograms and Seismic Imaging: Application to the Study of a Buried Valley

Femi O. Ogunsuyi and Douglas R. Schmitt

Abstract

The architectural complexity of a ~350 m deep paleovalley was revealed in a previous investigation by means of the acquisition and conventional processing of a high resolution seismic reflection survey in northern Alberta, Canada. However, much of the original raw data quality, particularly with respect to near surface features such as commercial methane deposits, was substantially degraded relative to the original raw data. This motivated use of additional processing algorithms to improve the quality of the final image that includes the development of a velocity model via tomographic inversion as input to prestack depth migration (PSDM), the application of a variety of noise suppression techniques, and time-variant bandpass filtering. The quality of the PSDM image was poorer in comparison to the newly processed time reflection profile, emphasizing the importance of a good velocity function for migration. In spite of

this, the tomographic velocity model highlights the ability to distinguish the materials constituting the paleovalley from the other surrounding rock bodies. Likewise, the seismic reflection data reprocessing was able to enhance both the spatial and vertical resolution of the reflection data and also provide a better imaging of new shallow features that indicate presence of gas, previously not observed in the conventionally processed section. Consequently, we underscore the importance of ensuring high frequency signals are predominantly kept during the processing of near-surface reflection data and experimenting with different noise suppression procedures before resorting to total muting of the seismic noise cone.

Introduction

Buried valleys are, simply, exactly what their name suggests: valleys that have been filled with unconsolidated sediments and covered such that their existence is not apparent at the earth's surface. They are abundant in recently glaciated areas in North America and Europe (e.g., Fisher et al., 2005; Hooke and Jennings, 2006; Jørgensen and Sandersen, 2008; ÓCofaigh, 1996). Their internal structure is complex with a heterogeneous mix of fluid-saturated porous and permeable sands and gravels mixed with low porosity and permeability diamicts and clays.

Surficial geological mapping often cannot locate nor delineate the dimensions of these buried valleys because they are mostly masked at the surface by recent glacial sediments; and the use of invasive methods like boreholes has been employed in characterizing them (e.g., Andriashek and Atkinson, 2007). Moreover, the physical properties of these glacially derived sediments often differ significantly from the surrounding bedrock that valleys had been cut into; and this contrast allows a number of complementary geophysical methods to be used. Geophysical techniques can also provide laterally continuous information about the subsurface, and so they may be preferred over the intrusive methods.

Geophysical methods have been used widely to investigate near-surface targets (Hunter et al., 1984; Miller et al., 1989; Clague et al., 1991; Belfer et al.,

1998; Nitsche et al., 2002; Benjumea et al., 2003; Sharpe et al., 2004; Chambers et al., 2006), and specifically, buried valleys (Greenhouse and Karrow, 1994; Jørgensen et al., 2003a; Jørgensen et al., 2003b; Steuer et al., 2009). In particular, refraction and reflection seismic methods have been used extensively in different glacial environments to image subsurface structures (e.g., Roberts et al., 1992; Wiederhold et al., 1998; Büker et al., 2000; Juhlin et al., 2002; Schijns et al., 2009) and also to study buried valleys (Büker et al., 1998; Francese et al., 2002; Fradelizio et al., 2008). Mostly in these studies, the application of seismic inversion is oftentimes limited to first-arrival traveltimes as input (e.g., Lennox and Carlson, 1967; Deen and Gohl, 2002; Zelt et al., 2006), as opposed to the use of both refracted and reflected traveltimes (e.g., De Iaco et al. 2003).

The fresh ground water within these valleys is the most important resource. Consequently, in the last 15 years there have been numerous and varied geophysical investigations in Northern Europe (e.g., Sandersen and Jørgensen, 2003; Gabriel et al., 2003; Wiederhold et al., 2008; Auken et al., 2009) and North America (e.g., Sharpe et al., 2003; Pullan et al., 2004; Pugin et al., 2009) to locate and define such features for their exploitation and protection. Further, the porous sands and gravels within buried valleys can also contain local biogenic gas as shown by Pugin et al., 2004 or leaked thermogenic methane. Such gas sometimes exists in modest commercial quantities but it can also be a significant safety hazard for drillers.

Ahmad et al. (2009) recently described an integrated geological, well log, DC electrical, and seismic reflection study of one such large buried valley in northern Alberta, Canada. Using the same seismic dataset, this contribution extends that work by exploring the development of a seismic tomographic velocity model using traveltime inversion techniques of both refracted and reflected waves over and above the simple refraction analysis performed by the authors to characterize the paleovalley on the basis of the material velocities.

Refracted, guided, air, and surface waves are examples of source-generated noise (coherent noise) that presents considerable problem during seismic data processing (Büker et al., 1998; Montagne and Vasconcelos, 2006).

Separation of refracted and guided waves from shallow reflections, with certainty, is difficult to achieve and these linear events can stack coherently on reflection profiles causing misinterpretation (Steeples and Miller, 1998). Performing a noise cone muting may prove useful in eliminating some of the source-generated noise; however, reflections are also muted in the process (Baker et al., 1998). Surgical noise cone muting was employed in removing the coherent noise in the previous study (Ahmad, 2006; Ahmad et al., 2009). Apart from the possibility that this may not have removed the guided waves located outside the noise cone zone on the shot gathers, it may also have inadvertently eliminated some true reflections during muting; either way, the resulting seismic profile is not as satisfactory as one might expect from the quality of the raw shot gathers. Therefore, in this study, we instead performed radial and slant-stack noise suppression procedures on the dataset in order to retain and enhance those shallow reflections that may have been removed by muting or masked by source-generated noise.

Since the dominant frequency of a seismic wave controls the separation of two close events (Yilmaz, 2001), the new processing scheme was also aimed at improving the spatial and vertical resolution of the dataset due to the fact that the seismic processing sequence of the previous study did not account for adequate filtering-out of low frequencies. We subsequently attempted to use the tomographic velocity model to perform a prestack depth migration (PSDM) after the noise suppression strategies on the dataset. To our knowledge, the application of the PSDM algorithms and the radial and τ-p noise suppression techniques, often employed in more conventional and deeper petroleum exploration, have not been applied to such near surface seismic data.

The goal here is not to provide a new geological interpretation of Ahmad et al.'s (2009) study, but to share the experiences gained in applying a number of tools, some of which have heretofore only been employed to our knowledge in deeper petroleum exploration. One especial improvement over the earlier work is that this reprocessing has allowed for the imaging of shallow methane deposits within the glacial materials, and as such this work has implications to both the exploration of such resources and to enhanced safety for drillers.

Background

Details and maps of the location of the survey in the northwestern corner of Alberta and roughly centered at 58^0 35' N and 118^0 31' W are found in Ahmad et al. (2009). The near surface geology of the northeast British Columbia and northwest Alberta has been extensively studied over the last decade (e.g., Levson, 2008; Hickin et al. 2008; Best et al., 2006). The surficial geology area immediately over the profile has been investigated by Plouffe et al. (2004) and Paulen et al. (2005) and it is established to be primarily blanketed with various glacial, lacustrine, and glacio-lacustrine sediments of variable depths; these authors have also produced numerous complementary surficial geological maps of the region generally.

A brief explanation of the bedrock geology is necessary to assist with the understanding of the later geophysical responses. The consolidated bedrock sediments beneath the Quaternary cover in the region are nearly flat-lying, and when not disturbed consist of ~250 m of Cretaceous siliclastic sands and shales underlain, across a sharp unconformity (sub-Cretaceous), by more indurated Paleozoic carbonates and shales. More detailed descriptions of the bedrock geology can be found in Hickin et al. (2008) and references therein. Ahmad et al. (2009), too, provide representative well logs that to first order approximately categorize the sediments on the basis of sonic velocity and density.

Seismic Field Program

A high-resolution 2D seismic profile was acquired over a survey length of approximately 9.6 km in east-west direction (see Figure A.1). The seismic survey line straddles the surface over the large buried valley to the east and the out-of-valley region to the west as determined from the maps of bedrock topography and surficial geology (Paulen et al., 2005; Pawlowicz et al., 2005a; b; Plouffe et al., 2004) (Figure A.1). The purpose of the survey was to image the formation above the sub-Cretaceous unconformity and hence delineate the buried channel and obtain important information about its internal structure.

A summary of the acquisition parameters is reviewed in Table A.1. The P-wave seismic source used was the University of Alberta's IVI Minivib™ unit, operated with linear sweeps of 7 s period from 20 Hz to 250 Hz at a force of about 26690 Newtons (6000 pounds). The seismic traces were acquired with high frequency (40-Hz) geophone singles (to attenuate some of the ground roll noise) at a 4 m spacing using 240-channel semi-distributed seismograph that consists of ten 24-channel Geode™ field boxes connected via field intranet cables to the recording computer. About 5 - 8 sweeps per shotpoint were generated by the seismic source at 24 m spacing. Cross-correlation of the seismic traces with the sweep signal (to generate a spike source) as well as the vertical stacking was carried out in the field and the final stacked records were saved in SEG2 format and later combined with survey header information into a single SEGY format file for processing.

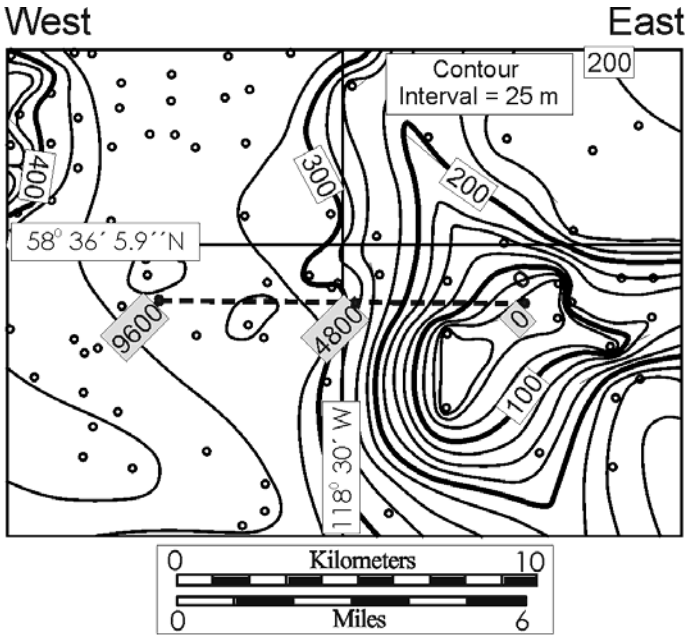

Figure A.1. Bedrock topography elevation contours in meters above sea level (a.s.l.) modified from Pawlowicz et al. (2005a) with the location of the 2D survey line shown as broken line with black labels inside gray boxes indicating distance in meters from east to west with origin at 0 m. The small unfilled circles are wellbore locations used to generate the bedrock topography map.

Table A.1. Acquisition parameters for the 2D seismic survey.

Parameter	Value
2D line direction	East-West
Length of profile	~ 9.6 km
Source	6000-lb IVI Minivib™ unit
Source frequency	20-250 Hz
Source type	Linear
Source length	7 s
Source spacing	24 m
Vertical stacks	5-8
Number of unique shotpoints	399
Receivers	40-Hz single geophones
Receiver spacing	4 m
Recording instrument	Geometrics Geode™ system
Number of channels	192-240
Sampling interval	0.5 ms
Record length	1.19 s
Nominal fold	~ 40

Generally, good coupling between the vibrator plate and the frozen, snow-covered ground was achieved as determined by the constant nature of the force over time during the sweep period and the transmission of high seismic frequencies (Ahmad et al., 2009). In a like manner, there was good coupling between the ground and the geophones, which were frozen in place overnight, thus improving the signal-to-noise (S/N) ratio. The average CMP fold for the survey was about 40. Two representative shot gathers from either ends of the seismic profile (Figure A.2) highlight the evolution of the traveltimes (and hence velocity structure) from east to west.

Seismic Traveltime Inversion

A linearized traveltime inversion procedure, primarily developed for modeling 2-D crustal refraction and wide-angle data (comprehensively described in Zelt and Smith, 1992; and applied in Song and ten Brink, 2004), was utilized. The inversion incorporates traveltimes of the direct, refracted, and reflected events. The geometry of the model is outlined by boundary node points that are connected through linear interpolation while the velocity field is specified by velocity value points at the top and base of each layer. The velocity within each block varies linearly with depth (between the upper and lower velocity in a layer) and also laterally across the velocity points along the upper and lower layer boundaries.

Examination of the refracted events on the shot gathers offers an important insight into the apparent velocity structure of the survey line. Figure A.2a shows a shot gather acquired at the east end of the profile immediately over the buried valley. Performing a simple intercept-time refraction analysis on this gather suggests a simple 2-layer model could be sufficient (see Ahmad et al., 2009). The wave passage through the top layer (grey highlight) may be linked to a lower material velocity of the Quaternary fill as compared to the higher velocity of the Devonian carbonates (yellow highlight). The velocity of the Quaternary rock is expected to be much lower than that of the Paleozoic because of its weak consolidation due to minimal overburden pressures. On the other hand, the shot gather obtained at the west end and outside of the buried valley indicates three layers (Figure A.2b). There is a direct wave (grey highlight) which passes through a thin low velocity Quaternary rock, a refracted event from the top of the Cretaceous rock of intermediate velocities and another wave refracted from the top of the Paleozoic with higher velocities.

The Vista® processing package (GEDCO, Calgary) was used to pick the traveltimes within the shot gathers of both refracted and reflected arrivals. About 72,000 traveltime picks were made from 143 shot gathers, and these were assigned an average error of ± 5 ms to account for far-offset ranges and deep

depths (Ogunsuyi et al., 2009). The program RayGUI (Song and ten Brink, 2004) was utilized for the forward modelling and inversion.

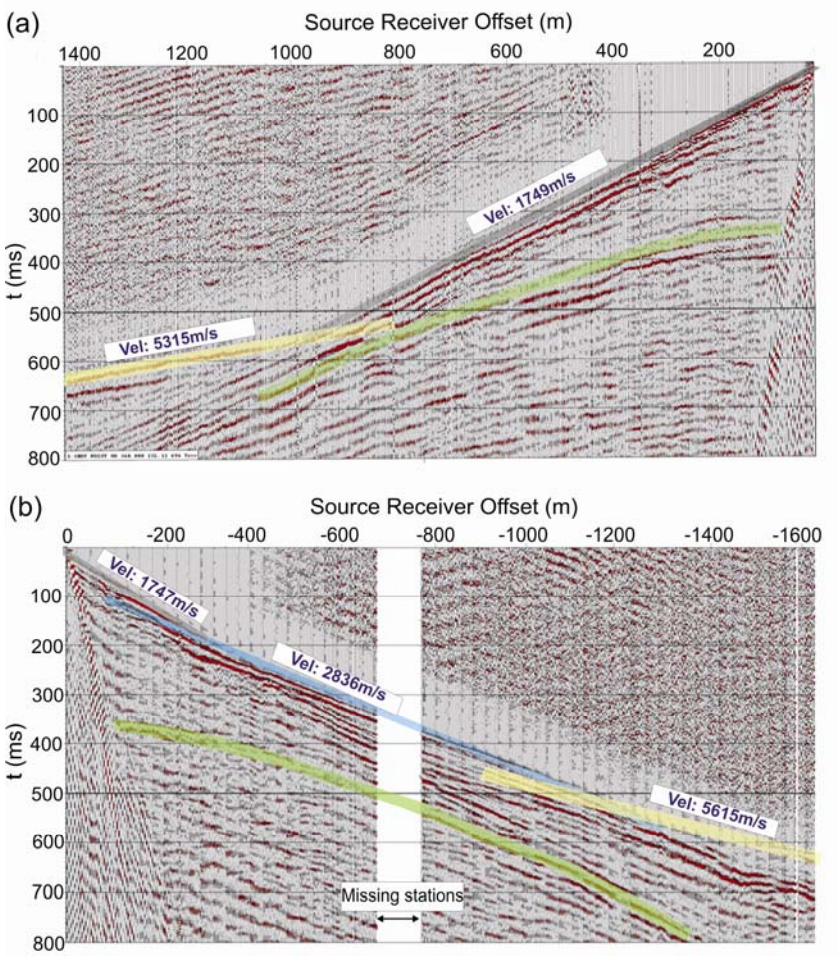

Figure A.2. Raw shot gathers acquired at different locations on the survey line. The apparent velocities of different refractors as obtained from a simple intercept-time refraction method are displayed. Positive offset values are to the west of the respective shotpoint while negative offsets are to the east. The gray highlight shows direct wave through the Quaternary fill, blue highlight is refracted wave turning through the Cretaceous rock, yellow line denotes the refracted wave through the Devonian and the reflection from the Devonian top is in green color. (a) An eastern shot gather (shotpoint 360) acquired over the valley on the seismic line. (b) A western shot record (shotpoint 1848) outside the buried valley.

After series of tests to determine the optimal initial model, the chosen starting model was constructed with 6 layers, with the velocities varying linearly in each layer. The starting model was made up of coinciding locations of velocity and boundary nodes which were almost equally spaced laterally at a distance of about 330 m for the top of the second and third layers, and irregularly spaced for the other layers. Short-offset (< 100 m) direct arrivals were inverted in the first layer to account for the near-surface velocity variations and the relatively flat surface topography. The second layer was defined for the inversion of the rest of the direct waves (grey highlights in Figure A.2), which constituted the greater part of the seismic waves through the Quaternary deposits. The third layer was defined for the refracted events turning through the Cretaceous rock (i.e. blue highlight in Figure A.2b), while the base of the fourth layer represented the waves prominently reflected from the top of the sub-Cretaceous unconformity. Technically, the third and fourth layers are supposed to be one and the same; however, they were separated to give a measure of the validity of the final tomographic model, as demonstrated by the degree to which the gap (depth-wise) between the base of the third layer and base of the fourth layer will be reduced subsequent to the inversion process. The refracted events (yellow highlights in Figure A.2) through the Devonian rock were inverted for in the fifth layer. A reflected event, which could not be picked successfully for the whole length of the survey line, was inverted for layer six and so less confidence is placed on the tomographic results at elevations below ~ -200 m above sea level.

The model was inverted layer by layer from the top-down in a layer-stripping method to speed up and simplify the process (Zelt and Smith, 1992). This method involved the following steps: (1) inversion of the model parameters (both velocity and boundary nodes) of the topmost layer simultaneously; (2) updating the model with the calculated changes; (3) repeating steps (1) and (2) till the stopping criteria is satisfied for the layer; (4) holding the model parameters of the layer constant for the subsequent inversion of all the parameters of the next layer in line; and (5) repeating steps (1) to (4) for all the other underlying layers

sequentially. The uncertainties in the depths of the boundary nodes and velocity values were 10 m and 200 m/s respectively.

The average values for the root-mean-square (rms) traveltime residual between the calculated and the observed times for all layer was 16.4 ms after 7 iterations. It should be noted that adding more model parameters generally reduces the traveltime residual, but at the expense of also reducing the spatial resolution of the final model parameters (Zelt and Smith, 1992). Subsequent to the inversion, the difference in depth between the base of the third and fourth layers was acceptably reduced on the west but not adequately on the east end inside the valley area. Merging the third and fourth layer before the inversion scheme however, produced low ray coverage, thus violating one of the conditions for choosing a final model. Consequently, the six-layer model was chosen as the optimum model for the subsurface of the area under investigation.

Seismic Reflection Data Processing

The earlier study (Ahmad et al., 2009) involves a conventional 2D CMP processing scheme (Table A.2) while the new processing sequence (adapted from Spitzer et al., 2003) carried out in this study is complemented with some noise suppression procedures involving transformation of *t-x* data into other domains (Table A.3). The motivation for designing a new processing scheme for the seismic data is the need to determine if reflections were eliminated or degraded by the muting functions adapted in the previous study or covered up by source-generated noise, and if so, recover the affected reflections; and additionally improve the lateral and vertical resolution of the reflection profile.

Low quality traces resulting from noisy channels, high amplitude, and frequency spikes are problematic to a final image. Starting with the dataset that already has geometry information assigned, the bad traces, with abnormally high amplitudes and frequencies were identified by computing amplitude and frequency statistics on all the traces and subsequently removed. To adjust for the lateral changes in the thickness and velocity of the shallow depths and also the small elevation variations of sources and receivers, elevation/refraction statics

corrections was conducted. A model of the shallow subsurface was established by inverting the first-break picks. Utilizing a weathering velocity of 500 m/s, the average velocity of the first refractor was approximately 1700 m/s. The computed statics corrections were applied to a flat datum of 385 m above sea level, which was slightly above the highest elevation of the survey line. Total elevation/refraction statics corrections ranged from about -6.5 ms to +21 ms.

Table A.2. Previous seismic processing sequence of Ahmad et al., (2009).

Processing Step	Parameters
Geometry	
Editing of bad trace	
Offset limited sorting	-500 m to -12 m and 12 m to 500 m
Surgical mute	Auto bottom mute; manual surgical mute
CMP sorting	4 m bin size
Velocity analyses	
NMO corrections	15% stretch mute
Elevation/refraction statics corrections	400 m a.s.l. datum; 1500 m/s replacement velocity
Residual statics corrections	Stack power algorithm
Inverse NMO corrections	
Final velocity analyses	
NMO corrections	15% stretch mute
Final residual statics corrections	Stack power algorithm
CMP Stack	
Bandpass filtering	45 to 240 Hz
Mean scaling	
FX Prediction	
AGC	

Table A.3. Time processing sequence for the 2D seismic survey.

Processing Step	Justification
Trace editing	Removal of spurious traces
First-break picking	
Elevation/refraction statics corrections	Correction for shallow lateral variations
Spiking deconvolution	Compression of wavelet
Time-variant bandpass filtering	Suppression of low-frequency noise
Trace equalization	
CMP binning	
Initial velocity analyses	Determination of stacking velocities
NMO corrections	
Residual statics corrections	Correction for near-surface velocity changes
Inverse NMO corrections	
Radial domain processing	Removal of guided waves
Linear τ–p processing	Suppression of source-generated noise
Predictive deconvolution	Elimination of multiples
Dip-moveout (DMO) corrections	Preservation of conflicting dips
Final velocity analyses	Determination of stacking velocities
Final residual statics corrections	Correction for near-surface velocity changes
NMO corrections	
CMP Stack	
F-X prediction	Reduction of incoherent noise
2D Kirchhoff time migration	Placing reflections in their true positions

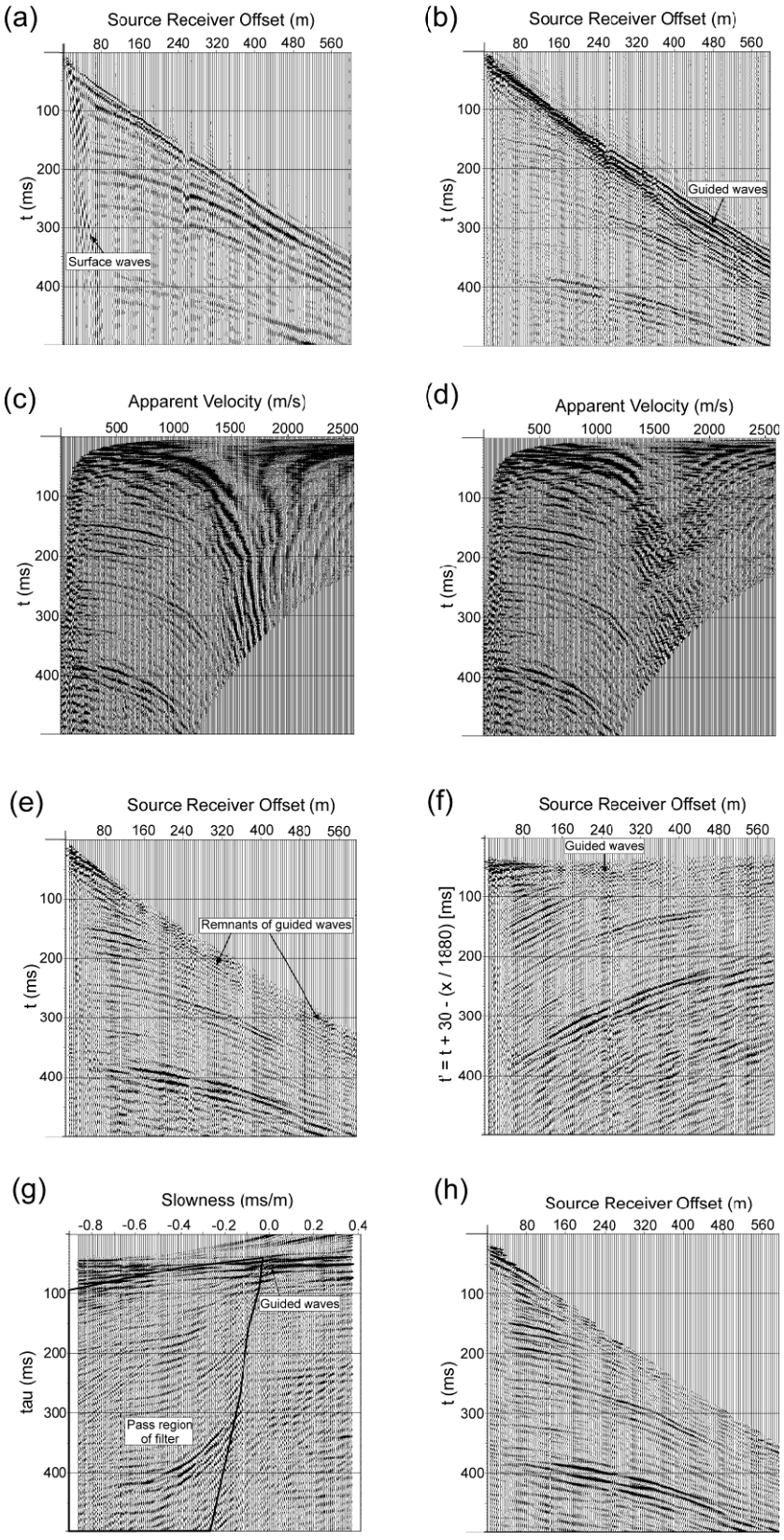

Figure A.3. Figure caption on next page

Figure A.3. (a) A typical raw shot gather (shotpoint number 660) after elevation/refraction static corrections. (b) Same shot gather as (a) after spiking deconvolution, time-variant bandpass filtering and trace equalization. (c) As for (b) after transformation to *r-t* domain. (d) As for (c) after applying a low-cut filter of 45 Hz to suppress the linear events. (e) As for (d) after radial processing which involved transforming the shot gather from *r-t* to *t-x* coordinates. (f) Same shot gather as (e) except that the time axis is reduced traveltimes $t' = t + 30 - (x/1880)$, where 1880 m/s is the average velocity for the first arrival as obtained from intercept-time refraction analyses. (g) As for (f) after linear τ–p transformation. The pass region of the τ–p filter is shown in solid black line. (h) Result of linear τ–p processing obtained from the filtering of (g) and applying inverse τ–p transformation. The records were scaled in relation to the RMS amplitude of their respective gathers.

Predictive deconvolution was not successful in removing some of the multiples in the data at this stage; hence it was carried out in later processing. In order to compress the wavelet to a spike and thus increase the temporal resolution, spiking deconvolution was applied. After testing with different operator lengths for optimal results, 20 ms operator length was finally employed. Low frequencies in the amplitude spectrum of the seismic data were dominated by direct and surface waves, but applying a low-cut frequency filter to the dataset may inadvertently remove some deeper reflections characterized by low frequencies too. Therefore, to avoid this, time-variant bandpass filtering (80-300 Hz for 0-380 ms time interval and 65-150 Hz for 380-800 ms) was applied to the data. Additionally, the bandpass filtering step provides a means by which the temporal resolution of the seismic profile could be enhanced. Following the spiking deconvolution step, the amplitude spectra of the shot gathers were adequately equalized. To appreciate the value of these processing steps, a raw shot gather (shot number 660), affected by surface waves after elevation/refraction statics

corrections (Figure A.3a) and after the application of spiking deconvolution, bandpass filtering and trace equalization (Figure A.3b) are displayed for comparison. Although most of the source-generated noise has not been eliminated, much of the surface waves have been suppressed and the reflections made sharper. Moreover, this processing step appears to have exposed additional guided waves that were concealed in the initial shot gather (Figure A.3b). Details about the properties of these common seismic arrivals, which form the basis of our interpretation, could be found in Robertsson et al. (1996) and Yilmaz (2001).

Choosing the best possible CMP bin size is imperative to minimizing spatial aliasing when processing seismic data for moderately to steeply dipping reflections (Spitzer et al., 2003). To determine the maximum CMP bin size b to use (Yilmaz, 2001), we evaluated

$$b \leq \frac{v_{\min}}{4 f_{\max} \sin\theta} \tag{A.1}$$

where v_{min} is the minimum velocity, f_{max} is the maximum frequency and θ is the maximum expected dip of structures. We arrived at a value of 3 m as bin size for our data. Initial velocity analyses, to determine the stacking velocities, were carried out on CMP supergathers by creating a panel of offset sort/stack records, constant velocity stacks and semblance output.

Residual statics corrections are needed to correct for short wavelength changes in the shallow velocity underneath each sources and receivers. Surface consistent residual statics by a stack power maximization algorithm (Ronen and Claerbout, 1985) was estimated from the data after applying normal moveout (NMO) corrections on the basis of the initial velocity analyses. The resulting average time shifts of about 4 ms were subsequently applied to the inverse NMO corrected data.

As was noted earlier, most of the source-generated noise was not eliminated by bandpass filtering. Linear events (e.g. guided waves), which can adversely affect the interpretation of shallow seismic if they are not suppressed, can still be observed (Figure A.3b). Some of these coherent noises can be reduced by mapping the data from normal *t-x* domain into apparent velocity versus two-

way-time (radial or *r-t*) domain. The basis of this noise attenuation process is that linear events in the *t-x* gather transform into a relatively few radial traces with apparent frequencies shifting from the seismic band to sub-seismic frequencies (Henley, 1999). After transformation to *r-t* domain (Figure A.3c), a low-cut filter of 45 Hz was applied to the radial traces (Figure A.3d) to eliminate the coherent noise mapped by *r-t* transform to low frequencies, and the data was subsequently transformed back to *t-x* domain (Figure A.3e). With regards to the removal of some of the guided waves, the improvement of the data passed through radial processing (Figure A.3e) over the original (Figure A.3b) is quite noticeable.

To further reduce the source-generated noise (direct wave, surface waves and remnants of guided waves) in the data, linear τ–p processing was next applied. Linear and hyperbolic events in *t-x* domain are mapped into points and ellipses, respectively, in linear τ–p (or slant-slack) domain during linear τ–p transformation (Yilmaz, 2001). Hence, it is possible to separate these events in slant-slack gathers to facilitate noise suppression. The steps involved in the linear τ–p processing are outlined below (modified from Spitzer et al., 2001).

a) The shot gathers were converted to reduced-traveltime format (linear moveout terms) using velocities derived from intercept-time refraction analyses. To generate the gathers,

$$t' = t + 30 - (x / v_{ave}) \tag{A.2}$$

was applied to each trace, where t' is the reduced-time in ms, t is the original time in ms, x is the source-receiver offset in m and v_{ave} is the average velocity in km/s. Generally, the average velocities change across the survey line. A bulkshift of 30 ms was applied to the data to accommodate possible linear moveout overcorrections. As seen in Figure A.3f, the first arrivals and related source-generated noises have been converted to horizontal or near-horizontal events.

b) Due to the fact that recording direction is not preserved during τ–p mapping (Spitzer et al., 2001), we separated the positive source-receiver offsets from negative offsets before further processing.

c) The reduced-traveltime shot gathers were transformed into linear τ–p domain using a range of p (slowness) values from -0.9 to 0.4 ms/m for positive offsets and -0.4 to 0.9 ms/m for negative offsets to exclude surface waves and other low velocity coherent noise. Although, minor aliasing of the surface waves was observed in the slant-stack gathers (as observed in *f-k* domain) of the data, it does not seem to pose a major problem to our data.

d) The reflected events (i.e. ellipses) in τ–p domain are quite distinguishable from the source generated noises (mapped to points around p = 0 ms/m). We defined a 2D pass filter (as illustrated in Figure A.3g) around the elliptical events for data on each side of the split source-receiver offset and set the amplitudes of the regions outside the area to zero. A 5 ms taper was applied in the τ direction to the data to minimize artifacts.

e) We then performed inverse linear τ–p transformation on the filtered τ–p data. Subsequently, the data for the positive and negative offsets were recombined, and the linear moveout terms and the time bulkshift removed. The results show that most of the linear source-generated noise has been reduced with no adverse effect on the reflections (Figure A.3h).

Some linear events still remain in the data; this could be because spatially aliased events in the *t-x* domain may spread over a range of slowness, including the pass region of the filter, in the τ–p domain (Spitzer et al., 2001). These remnant linear events were carefully removed by surgical muting. Applying predictive deconvolution with 150 ms operator length and prediction distance of 15 ms at this stage appeared to remove some of the multiples at deeper depths.

Stacking velocities are dip-dependent, hence in the case of an intersection between a flat event and a dipping event, one can only choose a stacking velocity in favor of one of these events, not both (Yilmaz, 2001). Dip-moveout (DMO) correction preserves differing dips with dissimilar stacking velocities during stacking. We applied DMO corrections to the normal moveout corrected gathers (using velocities from the initial conventional CMP velocity analyses) and then performed an inverse NMO on the resultant data. Subsequently, a final velocity analyses was carried out on CMP supergathers (made up of 15 adjacent composite

CMPs). The stacking velocities of the τ–p processed and DMO corrected data can be picked with greater assurance in comparison to the data that was not passed through these processing steps. The final stacking velocities from conventional CMP velocity analyses (Figure A.4a) and the corresponding interval velocities after conversion (Figure A.4b) show the lateral variation in the velocities from the buried valley to the Cretaceous bedrock, as does the result of the tomographic inversion (Figure A.4c).

Using statics estimates computed after NMO corrections based on the final stacking velocities, residual statics corrections were again carried out. As a result of NMO correction, a frequency distortion occurs, particularly for shallow events and large offsets (Yilmaz, 2001). A stretch mute of 60% was applied to the data to get around this problem. The data was later stacked and *f-x* prediction performed on the data to reduce incoherent noise (Canales, 1984). For display purposes, an automatic gain control of 300 ms was applied to the final stacked section (Figure A.5a). To place the reflections in the true subsurface positions, 2D Kirchhoff post-stack time migration was also performed on the seismic data (Figure A.5b).

Although it is possible to make an interpretation about the structure of the buried valley from the time stack section, correlation with depth values cannot be made without having a time-depth relationship. We conducted a simple depth-conversion of the seismic section, using average velocities from both tomographic model and conventional CMP velocity analyses, but the results showed a substantial pulling down of a prominent reflector (the sub-Cretaceous unconformity) at the west end of the profile probably due to the considerable lateral variation in velocity. Instead, prestack depth migration (PSDM) processing was performed on the data after the noise suppression procedures (as outlined in Table A.4) by using the velocity distribution derived from the traveltime tomography of refracted and reflected events (Figure A.4c). Though the results from the PSDM procedure showed less than expected quality, the depth to the prominent reflector at the top of the unconformity agrees acceptably with available wellbore information. The resulting PSDM image obtained with split-step (Stoffa et al., 1990) shot-profile (Biondi, 2003) migration algorithm is

displayed on its own (Figure A.5c) and also overlaid with velocity field from traveltime tomography and some interpretation tags (Figure A.5d).

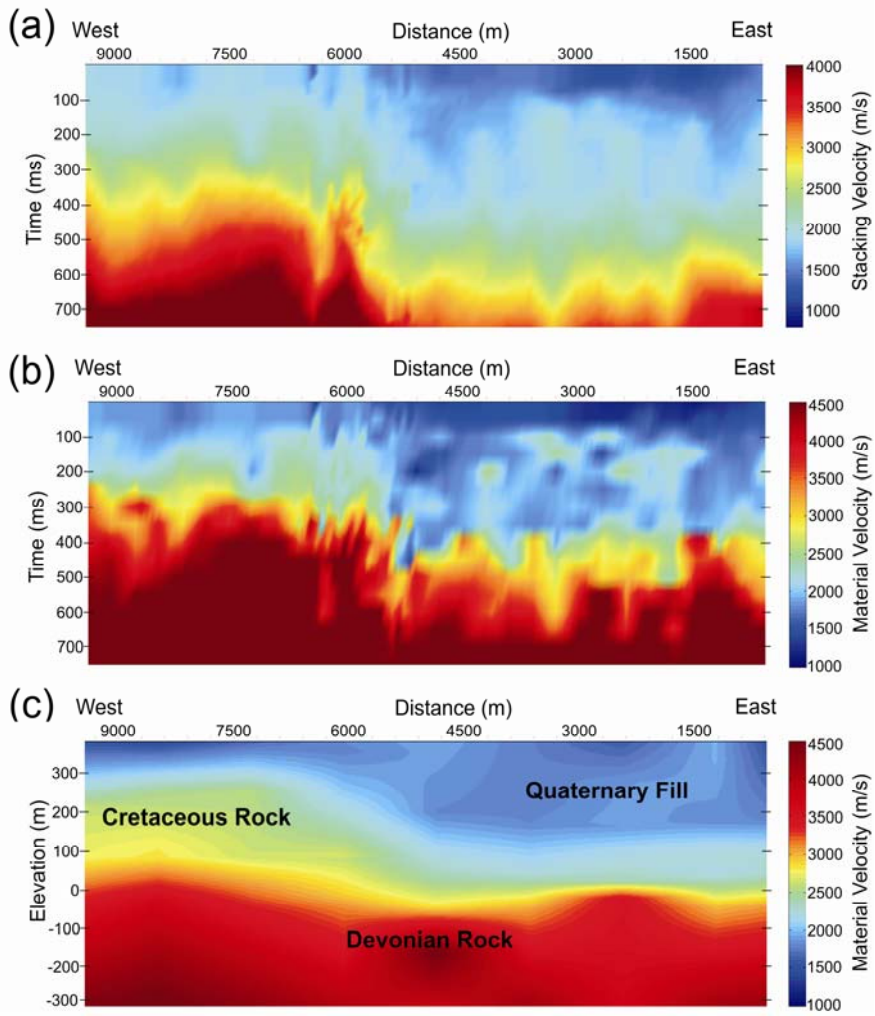

Figure A.4. (a) Final stacking velocities as picked during traditional velocity analyses on CMP supergathers. The vertical axis is two way time in ms. (b) As for (a) after conversion to interval velocities. (c) The interval velocities of the subsurface as acquired from the traveltime inversion with a vertical exaggeration of about 5. The vertical-axis is elevation in m a.s.l.; mean sea level is at 0 m; elevation above sea level is positive, while depth below sea level is negative. The different rock bodies, as labeled, can be distinguished based on their respective material velocities. The horizontal axis in all images is distance from the east to the west in m. The values of the velocities for each point in the subsurface are represented by colors according to the scale displayed beside each image.

Table A.4. PSDM processing sequence for the 2D seismic survey.

Processing Step
Trace editing
First-break picking
Elevation/refraction statics corrections
Spiking deconvolution
Time-variant bandpass filtering
Trace equalization
CMP binning
Initial velocity analyses
NMO corrections
Residual statics corrections
Inverse NMO corrections
Radial domain processing
Linear τ–p processing
Predictive deconvolution
Final velocity analyses
Final residual statics corrections
Prestack depth migration using tomographic velocity model
Stack
F-X prediction

Results and Discussion

The tomographic velocity distribution of the subsurface (Figure A.4c) created from the inversion of refracted and reflected traveltimes is an improvement over the simple refraction analysis carried out in the previous study. Delineating the paleovalley on the basis of the differences in the material velocities of the rocks in the area is the foremost reason for generating the

tomography. The Quaternary sediments in the east is readily distinguished from the Cretaceous bedrock in the west with material velocities varying from about 1700 m/s in the buried valley to about 2800 m/s in the bedrock (Figure A.4c). This is not surprising because the Quaternary fill deposits are expected to be loosely consolidated (giving rise to lower compressional wave velocities) in comparison to the stiffer Cretaceous bedrock. Accordingly, the edge of the valley is defined by rapid changes in the material velocities as observed in the inversion result at distances ~ between 4800 and 6000 m. Vertically, the transition in the velocities from the inversion (Figure A.4c) is not abrupt; however the geologically sharp unconformity (see Ahmad et al., 2009) at the base of both the Cretaceous and Quaternary sediments is still noticeable. The velocities rise rapidly in the tomographic result to values > 3500 m/s, typical of the deeper Devonian carbonates. The stacking velocities converted to interval velocities (Figure A.4b) are comparable to the final material velocities from the results of the traveltime inversion (Figure A.4c). The similarities, both in magnitude and features, between the two velocity images (Figures A.4b and A.4c) are apparent. It is noted, however, that the edge of the valley (~ distance 5700 m) as deduced from the interval velocities (Figure A.4b) derived from the picked stacking velocities, appears more abrupt than is observed in the tomographic velocity model (Figure A.4c). This difference in velocity transition from the valley to the Cretaceous rock could be related to challenges encountered in the course of picking the stacking velocities on washed-out CMP supergathers; since reflections were difficult to detect plainly in the washout zones. It is also observed that the top of the sub-Cretaceous unconformity (Ahmad et al., 2009), characterized by a noticeable jump in velocities, appears to be more uneven in the converted velocities (Figure A.4b) than in the results of the traveltime inversion (Figure A.4c); minor errors in the stacking velocity picking could possibly account for this contrast. It is observed that the success of the tomographic data in delineating the paleovalley is considerable.

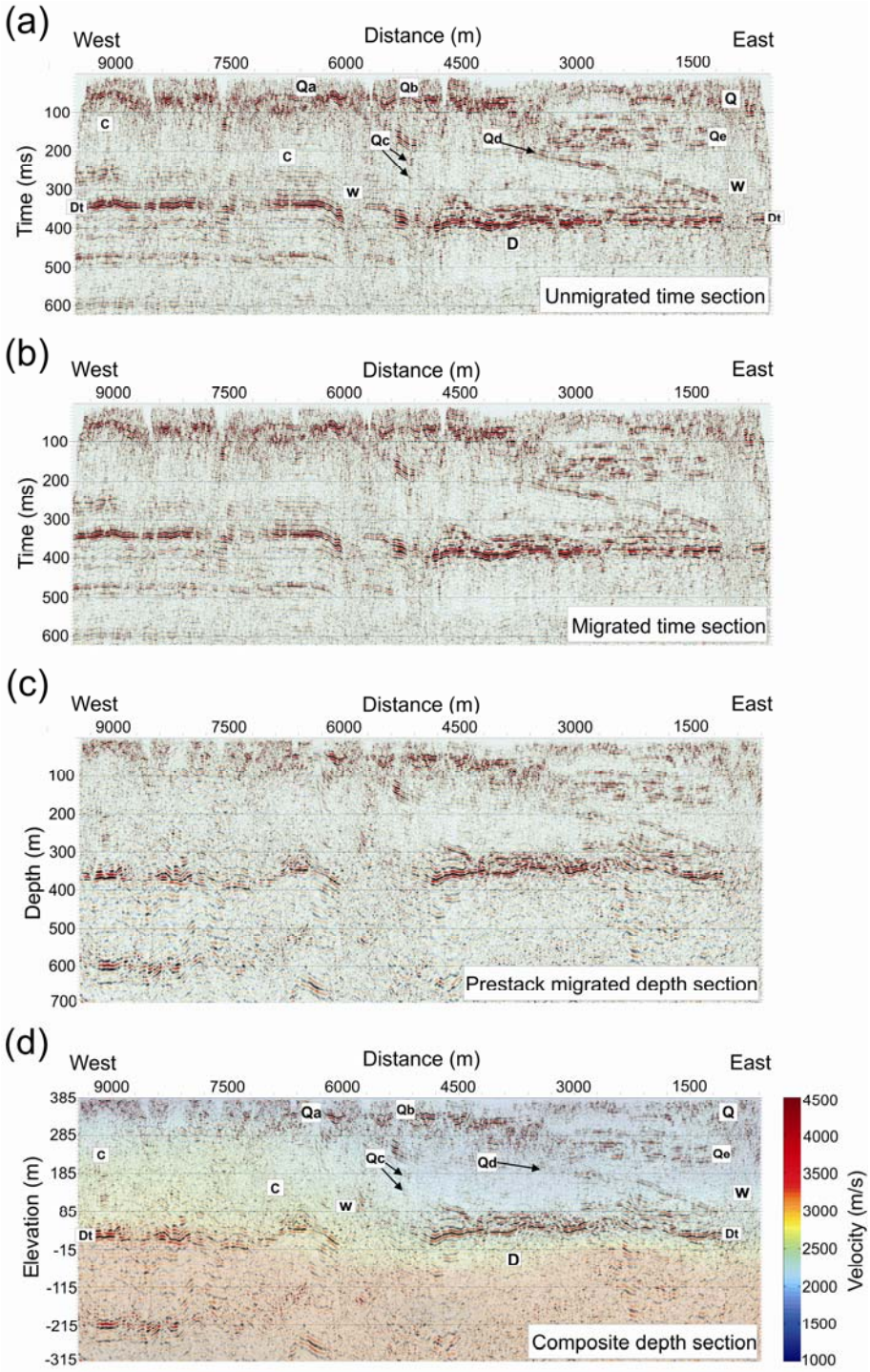

Figure A.5. (a) Unmigrated time seismic profile with interpretative tags. (b) Post-stack time migrated seismic section. (c) Final Prestack depth migrated seismic. (d) As for (c) overlaid with the traveltime inversion velocities. The interpretation tags in (a) and (d) are **D**: Devonian rock, **C**: Cretaceous Rock, **Q**: Quaternary fill, **w**: washed out regions, **Dt**: top of Devonian unconformity horizon, **Qa**: possible top

of Cretaceous bedrock, **Qb**: strong Quaternary event with possible gas presence, **Qc**: Quaternary dipping reflectors, **Qd**: strong dipping event within the Quaternary, and **Qe**: flat lying reflectors in the Quaternary fill. An automatic gain control of 300 ms was applied to each of the stacked seismic image and they were scaled in relation to the mean amplitude of their respective section.

However, the low-resolution inversion results (Figure A.4c) could not image details of the structure within the valley as are evident in the reflection profiles (Figures A.5a and A.5b). Some of the features include a variety of dipping reflectors **Qc** at the edge of the valley, strong dipping reflector **Qd** that is unconformable with the other reflectors, and the numerous flat lying reflectors **Qe**. Nonetheless, due to inadequate well information within the valley area, we cannot ascertain if there are substantial material velocity differences in the various sediments constituting the buried valley, which can be observed clearly on sonic logs.

In an attempt to convert the time section to depth, we used the tomographic velocity model to perform a prestack depth migration (PSDM) on the data (Figures A.5c and A.5d). The quality of the results, however, was not as good as anticipated as observed from the degraded reflection continuities, mostly in the western part of the line i.e., distances > 5000 m. This could be related to minor problems in the velocity model, which may require iterative refinement with aim of serving as input to the PSDM algorithm (see Bradford and Sawyer, 2002; Morozov and Levander, 2002; Bradford et al., 2006) for improved results. Seismic anisotropy may also play a role here as the tomographic image, which includes refracted head and turning waves could be biased by these more horizontal propagation paths. In addition, since a 2D migration can only collapse the Fresnel zone in the migration direction (Liner, 2004) the discontinuous nature of the reflections in the PSDM data could be that we are imaging an irregular 3D structure into the 2D profile.

Most of the wellbores in the immediate vicinity of the 2D line are for shallow gas production; hence they are not deep enough to reach the top of the unconformity. Nonetheless, two wells to the south at a distance < 3 km to the survey line penetrated the unconformity at an elevation of about 28 m a.s.l which is approximately 7 m deeper than the depth to the unconformity as can be observed clearly on the PSDM image (Figure A.5d). Considering the uneven topography of the top of the unconformity (Figure A.5a), this minor discrepancy in depth is not unreasonable. However, there is some level of uncertainty involved in estimating the top of the unconformity, known to be abrupt from core and well logs, from the 'smeared' results of the traveltime inversion. As mentioned earlier, the initially separated third and fourth layers of the tomographic velocity model are supposed to be one and the same; however, subsequent to the inversion implementation they were only adequately merged for the western part of the profile line and not the eastern side i.e., distance 1200 to 5100 m (see the section on Seismic Traveltime Inversion). Hence, either the top or base of the fourth layer can be picked as the top of the unconformity. If the top of layer four is selected as the top of the unconformity, there is agreement between the results of the traveltime inversion and the PSDM stacked section; however if the base of layer four is picked, there is some depth discrepancy of about 43 m. Additionally, estimating the depth of the unconformity from the tomography on the basis of an interpretation of the colors is quite subjective and easily biased.

The result of the previously processed reflection data using conventional (without radial and linear τ–p processing) steps (Ahmad et al., 2009) is displayed in Figure A.6a while that from the processing steps presented in this contribution is shown in Figure A.6b for comparison. From the magnified images besides each profile, better temporal and lateral resolution in the newly processed seismic is observed. Using the quarter-wavelength limit of vertical resolution (Widess, 1973) and a velocity of 2000 m/s, a vertical resolution of 16.6 to 6.25 m was obtained for the previously processed seismic data from dominant frequencies typically ranging from 30–80 Hz; and a vertical resolution of 10 to 3.3 m for the newly processed seismic profile mostly containing dominant frequencies in the

range 50–150 Hz. Evaluating the equation for threshold of lateral resolution i.e. radius of first Fresnel zone (Sheriff, 1980) with 1000 m/s as velocity at 150 ms two-way-time, the lateral resolution of the seismic section from the previous study ranged from 35.4 to 21.6 m (30–80 Hz dominant frequencies) and that of the new seismic profile varied from 27.4 to 15.8 m (50–150 Hz dominant frequencies) at about the same two-way traveltime. It is therefore evident from these values that the resolution of the data has been enhanced in the new seismic profile.

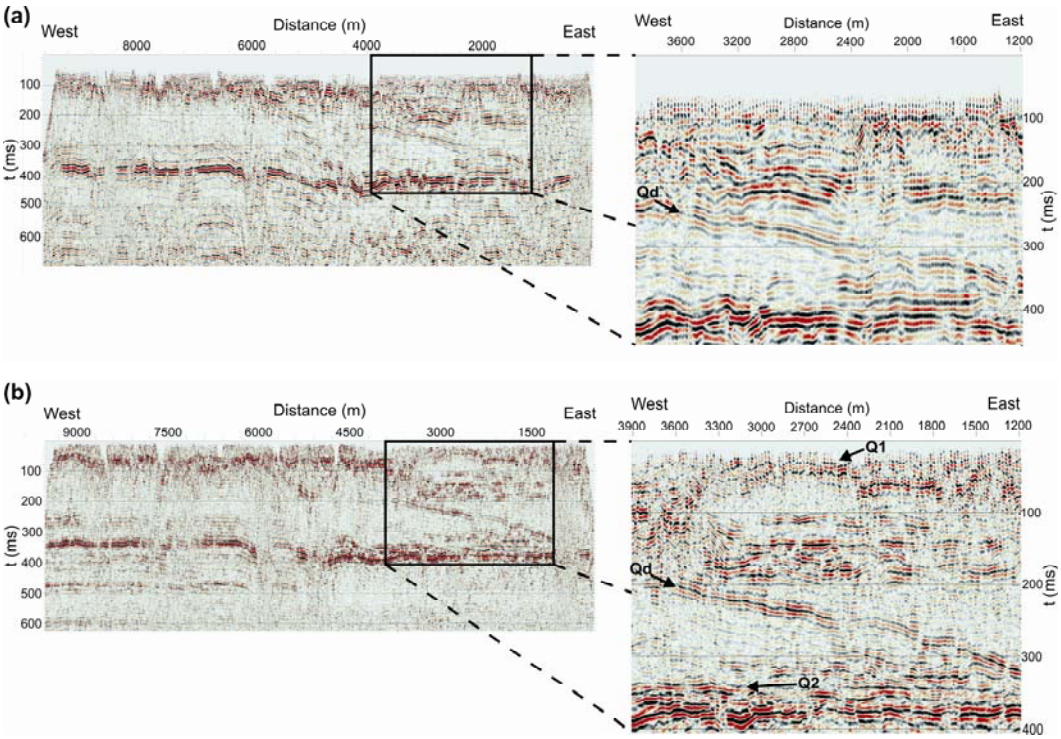

Figure A.6. (a) Previously processed seismic section using typical processing steps (Ahmad et al., 2009) not optimized to reduce source-generated noise. (b) Newly processed seismic optimized to reduce noise. An automatic gain control of 300 ms was applied to both stacked seismic sections and they were scaled with respect to the mean amplitude of the respective section. The images on the right hand sides are regions that have been magnified to highlight better resolution of the newly processed reflection seismic profile. The interpretation tags are: **Qd**: strong dipping event within the Quaternary, **Q1**: shallow event within the Quaternary, and **Q2**: resolved Quaternary horizons lying above the Devonian.

It is not clear from the previous seismic profile (Figure A.6a) if the low amplitude horizons immediately below the strong dipping event **Qd** are flat-lying or at an incline. On the other hand, the new profile (Figure A.6b) shows clearly that the abovementioned horizons are dipping from the west to the east. The clarification of the dipping-nature of these events was perhaps from the improved resolution of the new data, however one cannot rule out the possibility that the new processing scheme recovered some eliminated parts of the reflections, which could have been removed by the mute functions utilized in the previous processing, thus making them less coherent. At distance of about 2400 to 3000 m and time 30 ms, it is also possible to make out a nearly horizontal feature **Q1** on the new seismic data (Figure A.6b). In order to avoid misinterpreting coherent events and artifacts from various enhancement processing steps as reflections (e.g., Steeples and Miller, 1990; Steeples et al., 1997; Sloan et al., 2008), we attempted to validate the true nature of the **Q1** feature directly from the filtered shot records (Figure A.7a). However, this shallow feature, exhibiting lower frequency than deeper reflections on shot gathers could not be correlated with certainty to any true reflection and so without additional supporting evidence, this cannot be considered to be any more than a stacked coherent event.

Clearly noticeable on the new seismic profile (Figure A.6b) between distances 3000 and 4200 m are horizons **Q2** lying directly on top of the unconformity. These horizons appear to be merged with the sub-Cretaceous unconformity on the old seismic section (Figure A.6a) and so could not be easily distinguished. From the new profile, these high amplitudes reflections seem to cover almost the whole extent of the bottom of the valley from distance 4200 m on the west to distance 1200 m on the east at which point they become incoherent due to the smeared zone. Considering the fact that this flat-lying reflectors were not observed outside the paleovalley (distances > 6000 m), they are likely to be of Quaternary age sediments, deposited immediately after the erosion caused by the glacial meltwaters, or alternatively may be remnants of the erosion of the valley itself.

Washout/smeared zones **w** were problematic to the imaging (Figure A.5). In particular, the western edge of the valley (~ distance 5700 m) was not well imaged due to a large washout zone at that location. The washout zones are attenuated regions where continuous reflections are not observed. As observed from the unprocessed shot gathers, it is not possible to make out any strong reflection in these zones. Though the exact cause of this attenuation is not known, it is likely associated with thicker zones of muskeg (sphagnum moss filled bogs). The most conspicuous event in the reflection sections is the strong reflector **Dt** located at about halfway down the vertical axis of the profiles. Aside from the washout zones **w**, this reflector, which is the unconformity above the Devonian rock, spans the entire survey line. Above the unconformity lies Cretaceous bedrock **C** to the west of distance 6000 m and Quaternary sediments **Q** to the east of distance 4800 m. The edge of the paleovalley, dipping from west to east, lies between distances 4800 and 6000 m.

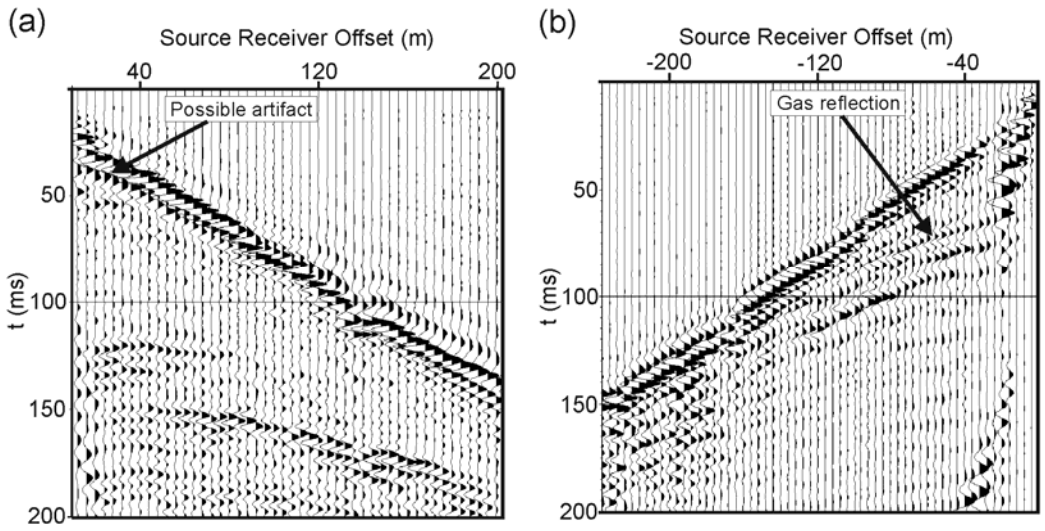

Figure A.7. Raw shot gathers after elevation/refraction static corrections, spiking deconvolution, time-variant bandpass filtering, and trace equalization located near (a) the poorly-constrained shallow 30 ms **Q1** feature from Figure 6b, and (b) strong reflection that is interpreted to be the top of a near surface methane saturated sand of Figure 8b.

There is a shallow high amplitude reflection **Qa** from about distance 6000 to 9300 m at a two-way-time of approximately 50 ms (Figure A.5a). This event could be the top of the Cretaceous bedrock. It is interesting to note that the reflection is not continuous across the entire survey line to the valley area on the eastern side. A possible explanation for this could be the minimal impedance contrast between the glacial sediments that blankets the whole area and the deposits that constitute the buried valley. This event could not be made out clearly on the previously processed seismic profile; this points to the fact that the new data is improved in comparison to the old.

New shallow features, not apparent in the previous processing of Ahmad et al. (2009) as illustrated in Figure A.8, are particularly worthy of note. As also seen on the PSDM seismic profile (Figure A.5d), there is a strong reflector **Qb** at elevation of about 345 m a.s.l (~ 40 m depth), inside but at the edge of the valley (between distances 3900 and 5100 m). This strong reflector, also clearly seen in the raw shot gathers (e.g., Figure A.7b), likely indicates presence of free gas, which continues to be produced in commercial quantities from this site (Rainbow and the Sousa fields in northern Alberta) over the last decade at depths of less than 100 m (see Pawlowicz et al., 2004; Kellett, 2007). Considering that the shallow gas in the Rainbow field has a chemical signature implicating a deeper, thermogenic origin, and also the high electrical resistivities recorded in our survey area, it has been suggested that gases migrated from the Cretaceous bedrock formations and were trapped within the porous Quaternary sediments (Ahmad et al., 2009).

These shallow gas deposits had previously been found 'serendipitously' during the drilling of shallow water or deeper petroleum boreholes; and on numerous occasions have led to dangerous releases of flammable methane gas leading to destruction of rigs in some cases. Ground based electrical resistivity tomography (ERT) studies have been used in the past to indicate free, dry gas on the basis of high electrical resistivities. However, it can be difficult to separate the gas-saturated from fresh water-saturated zones. The reprocessing of this current data set suggests that with sufficient care such shallow gas filled zones may be

distinguished; carrying out high resolution seismic surveys over areas already targeted for drilling on the basis of ERT could add confidence and warn drillers about the potential shallow blow-out hazards.

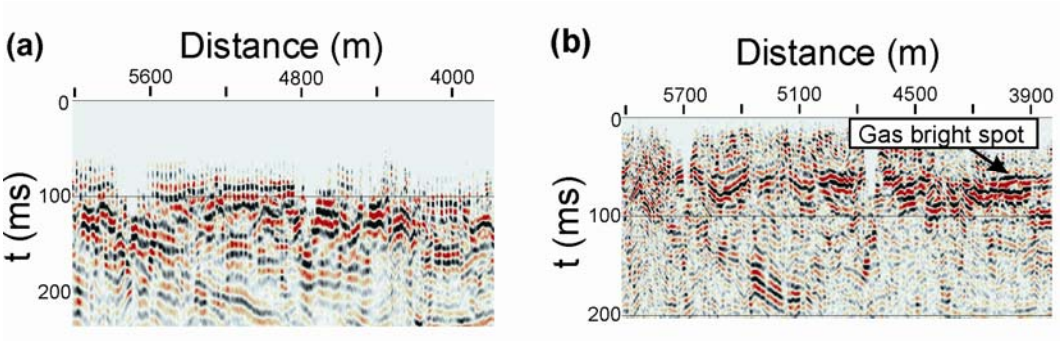

Figure A.8. Detailed comparison of topmost section of profile over known near surface gas reservoir (a) the previously processed seismic section of Ahmad et al. (2009), and (b) re-processed seismic reflection profile showing strong reflector that indicates the presence of free gas.

Conclusions

We have presented here the results of re-analyses of a near-surface seismic dataset acquired over a paleovalley in northern Alberta, Canada. Our study includes the generation of a traveltime inversion to better delineate the buried valley; the re-processing of the reflection data to enhance its resolution and recover any muted or degraded horizon from the previous processing; and an attempt to employ pre-stack depth migration using velocities obtained from the traveltime inversion for proper depth scale presentation.

Construction of the tomographic velocity from the inversion of direct, refracted and reflected waves was aimed at determining the accurate representation of the velocity distribution of the area over the buried valley as an improvement to the simple refraction analysis performed in the previous study. The results from the traveltime inversion showed clearly that a buried valley can be delineated from the surrounding rock bodies on the basis of the material velocities. The interval velocity of the loosely consolidated Quaternary fill valley

was observed to be around 1700 m/s while that of the more competent Cretaceous bedrock was in the region of 2800 m/s with the edge of the valley defined by rapid changes in the material velocities. The interpretation made from the tomographic model is important because of the significant knowledge it provides about velocity contrasts of different materials; on the other hand, this detailed information about the exact contrasts in the physical properties producing reflections may not be readily deduced from seismic reflection profiles alone, particularly given the absence of appropriate sonic and density well logs in the area. It is noted, however, that the resolution of the traveltime inversion was insufficient to image clearly the different rock features within the valley possibly due to the complexities in the structure of the valley. It is suggested that waveform inversion with the tomographic results as input model may be a viable option in imaging the complex architecture of the paleovalley.

The seismic reflection data was processed with a strategy optimized to enhance the lateral and vertical resolution of the profile; and also to recover any muted or degraded reflection from the old study by employing noise suppression techniques in other domains as opposed to the total muting of the noise cone in *t-x* coordinates. The processing steps included radial and linear τ–p processing utilized to reduce the noise and time-variant bandpass filtering to improve the resolution. Better resolution and more continuous events characterize the final stack of the newly time processed reflection profile in comparison to the previously processed seismic with lateral resolution enhanced by ~ 30% in the near surface and vertical resolution enhanced by ~ 75%. In addition, the dipping nature of some events, which could not be established on the initial processing, was ascertained on the new seismic images; likewise some indistinguishable horizons lying immediately over the sub-Cretaceous unconformity were identified on the newly processed profile. This underscores the significance of ensuring that high frequency signals are predominantly kept during the processing of near-surface reflection data. New bright near surface features, indicating presence of gas were better imaged in the new section. These features, not apparent in the old image, were probably muted during the previous processing sequence; hence we

emphasize the importance of experimenting with different noise suppression procedures before resorting to total muting of the noise cone. Aside from some washout zones in the data, the rock fabric and complex architecture of the channel and of the surrounding rock were imaged with better resolution in the newly processed stacked time section, and it is thus deemed to produce a better result in comparison to the previous study.

Subsequently, we attempted a prestack depth migration on the noise-suppressed reflection seismic dataset with the velocity field derived from the tomography. We observed the quality of the result to be less than expected with obvious reflection continuity losses in some areas. We judged that minor problems in the tomographic model may be the reason for this. Refining the tomographic image iteratively as input into the PSDM algorithm may likely produce an image with unbroken reflections. The results, however, validate the importance of using a good velocity model for migration and the challenge in obtaining the essential velocity accuracy from the shallow part of seismic data. In spite of the loss in reflection continuity, the depth to the sub-Cretaceous unconformity as observed on the PSDM data is consistent with the depth information obtained from two wellbores at a distance of less than 3 km to the 2D seismic profile.

Acknowledgements

We will like to thank Sam Kaplan and Todd Bown of the University of Alberta for assisting with the prestack depth migration processing and wellbore data gathering, respectively. We acknowledge also, Colin Zelt and Uri ten Brink for providing a copy of rayinvr and RayGUI software respectively for the implementation of the seismic tomography inversion, and GEDCO Ltd. for access to their VISTA® seismic data processing software via their university support program. The seismic acquisition field crew includes Jawwad Ahmad, Marek Welz, Len Tober, Gabrial Solano, Tiewei He, and Dean Rokosh (University of Alberta); John Pawlowciz, (Alberta Geological Survey, Edmonton); and Alain Plouffe (Geological Survey of Canada, Ottawa). Primary funding for the field

programs was initiated by the Geological Survey of Canada and the Alberta Geological Survey via the Targeted Geoscience Initiative – II programs. The work in this contribution was supported by the National Engineering and Research Council Discovery Grant and the Canada Research Chairs programs to D.R.S.

References

Ahmad, J., 2006, High-Resolution seismic and electrical resistivity tomography techniques applied to image and characterize a buried channel: M.S. thesis, University of Alberta.

Ahmad, J., D. R. Schmitt, C. D. Rokosh, and J. G. Pawlowicz, 2009, High resolution seismic and resistivity profiling of a buried Quaternary subglacial valley: Northern Alberta, Canada: Geological Society of America Bulletin, **121**, 1570–1583.

Auken, E., K. Sorensen, H. Lykke-Andersen, M. Bakker, A. Bosch, J. Gunnink, F. Binot, G. Gabriel, M. Grinat, H. M. Rumpel, A. Steuer, H. Wiederhold, T. Wonik, P. F. Christensen, R. Friborg, H. Guldager, S. Thomsen, B. Christensen, K. Hinsby, F. Jorgensen, I. M. Balling, P. Nyegaard, D. Seifert, T. Sormenborg, S. Christensen, R. Kirsch, W. Scheer, J. F. Christensen, R. Johnsen, R. J. Pedersen, J. Kroger, M. Zarth, H. J. Rehli, B. Rottger, B. Siemon, K. Petersen, M. Kjaerstrup, K. M. Mose, P. Erfurt, P. Sandersen, V. Jokumsen, and S. O. Nielsen, 2009, Buried quaternary valleys – a geophysical approach: Zeitschrift Der Deutschen Gesellschaft Fur Geowissenschaften, **160**, 237–247.

Baker, G. S., D. W. Steeples, and M. Drake, 1998, Muting the noise cone in near-surface reflection data: An example from southeastern Kansas: Geophysics, **63**, 1332–1338.

Belfer, I., I. Bruner, S. Keydar, A. Kravtsov, and E. Landa, 1998, Detection of shallow objects using refracted and diffracted seismic waves: Journal of Applied Geophysics, **38**, 155–168.

Benjumea B., J. A. Hunter, J. M. Aylsworth, and S. E. Pullan, 2003, Application of high-resolution seismic techniques in the evaluation of earthquake site response, Ottawa Valley, Canada: Tectonophysics, **368**, 193–209.

Best, M. E., V. M. Levson, T. Ferbey, and D. McConnell, 2006, Airborne electromagnetic mapping for buried quaternary sands and gravels in northeast British Columbia, Canada: Journal of Environmental and Engineering Geophysics, **11**, 17–26.

Biondi, B., 2003, Equivalence of source-receiver migration and shot-profile migration: Geophysics **68**, 1340–1347.

Bradford, J. H., and D. S. Sawyer, 2002, Depth characterization of shallow aquifers with seismic reflection – Part II: Prestack depth migration and field examples: Geophysics, **67**, 98–109.

Bradford, J. H., L. M. Liberty, M. W. Lyle, W. P. Clement, and S. Hess, 2006, Imaging complex structure in shallow seismic-reflection data using prestack depth migration: Geophysics, **71**, no. 6, B175–B181.

Büker, F., A. G. Green, and H. Horstmeyer, 1998, Shallow seismic reflection study of a glaciated valley: Geophysics, **63**, 1395–1407.

Büker, F., A. G. Green, and H. Horstmeyer, 2000, 3-D high-resolution reflection seismic imaging of unconsolidated glacial and glaciolacustrine sediments: processing and interpretation: Geophysics, **65**, 1395–1407.

Canales, L. L., 1984, Random noise reduction: 54th Annual International Meeting, SEG, Expanded Abstracts, 525–527.

Chambers, J. E., O. Kuras, P. I. Meldrum, R. D. Ogilvy, and J. Hollands, 2006, Electrical resistivity tomography applied to geologic, hydrogeologic, and engineering investigations at a former waste-disposal site: Geophysics, **71**, no. 6, B231–B239.

Clague, J. J., J. L. Luternauer, S. E. Pullan, and J. A. Hunter, 1991, Postglacial deltaic sediments, southern Fraser River delta, British Columbia: Canadian Journal of Earth Sciences, **28**, 1386–1393.

Deen, T., and K. Gohl, 2002, 3-D tomographic seismic inversion of a paleochannel system in central New South Wales, Australia: Geophysics, **67**, no. 5, 1364–1371.

De Iaco, R., A. G. Green, H. R. Maurer, and H. Horstmeyer, 2003, A combined seismic reflection and refraction study of a landfill and its host sediments: Journal of Applied Geophysics, **52**, 139–156.

Fenton, M. M., J. G. Pawlowicz, R. S. Paulen, G. J. Prior, and R. A. Olson, 2003, Quaternary geology of northern Alberta: Implications for kimberlite exploration: 8th International Kimberlite Conference, Program with Abstracts, 125–126.

Fenton, M. M., B. T. Schreiner, E. Nielsen, and J. G. Pawlowicz, 1994, Quaternary geology of the Western Plains, *in* G. D. Mossop, and I. Shetson, eds., Geological atlas of the western Canada sedimentary basin: Calgary, Alberta: Canadian Society of Petroleum Geologists and the Alberta Research Council, 413–420.

Fisher, T. G., H. M. Jol, and A. M. Boudreau, 2005, Saginaw Lobe tunnel channels (Laurentide Ice Sheet) and their significance in south-central Michigan, USA: Quaternary Science Reviews, **24**, 2375–2391.

Fradelizio, G. L., A. Levander, and C. A. Zelt, 2008, Three-dimensional seismic-reflection imaging of a shallow buried paleochannel: Geophysics, **73**, no. 5, B85–B98.

Francese, R. G., Z. Hajnal, and A. Prugger, 2002, High-resolution images of shallow aquifers—A challenge in near-surface seismology: Geophysics, **67**, 177–187.

Gabriel, G., R. Kirsch, B. Siemon, and H. Wiederhold, 2003, Geophysical investigation of buried Pleistocene subglacial valleys in northern Germany: Journal of Applied Geophysics, **53**, 159–180.

Greenhouse, J.P, and P. F. Karrow, 1994, Geological and geophysical studies of buried valleys and their fills near Elora and Rockwood, Ontario: Canadian Journal of Earth Sciences, **31**, 1838–1848.

Henley, D. C., 1999, The radial trace transform: an effective domain for coherent noise attenuation and wave field separation: 69th Annual International Meeting, SEG, Expanded Abstracts, 1204–1207.

Hickin, A. S., B. Kerr, D. G. Turner, and T. E. Barchyn, 2008, Mapping quaternary paleovalleys and drift thickness using petrophysical logs, northeast British Columbia, Fontas map sheet, NTS 94I: Canadian Journal of Earth Sciences, **45**, 577–591.

Hooke, R. L., and C. E. Jennings, 2006, On the formation of the tunnel valleys of the southern Laurentide ice sheet: Quaternary Science Reviews, **25**, 1364–1372.

Hunter, J. A., S. E. Pullan, R. A. Burns, R. M. Gagne, and R. L. Good, 1984, Shallow seismic reflection mapping of the overburden-bedrock interface with the engineering seismograph—some simple techniques: Geophysics, **49**, 1381–1385.

Jørgensen, F., H. Lykke-Andersen, P. B. E. Sandersen, E. Auken, and E. Nørmark, 2003a, Geophysical investigations of buried Quaternary valleys in Denmark: an integrated application of transient electromagnetic soundings, reflection seismic surveys and exploratory drillings: Journal of Applied Geophysics, **53**, 215–228.

Jørgensen, F., and P. B. E. Sandersen, 2008, Mapping of buried tunnel valleys in Denmark: new perspectives for the interpretation of the quaternary succession: Geological Survey of Denmark and Greenland Bulletin, **15**, 33–36.

Jørgensen, F., P. B. E. Sandersen, and E. Auken, 2003b, Imaging buried Quaternary valleys using the transient electromagnetic method: Journal of Applied Geophysics, **53**, 199–213.

Juhlin, C., H. Palm, C. Müllern, and B. Wållberg, 2002, Imaging of groundwater resources in glacial deposits using high-resolution reflection seismics, Sweden: Journal of Applied Geophysics, **51**, 107–120.

Kellett, R., 2007, A geophysical facies description of Quaternary channels in northern Alberta: CSEG Recorder, **32**, no. 10, 49–55.

Lennox, D. H., and V. Carlson, 1967, Geophysical exploration for buried valleys in an area north of Two Hills Alberta: Geophysics, **32**, 331–362.

Levson, V., 2008, Geology of northeast British Columbia and northwest Alberta: diamonds, shallow gas, gravel, and glaciers: Canadian Journal of Earth Sciences, **45**, 509–512.

Liner, C. L., 2004, Elements of 3D seismology: PennWell Corporation.

Miller, R. D., D. W. Steeples, and M. Brannan, 1989, Mapping a bedrock surface under dry alluvium with shallow seismic reflections: Geophysics, **54,** 1528–1534.

Montagne, R., and G. L. Vasconcelos, 2006, Extremum criteria for optimal suppression of coherent noise in seismic data using the Karhunen–Loève transform: Physica A, **371**, 122–125.

Morozov, I. B., and A. Levander, 2002, Depth image focusing in traveltime map-based wide-angle migration: Geophysics, **67**, 1903–1912.

Nitsche F.O., A. G. Green, H. Horstmeyer, and F. Büker, 2002, Late Quaternary depositional history of the Reuss delta, Switzerland: constraints from high-resolution seismic reflection and georadar surveys: Journal of Quaternary Science, **17**, 131–143.

ÓCofaigh, C., 1996, Tunnel valley genesis: Progress in Physical Geography, **20**, 1–19.

Ogunsuyi, O., D. Schmitt, and J. Ahmad, 2009, Seismic traveltime inversion to complement reflection profile in imaging a glacially buried valley: 79th Annual International Meeting, SEG, Expanded Abstracts, 3675–3678.

Paulen, R. C., M. M. Fenton, J. A. Weiss, J. G. Pawlowicz, A. Plouffe, and I. R. Smith, 2005, Surficial Geology of the Hay Lake Area, Alberta (NTS 84L/NE): Alberta Energy and Utilities Board, EUB/AGS Map 316, scale 1:100000.

Pawlowicz, J. G., A. S. Hicken, T. J. Nicoll, M. M. Fenton, R. C. Paulen, A. Plouffe, and I. R. Smith, 2004, Shallow gas in drift: northwestern Alberta: Alberta Energy and Utilities Board, EUB/AGS Information Series **130**.

Pawlowicz, J. G., A. S. Hickin, T. J. Nicoll, M. M. Fenton, R.C. Paulen, A. Plouffe, and I. R. Smith, 2005a, Bedrock topography of the Zama Lake area, Alberta (NTS 84L): Alberta Energy and Utilities Board, EUB/AGS Map 328, scale 1:250000.

Pawlowicz, J. G., A. S. Hickin, T. J. Nicoll, M. M. Fenton, R. C. Paulen, A. Plouffe, and I. R. Smith, 2005b, Drift thickness of the Zama Lake area, Alberta (NTS 84L): Alberta Energy and Utilities Board, EUB/AGS Map 329, scale 1:250000.

Plouffe, A., I. R. Smith, R. C. Paulen, M. M. Fenton, and J. G. Pawlowicz, 2004, Surficial geology, Bassett Lake, Alberta (NTS 84L SE): Geological Survey of Canada, Open File 4637, scale 1:100000.

Pugin, A. J., T. H. Larson, S. L. Sargent, J. H. McBride, and C. E. Bexfield, 2004, Near-surface mapping using SH-wave and P-wave seismic land-streamer data acquisition in Illinois, U.S.: The Leading Edge, **23**, 677–682.

Pugin, A. J. –M., S. E. Pullan, J. A. Hunter, and G. A. Oldenborger, 2009, Hydrogeological prospecting using p- and s-wave landstreamer seismic reflection methods: Near Surface Geophysics, **7**, 315–327.

Pullan, S.E., J. A. Hunter, H. A. J. Russell, and D. R. Sharpe, 2004, Delineating buried-valley aquifers using shallow seismic reflection profiling and grid downhole geophysical logs – an example from southern Ontario, Canada, *in* C. Chen, and J. H. Xia, eds., Progress in environmental and engineering geophysics:

proceedings of the International Conference on Environmental and Engineering Geophysics, Wuhan, China, 39–43.

Roberts, M. C., S. E. Pullan, and J. A. Hunter, 1992, Applications of land-based high resolution seismic reflection analysis to Quaternary and geomorphic research: Quaternary Science Reviews, **11**, 557–568.

Robertsson, J. O. A., K. Holliger, A. G. Green, A. Pugin, and R. De Iaco, 1996, Effects of near-surface waveguides on shallow high-resolution seismic refraction and reflection data: Geophysical Research Letters, **23**, 495–498.

Ronen, J., and J. F. Claerbout, 1985, Surface-consistent residual statics estimation by stack-power maximization: Geophysics, **50,** 2759–2767.

Sanderson, P. B. E., and F. Jørgensen, 2003, Buried Quaternary valleys in western Denmark — occurrence and inferred implications of groundwater resources and vulnerability: Journal of Applied Geophysics, **53**, 229–248.

Schijns, H., S. Heinonen, D. R. Schmitt, P. Heikkinen, and I. T. Kukkonen, 2009, Seismic refraction traveltime inversion for static corrections in a glaciated shield rock environment: a case study: Geophysical Prospecting, **57**, 997–1008.

Sharpe, D. R., A. Pugin, S. E. Pullan, and G. Gorrell, 2003, Application of seismic stratigraphy and sedimentology to regional hydrogeological investigations: an example from Oak Ridges Moraine, southern Ontario, Canada: Canadian Geotechnical Journal, **40**, 711–730.

Sharpe, D., A. Pugin, S. Pullan, and J. Shaw, 2004, Regional unconformities and the sedimentary architecture of the Oak Ridges Moraine area, southern Ontario: Canadian Journal of Earth Sciences, **41**, 183–198.

Sheriff, R. E., 1980, Nomogram for fresnel-zone calculation: Geophysics, **45**, 968–972.

Sloan, S. D., D. W. Steeples, and P. E. Malin, 2008, Acquisition and processing pitfall associated with clipping near-surface seismic reflection traces: Geophysics, **73**, no. 1, W1–W5.

Song, J. L., and U. ten Brink, 2004, RayGUI 2.0 - a graphical user interface for interactive forward and inversion ray-tracing: U.S. Geological Survey Open-File Report 2004–1426.

Spitzer, R., F. O. Nitsche, A. G. Green, and H. Horstmeyer, 2003, Efficient acquisition, processing and interpretation strategy for shallow 3D seismic surveying: a case study: Geophysics, **68**, 1792–1806.

Spitzer, R., F. O. Nitsche, and A. G. Green, 2001, Reducing source-generated noise in shallow seismic data using linear and hyperbolic τ–p transformations: Geophysics, **66**, 1612–1621.

Steeples, D. W., A. G. Green, T. V. McEvilly, R. D. Miller, W. E. Doll, and J. W. Rector, 1997, A workshop examination of shallow seismic reflection surveying: The Leading Edge, **16**, 1641–1647.

Steeples, D. W., and R. D. Miller, 1990, Seismic reflection methods applied to engineering, environmental, and groundwater problems, *in* S. H. Ward, ed., Geotechnical and environmental geophysics 1: Society of Exploration Geophysicists, 1–30.

Steeples, D. W., and R. D. Miller, 1998, Avoiding pitfalls in shallow seismic reflection surveys: Geophysics, **63**, 1213–1224.

Steuer, A., B. Siemon, and E. Auken, 2009, A comparison of helicopter-borne electromagnetics in frequency- and time-domain at the Cuxhaven valley in northern Germany: Journal of Applied Geophysics, **67**, 194–205.

Stoffa, P. L., J. T. Fokkema, R. M. de Luna Freire, and W. P. Kessinger, 1990, Split-step fourier migration: Geophysics, **55**, 410–421.

Widess M. B., 1973, How thin is a thin bed?: Geophysics, **38**, 1176–1180.

Wiederhold, H., H. A. Buness, and K. Bram, 1998, Glacial structures in northern Germany revealed by a high-resolution reflection seismic survey: Geophysics, **63**, 1265–1272.

Wiederhold, H., H. M. Rumpel, E. Auken, B. Siemon, W. Scheer, and R. Kirsch, 2008, Geophysical methods for investigation and characterization of groundwater resources in buried valleys: Grundwasser, **13**, 68–77.

Yilmaz, Ö., 2001, Seismic data analysis: processing, inversion, and interpretation of seismic data (Investigations in Geophysics, no. 10): Society of Exploration Geophysicists.

Zelt C. A., A. Azaria, and A. Levander, 2006, 3D seismic refraction traveltime tomography at a groundwater contamination site: Geophysics, **71**, no. 5, H67–H78.

Zelt, C. A., and R. B. Smith, 1992, Seismic traveltime inversion for 2-D crustal velocity structure: Geophysical Journal International, **108**, 16–34.